UNIVERSITAT POLITÈCNICA DE CATALUNYA
BARCELONATECH
Institut de Tècniques Energètiques

# Improvement of Early Warning Monitoring using Gamma Spectrometry

Anna Camp Brunés

Doctoral Dissertation

Supervisor:
Dr. Arturo Vargas Drechsler
Institut de Tècniques Energètiques (INTE)
Universitat Politècnica de Catalunya (UPC)

*A tu, científic.*

# Agraïments

Durant aquests anys d'investigació, són diverses les persones i institucions les que han fet possible que es pogués dur a terme el treball realitzat. Malgrat les paraules sempre poden quedar-se curtes, les següents línies volen ser una mostra d'agraïment a moltes d'elles.

Primer de tot, mostrar el meu agraïment cap a l'Institut de Tècniques Energètiques (INTE) de la Universitat Politècnica de Catalunya. Gràcies per permetre'm dur a terme aquesta investigació i proporcionar-me suport tant econòmic com personal. L'ajuda dels seus programes de formació, l'accés als laboratoris i instal·lacions i el suport dels diferents grups de recerca són els que han permès realitzar el treball que es presenta en aquest document.

A tot el personal de l'INTE, per fer de l'Institut el què és i per la vostra col·laboració. Gràcies a tot l'equip d'investigadors per la vostra col·laboració, en especial aquelles llargues tardes al Laboratori de Calibratge i Dosimetria, i a tot el personal tècnic pel vostre suport sempre que va caldre desenvolupar nous instruments, prototips i dedicar totes les hores necessàries perquè els meus coneixement informàtics estiguessin a un nivell més o menys adient.

A tots els estudiants de doctorat que hem coincidit durant aquests anys. De tots hem aprés i entre tots hem fet que el nostre pas per l'Institut tingués l'ambient distés que tant important resulta perquè tota gran feina pugui arribar a bon port.

Especial menció es mereix, tant per la part que li correspon com a personal de l'Institut com per haver fet possible aquesta tesi, el Dr. Arturo Vargas. Gracias Arturo por haber confiado en mí cuando nos conocimos en una asignatura de Master, me ofreciste la posibilidad de realizar el proyecto final en una de tus líneas de investigación y luego, de seguir mi investigación con la tesis. Con todo ello me permitiste conocer en primera persona lo que significa ser un investigador y tener una visión crítica como científica. Gracias también por el soporte

personal, por la paciencia y a la vez la insistencia, sin las cuales no habría sido posible terminar este trabajo.

Gràcies al suport de la beca ARGOS que, en el passat en els estudis de Màster i després durant la tesi, va proporcionar-me el suport econòmic necessari per impulsar aquesta investigació.

Thanks to EURADOS project and all its research teams. Nowadays, connection among research groups is essential. Your, our, project has allowed me the opportunity of knowing people from different institutions, to share information with them and to participate in several projects at European level. Also thanks to the MetroERM project which supported the last year of my PhD and allow me to participate in the project with this research.

Specially thanks to my new Greek family. Beyond the knowledge acquired during this research, my other little treasure is fantastic people I have had the pleasure to meet.

Especial atención merecen también aquellos grupos de otras universidades y departamentos que, bien por haber compartido proyectos o bien por tener como objetivo común el avance científico, han contribuido de forma inestimable a este proyecto. El grupo ICARUS de la UPC, que puso a nuestro alcance sus prototipos de UAV's y todos sus conocimientos técnicos. Al grupo de la estación ESMERALDA del CIEMAT, que nos ha permitido instalar allí equipos de medida, proporcionándonos un nuevo punto de medida adicional al de Barcelona. Y por supuesto al Dr. J. M. Fernández-Varea, con quien tuve el placer de trabajar durante el desarrollo de uno de los capítulos de esta tesis y que aportó tanto conocimiento como rigor y metodología al trabajo realizado.

Fora de l'àmbit universitari, també vull mostrar el meu agraïment als amics i la família, per la feina inestimable que heu fet escoltant llargues dissertacions tant professionals com personals, aportant aquella visió externa que tant imprescindible resulta en tota investigació. I en especial al Rafa, per ser sempre allà, per confiar en mi i els meus projectes probablement més del que sóc capaç de confiar-hi jo mateixa. Simplement perquè espero que segueixis formant part de tots els que encara estan per venir.

# Scientific Production

The scientific production carried out during this PhD are listed in the following, including published and submitted papers and scientific contributions to workshops.

Scientific Publications

- Camp, A., Vargas, A., 2014. Ambient dose estimation H*(10) from $LaBr_3$(Ce) spectra. Radiat. Prot. Dosimetry 160, 264–8. doi:10.1093/rpd/nct342
- Vargas, A., Camp, A., Serrano, I., Duch, M.A., 2014. Coincidence summing corrections for volume samples using the PENELOPE/penEasy Monte Carlo code. Appl. Radiat. Isot. 87, 376–9. doi:10.1016/j.apradiso.2013.11.057
- Camp, A., Vargas, A., Fernández-Varea, J.M., 2015. Determination of LaBr3(Ce) internal background using a HPGe detector and Monte Carlo simulations. Appl. Radiat. Isot. doi:10.1016/j.apradiso.2015.11.093
- Vidmar, T., Camp, A., Hurtado, S., Jäderström, H., Kastlander, J., Lépy, M.-C., Lutter, G., Ramebäck, H., Sima, O., Vargas, A., 2015. Equivalence of computer codes for calculation of coincidence summing correction factors – Part II. Appl. Radiat. Isot. doi:10.1016/j.apradiso.2015.11.071
- Kessler, P., Camp, A., Dombrowski, H., Neumaier, S., Röttger, A., Vargas, A., 2017. Influence of Radon Progeny on Dose Rate Measurements Studied at PTB's Radon Reference Chamber. Radiat. Prot. Dosimetry 1–8. doi:10.1093/rpd/ncx059
- Vargas, A., Cornejo, N., Camp, A., 2017. Comparison of methods for H*(10) calculation from LaBr3(Ce) measured spectra. Appl. Radiat. Isot. Submitted.

Scientific Presentations

- EURADOS Annual Meeting. Barcelona, 4 – 8 February 2013.
  - Arturo Vargas and Anna Camp. Detector Response from MC Calculations and Experiments. Oral presentation.
  - Arturo Vargas and Anna Camp. Stripping Method used in the INTE-UPC. MC Results. Oral presentation.

- Joint International Workshop on Off-Site Gamma Dose Rate and Ground Contamination Measurements. Freiburg, 13 – 15 May 2013.
  - Anna Camp and Arturo Vargas. Ambient Dose Estimation H*(10) from $LaBr_3$(Ce) Spectra. Oral presentation.
  - Anna Camp, Arturo Vargas, Natalia Alegria, Fernando Legarda, Alexander Clouvas, Sthelios Xanthos, Costas Potiriadis and Georgios Takoudis. An Intercomparison of Monte Carlo Simulation Codes Applied to a $LaBr_3$(Ce) Detector. Oral presentation.

- International Committee for Radionuclide Metrology 2013. Antwerpen, 16 – 21 June 2013.
  - Arturo Vargas, Anna Camp, Isabel Serrano and Maria Amor Duch. Gamma Summing Peak Correction of Volume Samples using PENELOPE/penEasy Monte Carlo Code. Poster.

- EURADOS Annual Meeting. Budapest, 10 – 13 February 2014.
  - Anna Camp and Arturo Vargas. Ambient Dose Equivalent Rate (H*(10)) Calculation from $LaBr_3$(Ce) Spectra. Oral presentation.
  - Anna Camp, Arturo Vargas, Natalia Alegria, Fernando Legarda, Alexander Clouvas, Sthelios Xanthos, Costas Potiriadis, Georgios Takoudis and Begoña Quintana. Comparison of Monte Carlo Simulation Codes for a LaBr3(Ce) Detector. Oral presentation.

- EURADOS Annual Meeting. Dubrovnik, 9 - 11 February 2015.
    - Arturo Vargas and Anna Camp. A One Year H*(10) Analysis using Stripping Method for a 1" x 1" LaBr3(Ce) Monitor in Barcelona. Oral presentation.
    - Arturo Vargas and Anna Camp. First MC Simulations to Study the Response of a 1" x 1" LaBr3 Monitor for Ground Deposited Artificial Radionuclides in Barcelona. Oral presentation.
    - Arturo Vargas and Anna Camp. Preliminary Results of a Helicopter UAV (3" x 3" NaI) Flight Campaign. Conclusions and Next Steps. Oral presentation.

- International Committee for Radionuclide Metrology 2015. Vienna, 8 – 11 June, 2015.
    - Anna Camp, Arturo Vargas andJosé M. Fernández-Varea. Determination of $LaBr_3$(Ce) Internal Background using a HPGe Detector and MC Simulations. Poster.

- International Conference Environmental Radioactivity 2015. Thessaloniki, 21 – 25 september 2015.
    - Anna Camp, Arturo Vargas, Maria Roig, Maria Amor Duch, Mercé Ginjaume and Ulrich Stöhlker. Ambient Dose Equivalent Rate Response of Gamma Spectrometry Monitors in the Framework of MetroERM European Project. Poster.
    - Claudia Grossi, Arturo Vargas, Anna Camp, José Enrique Martín, Josep Anton Morgui, Juan Pedro Bolivar and Xavier Rodó. Spanish Outdoor Radon Monitoring Network to Study the Behaviour of $^{222}Rn$ over Spain. Poster.
    - Arturo Vargas and Anna Camp. Response Study of a 1" x 1" Spectrometry Dose Rate LaBr3 Monitor for Ground Deposited Artificial Radionuclides. Oral presentation.

Participation in research projects:

**Competitive project**: Yes
**Title and code of the project**: Dosimetria i radiofísica mèdica. 2014 SGR 846
**Funding body**: AGAUR. Agència de Gestió d'Ajuts Universitaris i de Recerca
**Main researcher**: Josep Sempau (Institut de Tècniques Energètiques)
**Start and end date of the project**: 01/01/2014 – 30/04/2017
**Start and end date of the participation**: 01/01/2014 – 31/12/2016

**Competitive project**: Yes
**Title and code of the project:** Metrology for radiological early warning networks in Europe. ENV57-REG2
**Funding body**: European Commission and EURAMET
**Main researcher**: Stefan Neumaier (Physikalisch-Technische Bundesanstalt)
**Start and end date of the project**: 01/06/2014 – 31/05/2017
**Start and end date of the participation**: 01/06/2014 – 31/12/2016

# Index

# 1 General Introduction

## 1.1 Introduction

Gamma spectrometry is the study and analysis of the spectra produced by gamma emission of certain radionuclides. The energy of emitted gamma particles is characteristic of each radionuclide so gamma spectrometry allows the identification of radioactive sources, even in cases of mixtures of various isotopes.

We are exposed to radioactivity in the environment due to cosmic radiation and natural radionuclides found in soil and rocks. Therefore, the natural dose rate received by the general public depends on both ground characteristics and site altitude. The average natural dose (worldwide) is 2.4 mSv (UNSCEAR, 2008): which comprises 1.26 mSv due to radon inhalation, 0.48 mSv due to external terrestrial radiation, 0.29 mSv due to ingestion and 0.39 mSv due to cosmic radiation. It is important to ensure that certain limits are not exceeded, and this is the task of radiation environmental monitoring. There are two types of radiation surveillance networks, real time monitoring networks and networks that consist of sampling stations. The first type of network consists of automatic stations which continuously measure radiological variables; if a limit is exceeded, then the warning system is activated. These networks are also known as early warning networks. On the other hand, sampling stations perform periodic measurements; they take samples of soil, water, food... which are subsequently measured in laboratories. These measurements allow average radiological values to be established in certain areas and detect any change in trends. The National

Radiological Surveillance Network in Spain manages the Network of Automatic Stations (Red de Estaciones Automáticas - REA) as well as the Sampling Stations Network (Red de Estaciones de Muestreo - REM).

Typically, early warning networks include gamma dose rate monitors, while they do not have gamma spectrometry monitors. These measure the effects of gamma radiation, but do not provide any nuclide-specific information. The reason for using only dose rate monitors are both technical and economical. Up to now, most common detectors were high-purity germanium-type (HPGe) semiconductors with sodium iodine (NaI) scintillator-type monitors. HPGe crystals have great resolution, but require cooling which is a major drawback when being used in automatic stations. In addition, the high cost of such a semiconductor detector is another problem for installing them in surveillance networks. NaI crystals are better suited as they require lower maintenance, but their resolution is not so good e.g. they are not able to clearly distinguish between the natural radioisotopes $^{131}$I and $^{214}$Pb. However, new materials have been developed in the field of spectrometry research and implementation of gamma spectrometry detectors is being actively considered in many European networks (more than 5000). Some countries, such as Finland, have installed lanthanum bromide ($LaBr_3$:Ce) scintillator detectors at some of their surveillance stations close to nuclear power plants over the last few years.

In cases of radiological accident, such as Fukushima in 2011, real time information is essential in order to take decisions. However, in these circumstances there are large contaminated areas with high radiation levels, which makes it impossible to take in-situ samples or, at least, limits the time that workers can be exposed. Technological

advances allow the possibility of performing these measurements without compromising human lives. An active area of study at the moment is the use of unmanned aerial vehicles (UAV) equipped with measuring systems, controlled from a safe distance or with a pre-set flight plan.

## 1.2 Background

Technical advances in new materials that are sensitive to gamma radiation, such as $CeBr_3$, $LaBr_3$, $SrI_2$ and CdZnTe, lead us to think that in a few years' time existing radiological surveillance networks will be equipped with spectrometric detectors. Most probably they will be scintillator-type detectors due to their properties and market availability. In the following, a brief description of the physics behind scintillators is given.

In addition to providing radionuclide identification, dose rate values can be obtained from measured gamma spectra. In the thesis two methods are used involving $LaBr_3$, which require detailed characterization of detector response. This can be obtained either experimentally or by using Monte Carlo (MC) simulations. The terms of ambient dose equivalent rate and MC simulations, which are used repeatedly in the dissertation, are introduced below.

### 1.2.1 Scintillator detectors

Scintillator detectors consist of a scintillator crystal, a material which produces photons in response to incident radiation, and a photomultiplier tube (PMT). A diagram is shown in Fig. 1.1.

The PMT has two electrodes, the anode and the cathode, inside a vacuum tube with a light input window. The cathode, also named the

photocathode, is coated with a photoelectron emissive material. When light enters the window, photoelectrons are emitted from the photocathode and they are attracted to the anode. Between photocathode and anode there is a dynode series which produces secondary emission that is, produces electron multiplication and a cascade effect which generate a stronger signal at the anode.

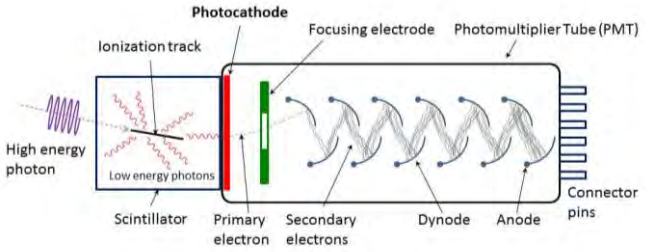


**Fig. 1.1.** Schematic showing incident high energy photon hitting a scintillating crystal, triggering the release of low-energy photons which are then converted into photoelectrons and multiplied in the photomultiplier (Scintillation counter, n.d).

The physics behind the scintillation process in the crystal is based on electron-hole pairs being created by lost gamma radiation energy. As described in Gilmore, 2008, primary electrons produced in this gamma ray interaction raise secondary electrons to the conduction band, thus leaving holes in the valence band. If the electron has not enough energy to move to the conduction band, both the electron and hole could remain electrostatically attracted which, in terms of the band structure model, could be interpreted as moving to an extra band just below the conduction band, as can be observed in Fig. 1.2. If this electron decays again to the valence band, it will emit electromagnetic radiation. If this radiation has or is close to optical

wavelength, it can be detected by a photomultiplier which sends a signal to the detector.

However, usually emitted photons are not in the visible range and the use of activators is required. Activators are impurities of a different element which incorporate extra levels within the forbidden band; the ground state of this activator lies just above the valence band and the excited states are somewhat below the conduction band. When an electron-hole pair is formed, the hole will tend to go to the ground level of the activator since the electrons will tend to be captured by its excitation levels. As shown in Fig. 1.2, these levels are closer and electromagnetic radiation produced during electron decay will be less energetic and so will be closer to the visible range. In addition, the wavelength will not match the absorption characteristics of the scintillator, thus favouring crystal transparency to emitted light.

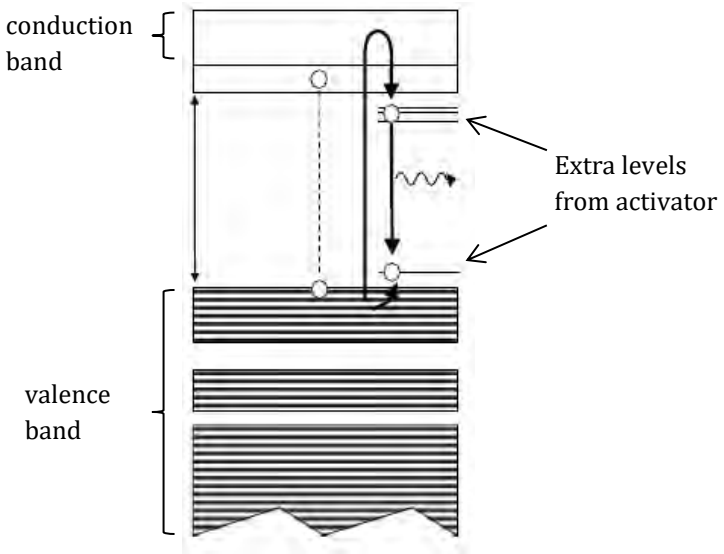


**Fig. 1.2.** Band gap structure scintillator (Gilmore, 2008).

Requirements for a scintillator detector for gamma-ray detection and spectrometry are the following:

- There must be a reasonable number of electron-hole pairs produced per unit gamma-ray energy.
- A material with high density and atomic number to ensure high stopping power for gamma radiation would be desirable.
- The response must be proportional to energy for spectrometry.
- The scintillator must be transparent to emitted light.
- The decay time of the excited state must be short to ensure high count rates.
- The material should have a reasonable cost.
- The refractive index of the material should be close to that of glass to allow efficient coupling to photomultipliers.

#### 1.2.1.1 Lanthanum Bromide crystals

Lanthanum Bromide crystals use cerium as an activator, and they are known as $LaBr_3(Ce)$. Specifically, in this study detectors used are *BrilLanCe™ 380* manufactured by the Saint-Gobain company with 5% of Ce.

$LaBr_3(Ce)$ detectors offer advantages over extended NaI. According to manufacturer's specifications:

- It has 1.6 times greater light output.
- Better resolution. It has 2.9 % at $^{137}Cs$ compared with 7 % of NaI.
- More efficient because of its higher density. BrilLance 380 has a density of 5.08 g $cm^{-3}$, compared with a NaI density of 3.67 g $cm^{-3}$.

- Scintillation decay time is much shorter, meaning that it can be used at much higher count rates.

A particularity of these crystals is their inherent radioactivity due to the presence of $^{138}La$ and $^{227}Ac$. This contamination produces a characteristic spectrum which can be measured, as is explained in this thesis, and must be taken into account in order not to overestimate measurements. The presence of $^{138}La$ cannot be avoided since it is a natural lanthanum radioisotope. However, in the case of $^{227}Ac$, its presence is due to chemical similitudes with $^{140}La$; newer crystals have substantially reduced the presence of this isotope thanks to a better refinement process.

### 1.2.2 Monte Carlo Simulation

Monte Carlo (MC) simulation was developed in the 1940s by scientists working on the atomic bomb program at Los Alamos National Laboratory. It is a mathematical technique based on the use of random numbers to solve problems that might have a deterministic solution. This method offers a solution to problems that are too complex to provide an analytical solution or where the number of independent variables would require an excessive amount of memory and computing time using conventional numerical methods. Its scope lies in all areas that have a probabilistic interpretation, thus it can be applied to informatics, economy, social studies, physical sciences…

In the case of radiation transport, the history of a particle is treated as a random sequence of free flights that end with an interaction event where the particle changes its final energy and momentum. Due to the randomness of the MC method only a few trials cannot be representative. However, after a large number of histories, physically interesting quantities can be statistically

estimated by sampling particle motion several times throughout all the random histories.

To simulate these histories an interaction model is needed, *i.e.,* a set of differential cross sections (DCS) for the relevant mechanisms. These DCSs determine the probability distribution functions of the random variables that characterize a track; 1) free path between successive interaction events, 2) type of interaction taking place and 3) energy loss and angular deflection in a particular event. This is widely described in PENELOPE (PENetration and Energy LOss of Positrons and Electrons, Salvat et al., 2011). A code for coupled electron-photon transport in arbitrary materials in a wide energy range spanning from a few hundred eV to about 1 GeV.

In this thesis the code PENELOPE was chosen as the Monte Carlo simulation code using penEasy (Sempau et al., 2011) as the main steering program. PenEasy is a modular code which includes a set of source models, tallies and variance reduction techniques that facilitates the modification of routines to user needs without having to change the main program.

### 1.2.3 Ambient Dose Equivalent Rate

Ambient Dose Equivalent Rate (ADER), $\dot{H}^*(10)$, is the dose equivalent that would be produced by the corresponding aligned and expanded field in the ICRU sphere at a depth 10 mm on the radius opposing the direction of the aligned field (IAEA, 2007). The ICRU sphere is a 30 cm sphere made of tissue equivalent material (Fig. 1.3).

It is an operational quantity and its unit is the sievert (Sv), 1 Sv = 1 J $kg^{-1}$. Actually the definition of ADER is theoretical and there is no monitor with an ICRU sphere within it. Dose rate monitors such as

proportional counters or ionization chambers, measure air-kerma ($K_{air}$) (absorbed dose ($D$)).

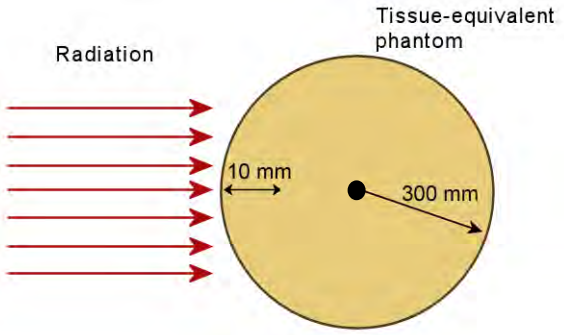


**Fig. 1.3.** Geometry to define the $H^*(10)$ with the ICRU sphere.

Absorbed Dose is the mean energy imparted by ionizing radiation to matter in a volume element of mass $m$. Its unit is the gray (Gy), 1 Gy = 1 J $kg^{-1}$. On the other hand, Kerma (Kinetic Energy Released per unit MAss) is the total initial kinetic energy of all charged particles set free by incident uncharged particles (photons, neutrons) per unit mass. Its unit is also the gray (Gy), and if the media studied is air, we say air-kerma. When there is charged-particle equilibrium and charged particles released by photons deposit all of their kinetic energy in the material, Kerma is a good approximation of absorbed dose. In practice, only at high energies (> 1 MeV) is there a difference between the two quantities due to bremsstrahlung radiation, which can cause an electron to deposit its energy away from the measuring point.

In order to convert from air-kerma to ADER the convention is to multiply by the factor 1.2 (Equation (1.1)), which is the conversion factor corresponding to gamma energy of 661.6 keV ($^{137}Cs$). In Fig. 1.4 are plotted conversion factors for monoenergetic photons. It can be observed that above ~600 keV, the function reaches a plateau.

However, at low energies using this 1.2 value would lead to inaccuracies.

$$H^*(10)[Sv] = 1.2\ [Sv/Gy] * K_{air}\ [Gy] \quad (1.1)$$

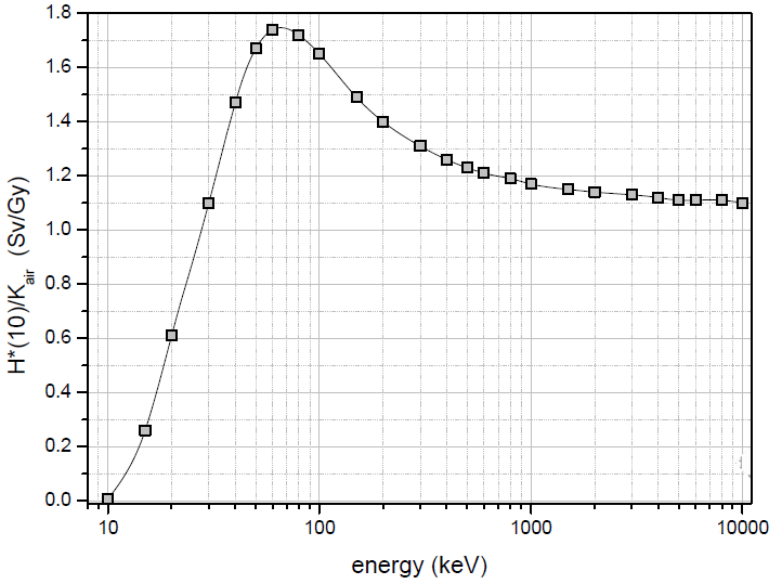


**Fig. 1.4.** Conversion air kerma – ambient equivalent dose (ISO 4037-3, 1999)

## 1.3 Research collaboration groups

Cooperation and networking among research groups is essential to share knowledge and take decisions that could have important consequences. Each country has sovereignty over radiological limits and surveillance networks. However, there are cross-border institutions which make recommendations with the aim of standardizing values and measurements from all radiation protection agencies.

Our institute collaborates with the European Radiation Dosimetry Group (EURADOS), which promotes scientific and technical research and development in the field of ionizing radiation. One of its main goals is to achieve harmonization among surveillance networks. There are several working groups, one for each research area and this PhD was done in the framework of WG3, the environmental dosimetry group. Thanks to this collaboration our group has had the possibility of obtaining a 1" x 1" $LaBr_3$(Ce) detector and a proportional counter-type dose rate monitor from the BITT Company installed on the roof of our institute.

This PhD has been developed also within the framework of the European Project "Metrology for Radiological Early Warning Networks in Europe (MetroERM)". This project aims to achieve harmonization of dosimetry early warning networks on the basis of development of a new generation of detectors based on spectrometers. During this PhD and within the framework of the first goal of the project, $LaBr_3$(Ce), CZT and $CeBr_3$ detectors were studied and characterized by using experimental irradiation and MC simulations. In addition, our group participated in an intercomparison study at the PTB (Physikalisch-Technische Bundesanstalt) and in a measurement campaign at the ESMERALDA station belonging to the CIEMAT (Centro de Investigaciones Energéticas, Medioambientales y Tecnológicas).

## 1.4 Thesis aims

The aim of this dissertation is the improvement of early warning monitoring stations by using gamma spectrometry. In this thesis the $LaBr_3$(Ce) detector was selected as the reference instrument to study the possibility of installing it in early warning networks. The reasons

for its choice were its resolution, which improves from 7 % to 3 % at 662 keV, its availability and the fact that these detectors are already being used at institutions such as STUK, the nuclear safety authority in Finland. In this framework, the objectives of the thesis are the following:

- Characterization of selected monitors. The energy linearity, the angular response, the dose rate response and energy resolution of the $LaBr_3$(Ce) detectors will be determined. The study of inherent background and the influence of cosmic radiation in these crystals must be also determined to properly analyze measured spectra.
- Definition of detector geometry and materials of the selected monitors to be used in MC simulations. Thus, characterization of $LaBr_3$(Ce) monitors in maximum detail is required in order to study detector response to any energy and incident angle of the photon.
- Development and application of methodologies to calculate $H^*(10)$ from the measured spectra by the $LaBr_3$(Ce) monitors and comparison with classical dose rate monitors. The influence of radon progeny deposition during rainy events and their daily oscillations on $H^*(10)$ will be used to study the sensitivity of developed methodologies and to be compared with the classical dose rate monitors.
- Study of the $LaBr_3$(Ce) monitor response in the case of fresh deposited artificial radionuclides considering that the source of contamination was over a large surface area. This will be carried out according to background measurements at surveillance stations and simulation of freshly deposited artificial radionuclides.

- Viability analysis of using spectrometric monitors installed in unmanned aerial vehicles to avoid radiological risk to first responder in case of a nuclear or radiological incident.

In order to achieve these objectives the thesis is organized as follows:

- CHAPTER 2: The $LaBr_3(Ce)$ detectors used in the PhD are characterized in detail: there is a study of their energy linearity and resolution, angular response by irradiation at a reference laboratory at the Institute of Energy Technologies (INTE). In this Chapter also is studied the influence of cosmic radiations and the internal background by means of exposures in lakes, underground laboratories and the use of MC simulations.
- CHAPTER 3: Two different methodologies to obtain $\dot{H}^*(10)$ from the gamma-ray spectrum are compared and applied to several measurements. The *stripping method*, subtracts out all partial absorptions in the measured spectrum in order to calculate the $\dot{H}^*(10)$ value from the outcoming flux. The second method, the *conversion coefficients method*, divides the measured spectrum into energy regions and applies energy-dependent conversion coefficients to obtain $\dot{H}^*(10)$. Both methodologies have been applied to spectra acquired in long-term measurements at two stations, campus Sud in Barcelona and ESMERALDA in Madrid. The calculated $\dot{H}^*(10)$ were compared with measured data using classical dose rate monitors. Since, fortunately, there were no radiological emergencies during research for this thesis, $\dot{H}^*(10)$ diurnal and seasonal variations at these stations are studied from the

viewpoint of the influence of cosmic radiation and variations of $^{222}Rn$ daughter concentration. In this Chapter is also described an intercomparison campaign at PTB facilities to study both detector sensitivity and the accuracy of $H^*(10)$ calculated values.

- CHAPTER 4: In this chapter the response of the spectrometric monitor to freshly deposited artificial radionuclides is investigated. To simulate radionuclides deposition that would be detected during the first few hours in a surveillance network in the case of a radiological accident, the reciprocal method technique (Zähringer and Sempau, 1997) is combined with the detection probability of a $LaBr_3(Ce)$ monitor to obtain the expected gamma spectra in a reasonable computing time.
- CHAPTER 5: In order to provide improvements in radiation surveillance, it has been developed a prototype which uses a 3"x3" NaI detector installed in an RPAS helicopter (Remotely Piloted Aircraft Systems). The set-up and results obtained in preliminary flights are shown in this Chapter.
- CHAPTER 6: A summary of conclusions obtained in each chapter and general conclusions of the thesis are reported.

# 2 Instruments: Characterization and Calibration

## 2.1 Introduction

In this chapter the $LaBr_3$(Ce) detectors used in the dissertation are described. There are two non-commercial detectors with 1" x 1" crystals and one 1.5" x 1.5" commercial model.

One of the 1" x 1" detectors is installed in the facilities at our institute and it carries out continuous measurements on a 15-minute basis. The 1.5" x 1.5" detector, named SpectroTRACER from the Saphymo Company, was also installed in the institute facilities within the framework of the MetroERM project.

Characterization of these monitors includes the study of their energy linearity and resolution, angular response and determination of their internal background. The presence of $^{138}$La and $^{227}$Ac is typical in $LaBr_3$(Ce) crystals, and this inherent activity is extensively described in this chapter.

## 2.2 Monitor description

### 2.2.1 1" x 1" $LaBr_3$(Ce) - Monitor 1

The detector named Monitor 1 is a 1" x 1" $LaBr_3$(Ce:5%) scintillator from the Saint Gobain Company (http://www.crystals.saint-gobain.com/Scintillation_Materials.aspx) coupled to a photomultiplier tube (PMT) model XP2060B. All this assembly, including the high-voltage (HV) and the Multi-Channel

Analyzer (MCA), is protected with an external aluminium housing which allows outdoor continuous measurement (Fig. 2.1) to be performed. The probe belongs to the BfS, who kindly provided it to us as part of the WG3 – Ambient Dosimetry EURADOS group study. It is currently installed at 1 m height on the roof of the INTE facilities, at the South Campus of the UPC.

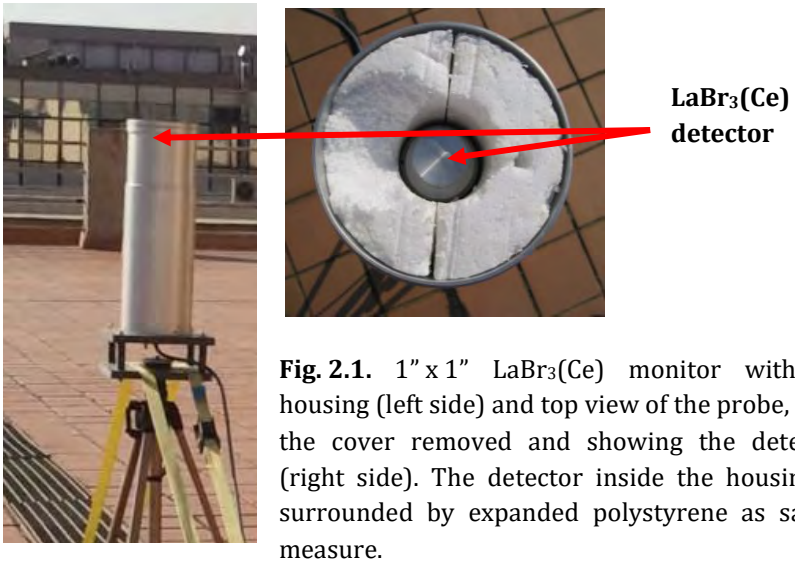


**Fig. 2.1.** 1" x 1" $LaBr_3$(Ce) monitor with its housing (left side) and top view of the probe, with the cover removed and showing the detector (right side). The detector inside the housing is surrounded by expanded polystyrene as safety measure.

The signal is processed by at low power digital pulse processor microDXP from XIA LLC (which includes both a digital spectroscopy amplifier and MCA functions. Fig. 2.2 shows a diagram of the connection between the microDXP and the computer. The detector high-voltage is controlled by the program 'DXP Control', developed by *Bundesamt für Strahlenschutz* (BfS), and operates at 470 V. MCA settings are controlled with microManager software from XIA LLC (see Fig. 2.3). It runs on Windows and, unless otherwise indicated, the main parameters are shown in Table 2.1. The detector is set to 2048 channels and an average bin width of 2.3 keV; the energy threshold

was established at approximately 40 keV to prevent the noise observed in the first channels (see section 2.3.1).

In order to work on a continuous measurement basis, essential in environmental monitoring, a home-made program was developed. The software runs in the background, starting a new measurement when defined real (or live) time ends.

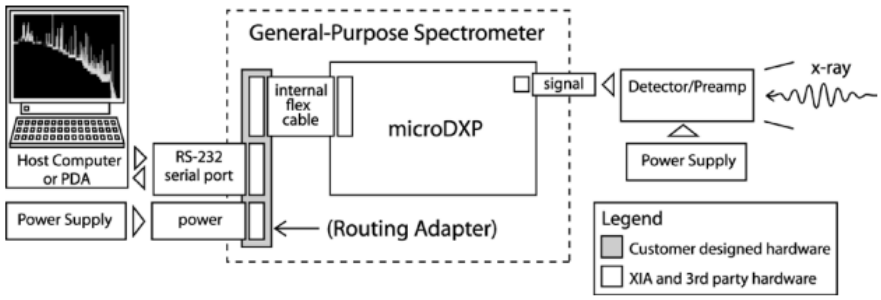


**Fig. 2.2.** A general purpose spectrometer with microDXP. A simpler user-designed Routing-adapter interface connects the microDXP to the host computer/PDA and power supplies (XIA LLC, 2009).

| Filter parameters | |
|---|---|
| Slow Length | 0.750 µs |
| Slow Gap | 0.750 µs |
| Peak Interval | 1.500 µs |
| Peak Sample | 0.750 µs |
| Fast Length | 0.500 µs |
| Fast Gap | 0.000 µs |
| Max Width | 1.625 µs |

**Table 2.1.** MCA filter parameters.

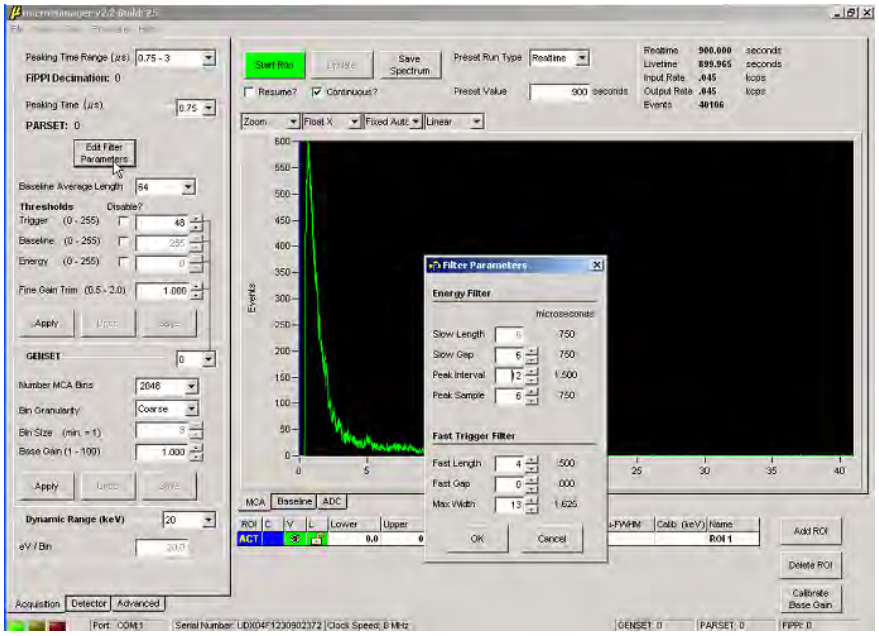


**Fig. 2.3.** Settings parameters stablished in the micromanager program to control the $LaBr_3$(Ce) detector.

## 2.2.2 1" x 1" $LaBr_3$(Ce) - Monitor 2

The detector denoted as Monitor 2 is a 1" x 1" $LaBr_3$(Ce:5%) scintillator from the Saint Gobain Company coupled to a photomultiplier tube (PMT) model R9420. It uses a prototype of a gamma ray analysis digital filter multi-channel analyzer named GMCA (Dambacher et al., 2011). All this assembly, including the high-voltage (HV) and the Multi-Channel Analyzer (MCA), is protected by a plastic housing developed at the INTE-UPC workshop and allows continuous outdoor measurements.

Apart from its main functions as digital MCA software, the GMCA controls the setting of the high voltage board. Data transfer with the PC is through a USB port and it also reports information on temperature due to the sensors in the probe. GMCA is able to work in

a Windows environment using a tool developed in Labview (Fig. 2.4). It also works in Linux. In this latter case, the monitor is controlled by a set of established Linux commands. Continuous measurements are normally carried out in the Linux mode.

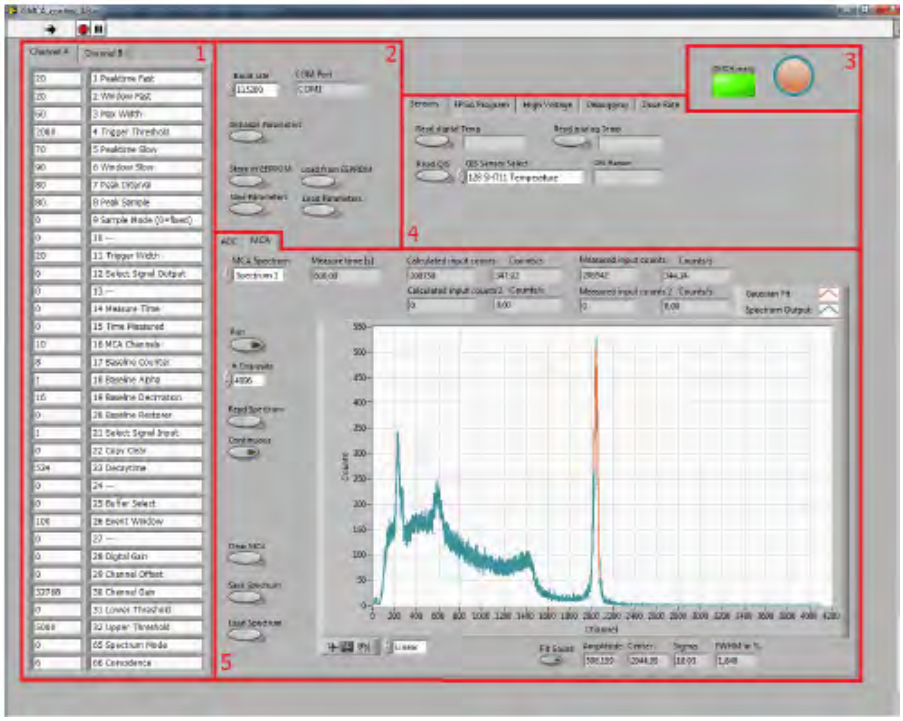

**Fig. 2.4.** Screenshot of the GMCA control software in Windows mode (Dambacher, 2011).

This monitor, unlike the previous one, has still not been installed at a fixed location for environmental monitoring, although it is planned to be installed at the Universidad de Huelva (UHU) in an immediate future. This means that there are no preferred settings and so different configurations have been used during this work, and are appropriately indicated according to the specific needs of each measurement.

### 2.2.3 1.5" x 1.5" $LaBr_3$(Ce) monitor - SpectroTRACER

The SpectroTRACER is a commercial monitor. It has been developed by Saphymo GmbH (http://www.saphymo.com) and the design includes NaI or $LaBr_3$(Ce) detectors of different sizes. It was designed for continuous environmental gamma contamination monitoring and it is intended to be used in early warning stations for radiological surveillance of air and/or ground contamination. The probe has an aluminium housing well suited for outdoors measurements and automatically provides gamma spectra, calculation of *H*(10)*, peak stabilisation, nuclide identification and it also includes the option to transfer data on-line.

As part of the MetroERM project, one task at our institute was the characterization of one SpectroTRACER with a 1.5" x 1.5" $LaBr_3$(Ce) detector.

## 2.3 Characterization of the monitors at LCD

The Calibration and Dosimetry Laboratory (LCD) at the INTE-UPC has been accredited by the Spanish National Accreditation Agency (ENAC) according to the ISO 17025 Standard. The lab has a photonic irradiator with different sources of $^{241}$Am, $^{137}$Cs and $^{60}$Co (Fig. 2.5), which have been used in this work to characterize the response of Monitor 1 and the SpectroTRACER. Monitor 2 is the same type of detector as Monitor 1, so the we considered that characterization was not needed.

**Fig. 2.5.** Photonic irradiator at LCD with one monitor prepared to be irradiated.

### 2.3.1 Dead time corrections

Irradiations at LCD could produce high count rates which require dead time corrections in spectra analysis. Dead time is the time after each event during which the system is not able to record another event. It therefore increases at high input count rates. Dead time can be defined as the ratio between the output count rate (OCR) and the input count rate (ICR):

$$Dead\ time\ in\ \% = \left(1 - \frac{OCR}{ICR}\right) x\ 100\% \qquad (2.1)$$

The microDXP processor and, similarly, the GMCA multi-channel analyzer, not only reports measured spectra, but also the measured input count rate ($ICR_m$) and the output count rate. According to the XIA LLC, (2009), measured counts ($N_{mi}$) in any spectral channel *i* can be related to the true number ($N_{ti}$) which would have been collected in the same channel *i* in the absence of dead time effects by:

$$N_{ti} = N_{mi} \cdot ICR_t / OCR \tag{2.2}$$

Where $ICR_t$ is the true input count rate, a higher value than the $ICR_m$, measured input count rate, reported by DXP because of the fast channel pile-up. The fast channel deadtime $\tau_{df}$ should be measured from a fit to Equation (2.3).

$$ICR_m = ICR_t \cdot exp(-ICR_t \cdot \tau_{df}) \tag{2.3}$$

Equation (2.3) can then be inverted and $ICR_t$ is obtained for each recorded spectrum from the reported $ICR_m$.

In Fig. 2.6, fast channel dead time ($\tau_{df}$) is adjusted from the fit at low dose rates, below 10 µSv $h^{-1}$, where dead time can be disregarded. The value obtained is $\tau_{df}$ = 0.5 µs.

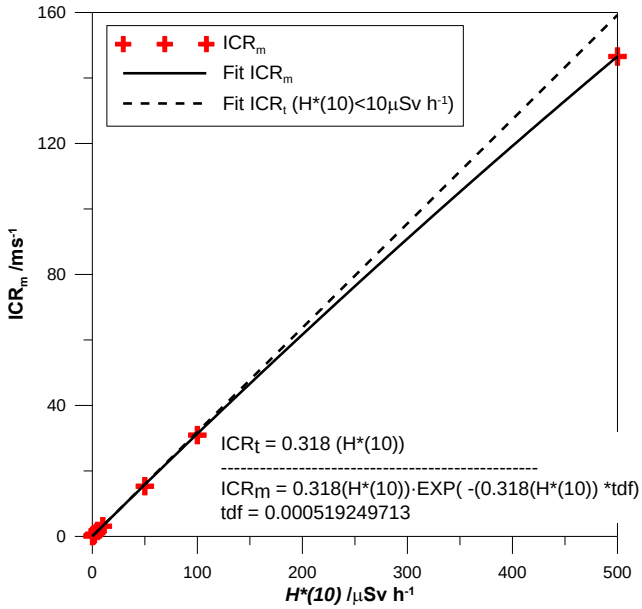


**Fig. 2.6.** Values of $ICR_m$ measured at different *H*(10)*. A linear fit at *H*(10)*<10 µSv $h^{-1}$, provides $ICR_t$. The fit of $ICR_m$ according to $ICR_m = ICR_t \cdot exp(-ICR_t \cdot \tau_{df})$, gives the fast channel dead time ($\tau_{df}$).

The correction in number of counts defined by Equation (2.2) can be affected by low energy noise produced by temperature variations which affects the ICR/OCR ratio reported by the monitor. The trigger threshold is fixed at approximately 40 keV to suppress these low energy contributions. Fig. 2.7 shows the effects of this noise during both the third week of May in 2014 and during 2015, in order to have similar temperature values. On the left side, the complete energy range was considered for 2014 and it can be seen that the ICR/OCR ratio follows daily temperature variations. On the right side, for 2015, the first few channels were suppressed and the ICR/OCR ratio remains almost constant, independent of temperature fluctuations.

The SpectroTRACER monitor shows corrected count rates together with both live time and real time readings. Live time readings should be used to obtain the count rate without underestimations.

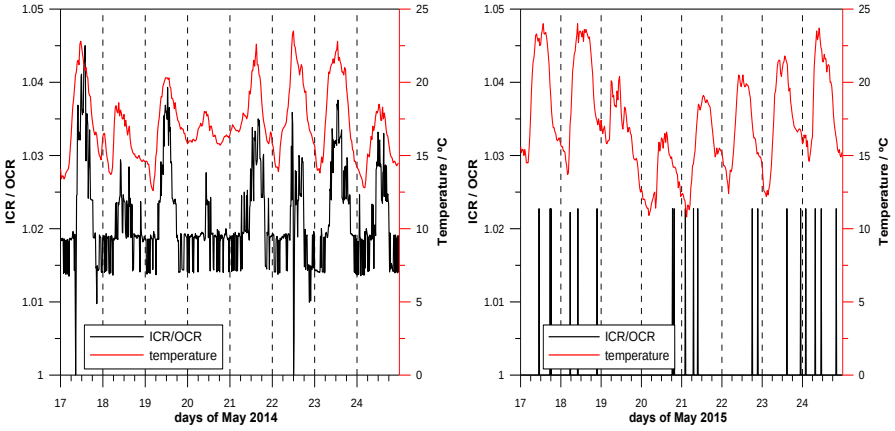


**Fig. 2.7.** ICR/OCR (black line) plot together with daily temperature variations (red line) during third week of May 2014 (left side), all energy range has been considered, and May 2015 (right side), first channels suppressed.

### 2.3.2 Angular response

The angular response was studied for the two monitors according to the geometry shown at the Fig. 2.8.

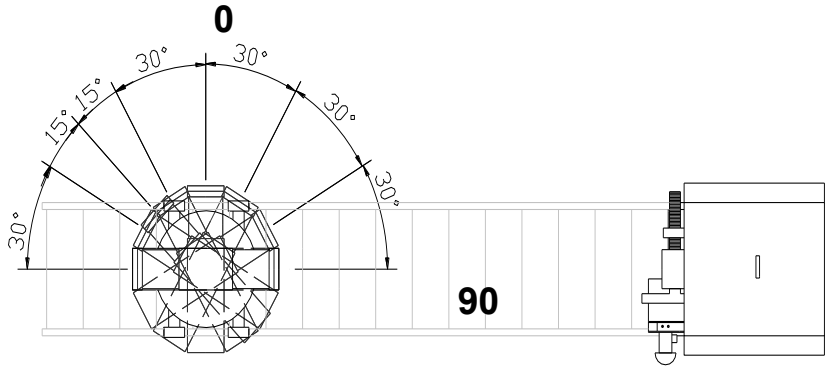


**Fig. 2.8.** Scheme of the irradiations performed at LCD with Monitor 1 and SpectroTRACER monitors to study the angular response.

In Fig. 2.9 the relative response of Monitor 1 (a) and the SpectroTRACER (b) are shown. Both detectors show almost an isotropic response from 90º to ~ -30º (330º), while after this breakpoint the efficiency drops to nearly zero at -90º (270º). The reason for this is the shielding produced by the electronics of the monitor, located in the lower part of the housing.

Differences between the top face and the lateral face, 90º and 0º respectively, are <2% for $^{137}$Cs and $^{60}$Co, while they are ~20% for $^{241}$Am in Monitor 1. For the SpectroTRACER, differences are <10% for $^{137}$Cs and $^{60}$Co, while they are ~25% for $^{241}$Am. These differences could be explained from the analysis of the detector full-energy peak efficiency (DE) described by Equation (2.4) (Saint Gobain Crystals, 2004).

$$DE = \frac{A}{4\pi R^2} \times \sum_i e^{(-\mu_i d_i)} \times \left(1 - e^{(-\mu_m x)}\right) \quad (2.4)$$

Where the first term is the fraction of all space that the detector subtends: $4\pi R^2$ is the area of the sphere covered by a point source emission if we consider a distance $R$ between the source and detector and $A$ is the area of detector face. The second term is the fraction of photons that reach the detector surface after being transmitted by the intervening $i$ materials, with attenuation coefficient $\mu_i$ and thickness $d_i$. The last term is the fraction of photons absorbed by the detector, where $\mu_m$ is the attenuation coefficient of the crystal and $x$, the material traversed. Values of the third term are directly available from Fig. 2.10, which shows the percentage of absorbed gamma-rays depending on their energies and for several crystal thicknesses.

Gamma-rays from $^{241}$Am decay (59.6 keV) are completely absorbed by both crystals (black line on Fig. 2.10). In this case the third term of

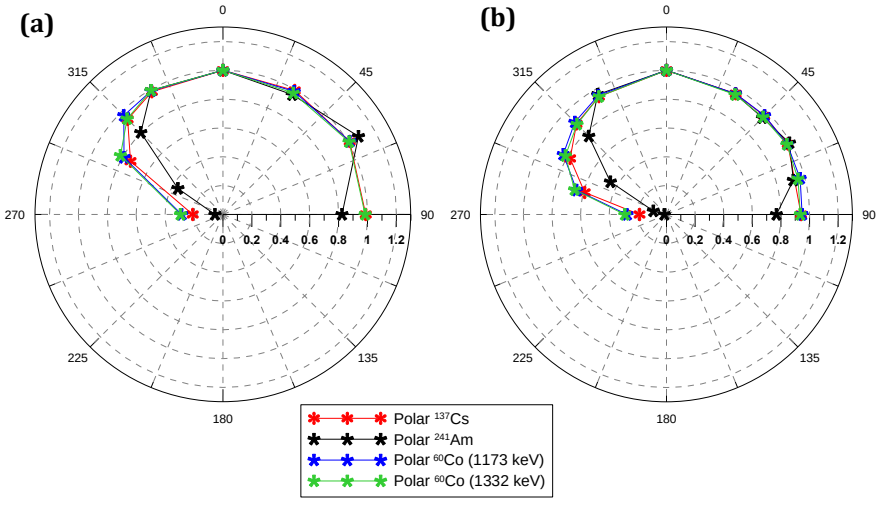


**Fig. 2.9.** Experimental relative response of (a) Monitor 1 and (b) SpectroTRACER at different angles of $^{137}$Cs, $^{241}$Am and $^{60}$Co sources.

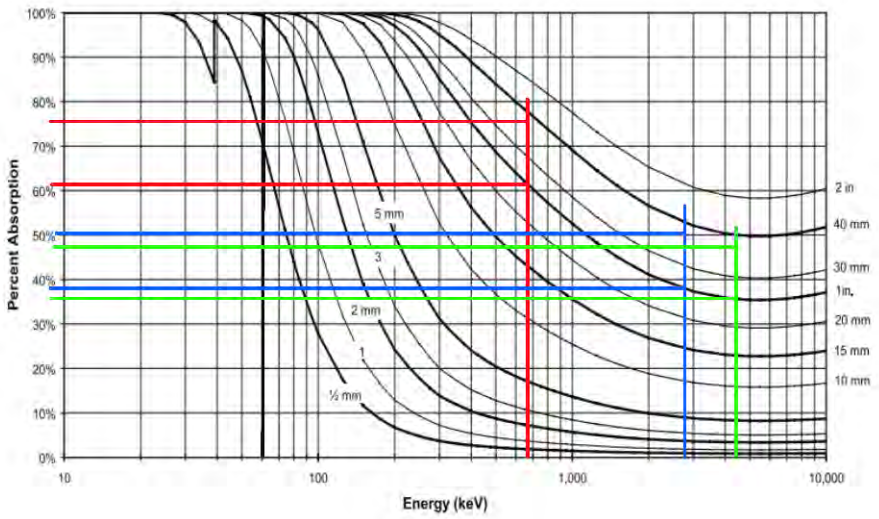


**Fig. 2.10.** Gamma and X-ray absorption efficiency for several thicknesses of BrilLance 380 material (Saint Gobain Crystals, 2004). Energies of $^{241}$Am (black line), $^{137}$Cs (red line) and $^{60}$Co (blue and green lines) are pointed for 1" and 1.5" thicknesses.

Equation (2.4) becomes 1. The area subtended by the cylindrical detectors is smaller by $\pi/4$ for the front surface (90º) compared with the lateral surface (0º). In other words, the efficiency should be 21.5% lower at the front surface due to geometrical reasons. In Fig. 2.9 it can be seen that the efficiency is ~20-25% lower at 90º than at 0º. However, gamma-rays from $^{137}$Cs (661.6 keV) and $^{60}$Co decays (1173.2 and 1332.5 keV) are not completely absorbed by the crystal (red, blue and green lines in Fig. 2.10). As a consequence, according to the third term in Equation (2.4), the main factor affecting absorption at low $\mu_m$ values is the distance travelled by photons inside the crystal. This factor is related to detector volume and is independent of incident direction. Therefore, the difference between angular response at 0º and 90º is minimized; more notably in the 1" x 1" crystal, which has lower absorption coefficients than the 1.5" x 1.5" crystal.

### 2.3.3 Detector response to *H**(10) rates

The response of detectors to different *H**(10) rates was studied using $^{137}$Cs sources. Monitor 1 was irradiated at 2, 10, 50, 200, 500, 700 and 1500 μSv h$^{-1}$ while the SpectroTRACER was irradiated at 2, 10, 50, 200, 2000 and 5000 μSv h$^{-1}$. Rates were adjusted by changing the source strength and monitor position in the LCD.

Results are plotted in Fig. 2.11. On the left side there is the measured response for the 1" x 1" monitor and, on the right side, there is the response for the 1.5" x 1.5" monitor, the SpectroTRACER. It should be noted that above 1 mSv h$^{-1}$, both detectors start to show saturation in their response.

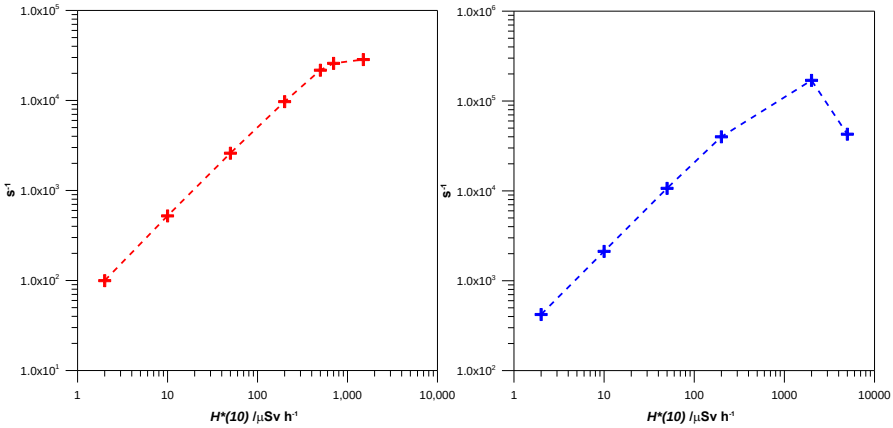


**Fig. 2.11.** Counts per second for a $^{137}$Cs source at different ambient dose equivalent rates (*H*(10)*) for Monitor 1 (left) and SpectroTRACER (right).

### 2.3.4 Energy linearity

Measurements were made using $^{241}$Am, $^{137}$Cs and $^{60}$Co sources to calculate the energy to channel conversion. For these measurements Monitor 1 was adjusted to 4098 channels while the SpectroTRACER was adjusted to 1024 channels. The difference in the number of

channels lies in the fact that measurements were performed separately in time, under different criteria. Anyhow, linearity in the response of both scintillators can be observed regardless of the number of channels.

Energy calibration for both monitors is shown in Fig. 2.12, which plots peak channel position versus photon energy of the sources (59.6, 661.6, 1173.2 and 1332.5 keV), for Monitor 1 (left) and SpectroTRACER (right). In both cases, the linear fit to each measured point shows an R-squared ~ 1, which means linear proportionality. Therefore, as will be shown in the next section, a linear energy calibration has been used for Monitor 1. SpectroTRACER is automatically calibrated and usually uses a second-order polynomial, although the non-linear term is proportional to $10^{-4}$.

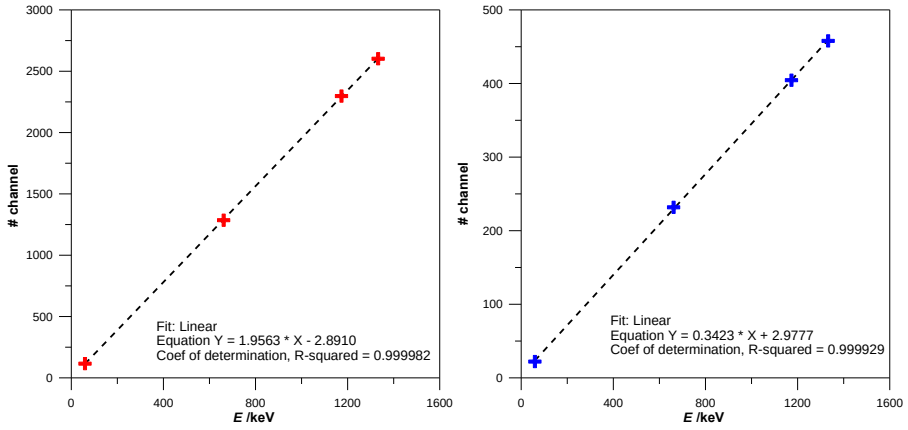


**Fig. 2.12.** Centroid channel versus the photon energy obtained for Monitor 1 (left) and SpectroTRACER (right).

## 2.3.5 Energy resolution

The energy resolution determines the ability of a detector to discriminate between γ-rays with close energies. It is defined as $\Delta E/E$,

where $\Delta E$ is the full width at half maximum (FWHM) of a photopeak occurring at the pulse-height $E$. Peaks in scintillator detectors are fitted by Gaussian functions, which means that FWHM can be defined as:

$$FWHM = 2.355\sigma \tag{2.5}$$

Where $\sigma$ is the standard deviation of the Gaussian curve.

The scintillator resolution ($R = FWHM/E$) can be estimated as (Dorenbos et al., 2004; Quarati et al., 2013):

$$R = R_{stat}^2 + R_{nPR}^2 + R_{inh}^2 \tag{2.6}$$

Where $R_{stat}$ is the contribution from the statistics in the number of photoelectrons ($N_{phe}$) produced in the crystal. $R_{nPR}$ is a contribution associated with the non-proportionality in the scintillation light yield with γ-rays or electron energy. $R_{inh}$ is associated with in-homogeneities in the crystal, the light reflector or the quantum efficiency of the photon detector.

The FWHM was evaluated from measurements at LCD. For Monitor 1, measurements using $^{241}$Am, $^{137}$Cs and $^{60}$Co sources were made, while for the SpectroTRACER measurements using $^{137}$Cs and $^{60}$Co were made. Results are plotted in Fig. 2.13. The best fit achieved (dotted line) is described by Equation (2.7) (Gilmore, 2008):

$$FWHM = aE + b\sqrt{E} \tag{2.7}$$

With a~0 and b = 0.8105, i.e, $FWHM = 0.8105\sqrt{E}$. This equation is in agreement with the equation obtained by Quarati et al., (2007).

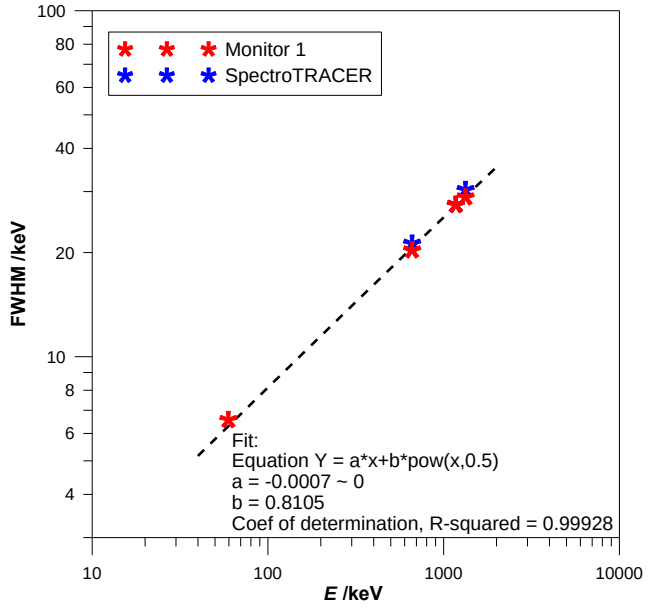


**Fig. 2.13.** Measured FWHM for the two monitors. Dotted line shows the best fit achieved.

## 2.4 $LaBr_3(Ce)$ energy calibration and spectra stabilization

Calibration of $LaBr_3(Ce)$ monitors requires special attention due to their known drift in energy calibration, mainly caused by the temperature sensitivity of the detector (Moszyński et al., 2006). Fig. 2.14 shows two typical spectra registered at the Campus Sud station using a $LaBr_3(Ce)$ crystal at 5ºC and 30ºC; peaks are located in high channels at low temperatures, while high temperatures shift peaks to positions in low channels. One common use of $LaBr_3(Ce)$ is in environmental gamma monitoring, where temperature fluctuates a lot. Therefore, this peak shift due to temperature is a main drawback because it can lead to problems in radionuclide identification.

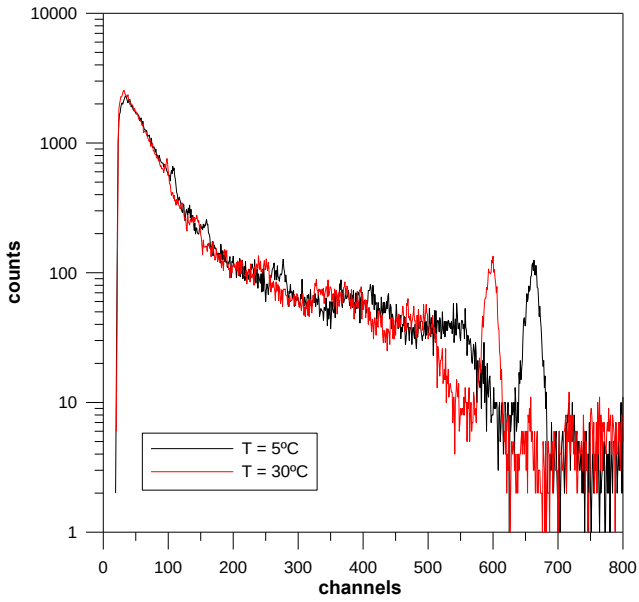


**Fig. 2.14** Natural background measured with a 1" x 1" $LaBr_3(Ce)$ crystal at $T$ = 5ºC and $T$ = 30ºC (acquisition time 1 h).

The position of a peak which has been shifted can be described by using a calibration reference, as shown in Equation (2.8).

$$C_{ik} = C_{i0} \cdot f(x) \tag{2.8}$$

Where $C_{i0}$ is the position of the $i^{th}$ channel in the reference calibration, $C_{ik}$ is the position of the $i^{th}$ channel in a shifted spectrum and *f(x)* is the function that describes the drift and is considered to be the same for all channels.

Only a reference peak is needed to determine the *f(x)* value (Casanovas et al., 2012). In $LaBr_3(Ce)$ detectors it is a common methodology to take advantage of the inherent $^{138}La$ radioisotope present in these crystals. $^{138}La$ decay has two branches (see Fig. 2.21). To correct channel shift, we are interested in the most probable decay (65.2%), i.e, decay by electron capture (EC) to the first excited level of

$^{138}$Ba followed by a 1435.8 keV γ-ray emitted in the de-excitation of $^{138}$Ba. This cascade decay inside the crystal produces a peak at approximately 1473 keV and an escape peak at about 1441 keV (see section 2.5.3). In addition, in this region there the natural radioisotope $^{40}$K (1460.8 keV) is also present. These three peaks are shown as a wide peak around 1470 keV in the spectra. However, to determine *f(x),* the three peaks may be taken into consideration.

Three Gaussian curves are used to fit the peaks. The mean ($\mu$) of each Gaussian (Equation (2.9)) indicates the channel position of the curve and, hence, it defines a correction function according to Equation (2.8). The final *f(x)* is defined as the average of the correction obtained from each peak (Equation (2.10)).

$$Gaussian\ function = \frac{A}{\sigma\sqrt{2\pi}} exp^{-(x-\mu)^2/2\sigma^2} \tag{2.9}$$

$$f(x) = \frac{f_{1441keV}(x) + f_{1461keV}(x) + f_{1473keV}(x)}{3} \tag{2.10}$$

According to the correction described by Equation (2.8), if the reference energy calibration for a spectrum is $E = E_0 + E_1*chan + E_2*chan^2 + \ldots$, the drift can be corrected by using Equation (2.11). The equation shows a polynomial of several degrees, but, as we have seen in the previous section, these monitors have a very linear response so a first degree polynomial is used in this study.

$$E(x) = E_0 + \frac{E_1}{f(x)} \times chan + \frac{E_1}{f(x)^2} \times chan^2 + \cdots \tag{2.11}$$

### 2.4.1 Gaussian fit of the $^{138}$La – $^{40}$K peak

Several software packages could be used to determine the best fit for this multiple peak. However, here the data interactive plotting program Gnuplot was selected (Williams and Kelley, n.d.). The fit command of Gnuplot uses a nonlinear least-squares Marquardt-Levenberg algorithm.

As is shown in Equation (2.12), the three peaks are fitted with three Gaussian functions plus a background line. Peaks 1441, 1473 and 1460.8 keV, are identified as peaks 1, 2 and 3, respectively. Fitting parameters $a_k$ refer to the Gaussian function amplitude ($A/\sigma\sqrt{2\pi}$) and $m_k$ parameters determine the Gaussian means ($\mu$). They are described in detail in sections 2.4.1.1 and 2.4.1.2. The full width at half maximum (FWHM) in this region is about ~2.1%, according to manufacturer (Saint Gobain, 2009) and the FWHM determined for these detectors (section 2.3.5). In other words, the required standard deviation for Gaussian functions is $\sigma \sim 13$ keV.

$$f(x) = \sum_{i=1}^{3} \frac{A_i(a_i)}{\sigma\sqrt{2\pi}} exp\left(-\frac{\left(x - M_i(m_i)\right)^2}{2\sigma^2}\right) + \left[counts_{-} + \frac{counts_{+} - counts_{-}}{ch_{+} - ch_{-}}(x - ch_{-})\right]^{*} \quad (2.12)$$

*The second term of *f(x)* is the background baseline. It is defined by linear interpolation between both sides of the multiplet area. Limits $ch_{+}$ and $ch_{-}$, depend on the position of peaks 1 and 2 according to the chosen *k* value.

#### 2.4.1.1 Number of counts in $^{138}$La peaks

According to several works (Camp et al., 2016; Menge et al., 2007) the specific activity of $^{138}$La in $LaBr_3$(Ce:5%) is 1.53 ± 0.07 Bq cm$^{-3}$. The study of the internal background using Monte Carlo simulations, extensively explained in section 2.5.3, enables individual information of the two $^{138}$La peaks to be obtained as is shown in Table 2.2.

| | 1441 keV peak | 1473 keV peak |
|---|---|---|
| ($s^{-1}$ $cm^{-3}$) from MC simulation | $(3.2\pm0.2)\cdot10^{-4}$ | $(4.8\pm0.2)\cdot10^{-4}$ |

**Table 2.2.** Amplitude of the 1441 keV and 1473 keV peak in the $^{138}$La. Uncertainties associated to both peaks have been obtained from uncertainty in $^{138}$La specific activity combined with uncertainties in MC simulation ($k$=2).

The ratio between both amplitudes is 1.5 ± 0.1, so that the amplitude of the 1441 keV peak (Equation (2.13)) can be defined based on the 1473 keV peak amplitude (Equation (2.14)). The *atan(x)* function ensures that the fitting parameter $a_2$ takes values according to uncertainty limits (see Fig. 2.15). Minimum and maximum values for $a_2$ are described by Equations (2.15) and (2.16), regarding the normalization factor $\sigma\sqrt{2\pi}$.

$$A_1(a_1) = \frac{1}{\pi}\left[\frac{1}{1.4}A_2(a_2) - \frac{1}{1.6}A_2(a_2)\right] \times \left(atan(a_1) + \frac{\pi}{2}\right) + \frac{1}{1.6}[A_2(a_2)] \quad (2.13)$$

$$A_2(a_2) = \frac{e^{a2max} - e^{a2min}}{\pi} \cdot \left(atan(a_2) + \frac{\pi}{2}\right) + e^{a2min} \quad (2.14)$$

$$a2max = ln(0.017\ [s^{-1}\ cm^{-3}] \times t[s] \times V[cm^3]) \quad (2.15)$$

$$\boldsymbol{a2min = ln\left(0.015\ [s^{-1}\ cm^{-3}] \times t[s] \times V[cm^3]\right)} \quad (2.16)$$

### 2.4.1.2 Location of the multiplet

Another boundary condition in order to fit the multiplet is the energetic distance between peaks. In the region of interest the program looks for the channel with the maximum number of counts. This channel is identified as the starting point for the fitting parameter $m_2$, the Gaussian mean of the 1473 keV peak.

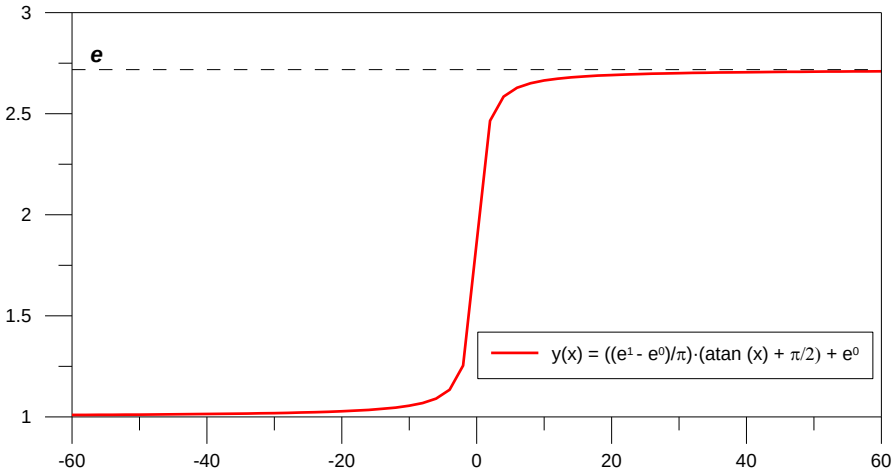


**Fig. 2.15.** Atan(x) function. For any *x* it returns a single value between $e^1$ and $e^0$, according to limits fixed by *y(x)*.

Gaussian means for the other two peaks, 1441 keV and 1460.8 keV, are fixed according to Equation (2.17), with fitting parameters *m1* and *m3* respectively. These parameters are allowed to take values in a certain range with limit values defined in equations (2.19), (2.20), (2.21) and (2.22). If we consider temperature as being the main reason for energy calibration drift, this range covers a temperature fluctuation from -20ºC up to +50ºC, in other words, *f(x)* takes values between 1.05 and 0.89 (Moszyński et al., 2006).

$$MM_i(m_i) = \frac{\left(m_2 - \Delta ch_+^{2-i}\right) - \left(m_2 - \Delta ch_-^{2-i}\right)}{\pi} \times \left(atan(x) + \frac{\pi}{2}\right) + \left(m_2 - \Delta ch_-^{i}\right) \qquad (2.17)$$

$$i = 1,3$$

$$MM_2(x) = m_2 \qquad (2.18)$$

$$\Delta ch_{+}^{2-1} = (1473\ keV - 1441\ keV)/E_1 \times f(x_{max}) \quad (2.19)$$

$$\Delta ch_{-}^{2-1} = (1473\ keV - 1441\ keV)/E_1 \times f(x_{min}) \quad (2.20)$$

$$\Delta ch_{+}^{2-3} = (1473\ keV - 1460.8\ keV)/E_1 \times f(x_{max}) \quad (2.21)$$

$$\Delta ch_{-}^{2-3} = (1473\ keV - 1460.8\ keV)/E_1 \times f(x_{min}) \quad (2.22)$$

### 2.4.2 Results of the fitting method

The fitting method defined in the previous section was applied to different spectra registered in different scenarios using Monitor 1, see Fig. 2.16. A zoom of the ~1470 keV peak region is shown in each plot providing the experimental spectrum (black dots) with its associated uncertainty (vertical bars) and the resulting fit (red line), using the three Gaussian curves. Spectrum (a) corresponds to a natural background spectrum registered on the roof of the INTE-UPC, with an acquisition time $t$ = 3600 s. Spectrum (b) was taken with the same acquisition time in the presence of $^{137}$Cs and $^{60}$Co sources, only the 1332 keV peak from $^{60}$Co is shown together with the $^{138}$La - $^{40}$K multiplet. Spectrum (c) was registered on a floating platform ($t$ = 3600 s) installed on a lake, at a distance to the shore of 100 m and with a water depth of 2.5 m - 3.5 m. This set-up, located at the Physikalisch-Technische Bundesanstalt (PTB), is used for cosmic measurements due to the low terrestrial contribution. Spectrum (d) is a background from the Underground laboratory for DOsimetry and spectrometry (UDO II), also at the PTB, at 430 m underground in a salt mine ($t$ = 4400 s) (more information on section 2.5).

Spectra a) and b) show a remarkable $^{40}$K peak (black curve) in addition to both peaks from $^{138}$La, 1441 keV and 1473 keV, because $^{40}$K is a natural radionuclide present both in building materials and soil. On the other hand, spectra (c) and (d) mainly show the internal

background contribution, since both measurement sites were isolated from natural radioactivity. The small remaining $^{40}$K peak observed in (c) and (d) has almost the same number of counts and is probably due to the presence of this radionuclide in the borosilicate glass of the PMT input window (Photonis, 2007).

Spectra from Fig. 2.16 are calibrated according to Equation (2.11),

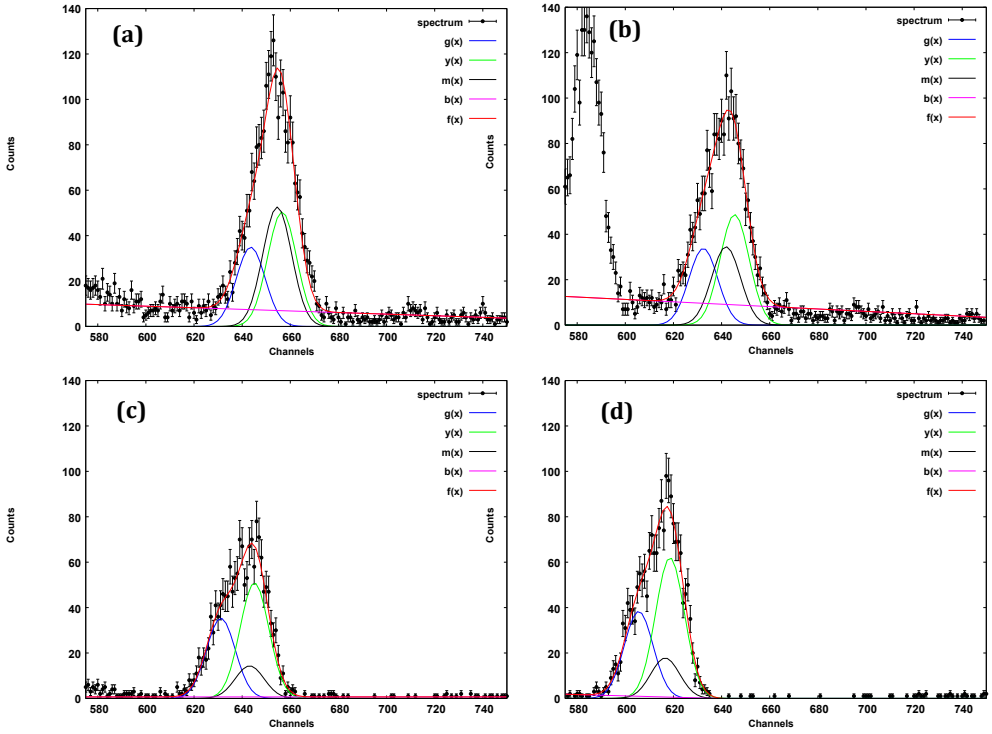


**Fig. 2.16.** $^{138}$La-$^{40}$K peak fit applied to several spectra measured with Monitor 1. (a) Spectrum registered at the roof of INTE ($t$ = 3600 s), (b) spectrum registered on free field with artificial sources ($t$ = 3600 s), (c) spectrum registered on a lake platform ($t$ = 3600 s) and (d) spectrum registered at UDO II with the monitor inside a lead castle ($t$ = 4400 s). Black line fits the $^{40}$K peak (*m(x)* function), blue and green lines fits $^{138}$La peaks, 1441 keV and 1473 keV respectively (*g(x)* and *y(x)* functions), pink line represents calculated background (*b(x)* function) and the red line represents the final fit curve (*f(x)* function).

and results are shown in Fig. 2.17. Spectrum (a) shows only a natural background, and the peak in the 1470 keV region is clearly distinguishable due to the presence of $^{138}$La. In spectrum (b) the peaks from the two artificial sources $^{137}$Cs and $^{60}$Co can be seen together with the $^{40}$K-$^{138}$La peak. Spectra (c) and (d), as has already been explained, were registered with almost no natural contribution so, they mainly show the internal background spectra of the crystal due to $^{138}$La. The peak at ~1470 keV shows the characteristic inset due to the escape peak at 1441 keV (more information in section 2.5.3).

The calibration equation is reported for each spectrum. In order to analyze the spectra, both the spectra and their calculated calibration equations were loaded into the GENIE2000 analysis software. Results obtained using the standard automated sequences for detecting peaks are reported in Table 2.3. It should be pointed out that the reference peak $^{40}$K - $^{138}$La is a multiple peak, but the program returns its centroid. The value for spectra (a) and (b), with natural background, is close to the $^{40}$K energy ($E$ = 1460.8 keV), while for spectra (c) and (d) the centroid is biased towards $E$ = 1470 keV.

| | **Peak energies /*keV*** | | | | | |
|---|---|---|---|---|---|---|
| | **$^{214}$Pb** | **$^{214}$Bi** | **$^{137}$Cs** | **$^{60}$Co** | **$^{60}$Co** | **$^{40}$K-$^{138}$La** |
| **(a)** | 354.32 | 604.61 | - | - | - | 1461.79 |
| **(b)** | 356.36 | 615.57 | 666.66 | 1172.94 | 1328.48 | 1461.01 |
| **(c)** | - | - | - | - | - | 1464.69 |
| **(d)** | - | - | - | - | - | 1466.68 |

**Table 2.3.** Analysis obtained with the GENIE2000 program applying to each spectrum their respective calculated calibration equation. Nomenclature to identify spectra is the same as in Fig. 2.16.

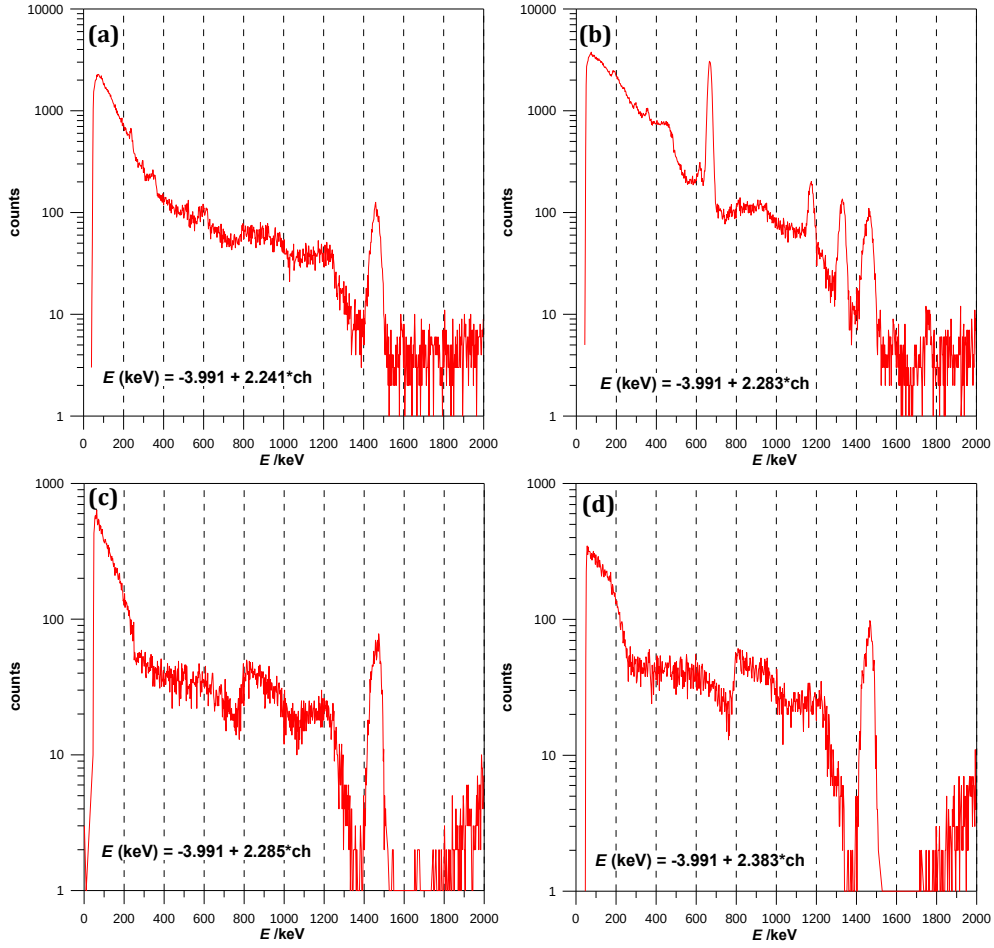


**Fig. 2.17.** Calibrated spectra registered with 1" x 1" $LaBr_3(Ce)$ monitor. Nomenclature to identify spectra is the same as in Fig. 2.16. Energy calibration obtained according to Equation (2.11) is reported.

## 2.4.3 Spectra stabilization

A representative example on how the spectra are corrected by applying the methodology mentioned above is shown in Fig. 2.18. It shows measured spectra both before and after applying the energy calibration methodology described above. The plot covers a time frame of 2 days in May and the temperature variations are natural daily oscillations. Each spectrum was registered over 900 s and the

measurement site was located on the roof of the INTE. The position of natural $^{40}$K mixed with $^{138}$La from the internal background shows a clear dependence on temperature. High temperatures produce a shift toward lower channels; conversely, low temperatures produce a displacement towards higher channels. After applying the correction, the line due to $^{40}$K - $^{138}$La, as in the case of the rest of spectra, maintains its position regardless of temperature variations.

### 2.4.4 Final considerations of the methodology

Both temperature correction and the subsequent energy calibration methodology are based on the identification of the three Gaussian peaks in the $^{138}$La – $^{40}$K region. If the spectrum is not wide enough and there are not enough counts to identify the peak, then the fit would not be possible. Fig. 2.20 shows an example of this case for a t = 2 min spectrum. In these situations, the recommendation is to sum enough sequential spectra in order to be able to identify the peak, and then apply the same energy calibration for all spectra.

Another consideration is when there are more peaks in the vicinities of the $^{138}$La – $^{40}$K peak. A common example is with a $^{226}$Ra source in equilibrium with its daughters, which produces peaks at $E$ = 1408 keV and $E$ = 1509.2 keV from $^{214}$Bi, among others, close to the region of interest for adjusting the spectrum. As is shown in Fig. 2.19, the reference peak is not so clear. In this situation the chosen solution was to fix the background limits ($ch_+$ and $ch_-$ in Equation (2.12)). Otherwise, counts belonging to nearby peaks will be considered, leading to fails in the fitting process.

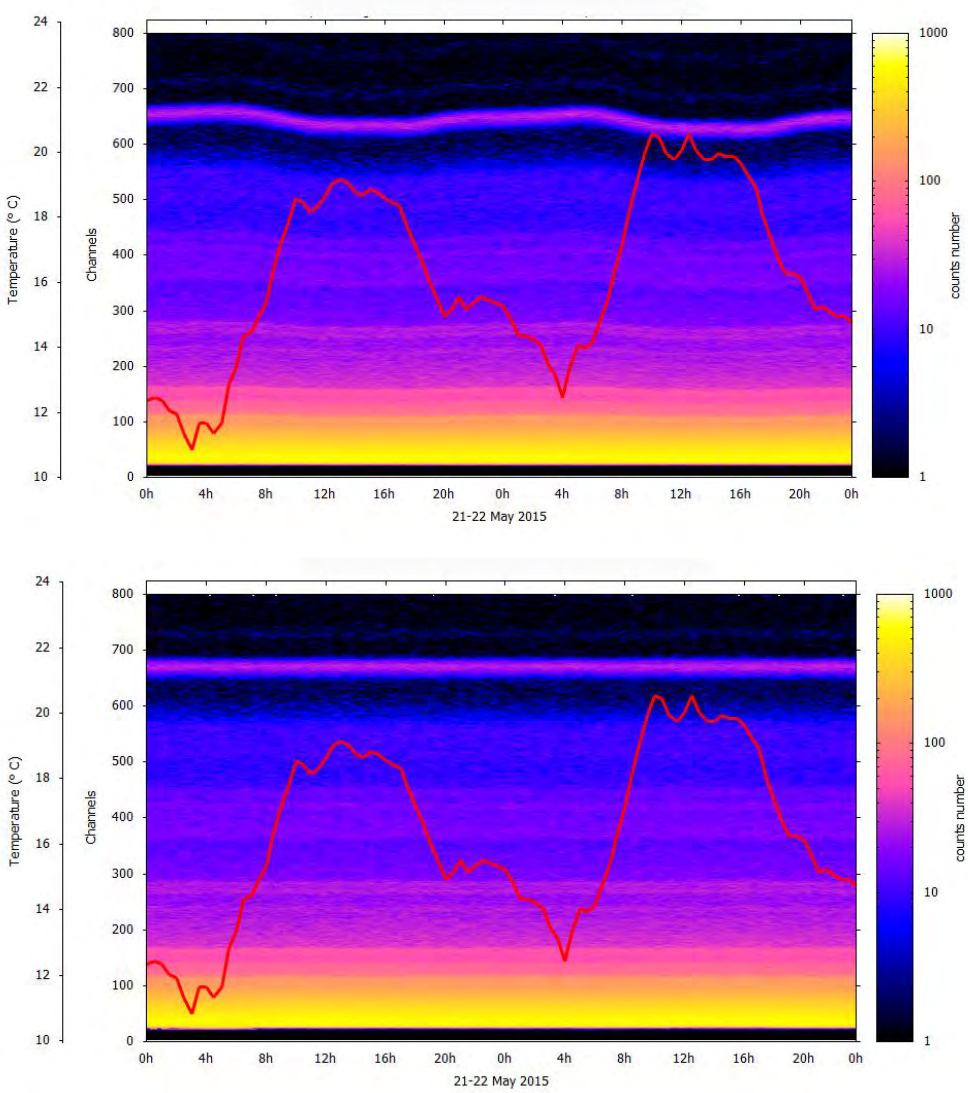


**Fig. 2.18.** Effects of temperature on spectra registered with 1" x 1" $LaBr_3(Ce)$ monitor 1. The raw spectra (top), before any correction, show dependence between channels position and temperature. In the corrected spectra (bottom) the peaks mantain the position regardless of the temperature.

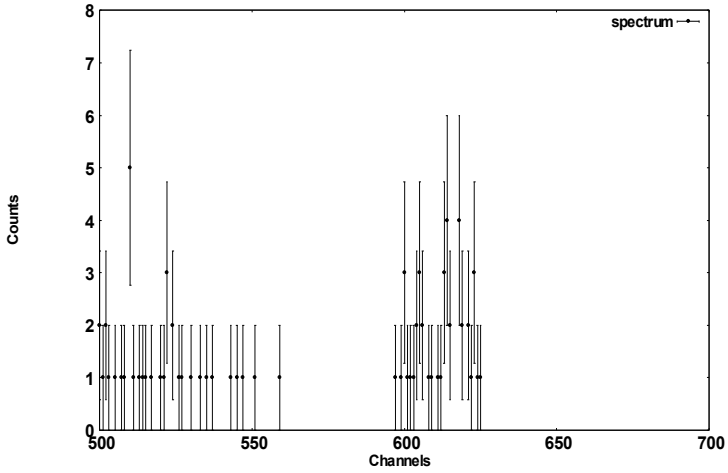


**Fig. 2.19.** Spectrum registered only during 2 min.

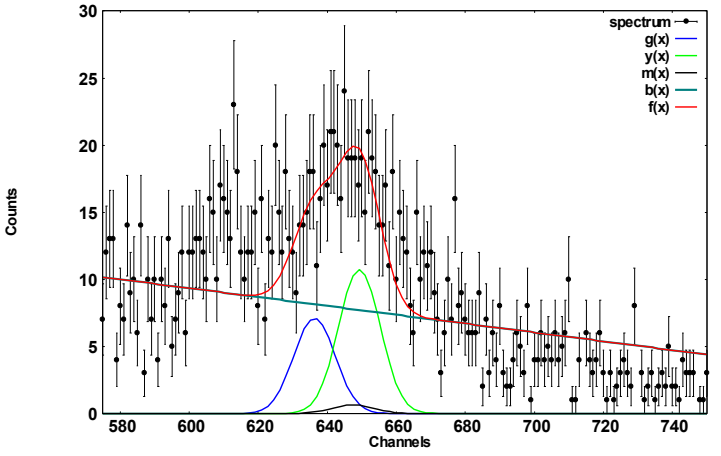


**Fig. 2.20.** Experimental spectrum obtained from $^{226}$Ra source ($t$ = 10 min).

## 2.5 Internal background

The $LaBr_3(Ce)$ crystals have an improved relative resolution (about 3 % at 662 keV) compared with commonly-used NaI(Tl) crystals (about 7 % at 662 keV). However, they have an internal contamination of $^{138}La$ ($T_{1/2} = 10^{11}$ years) and $^{227}Ac$ ($T_{1/2} = 21.77$ years) impurities, which produce a non-negligible background in the spectra and it supposes a disadvantage.

The decay of $^{138}La$ has two branches (see Fig. 2.21). The most probable one (65.2%) is electron capture (EC) to the first excited level of $^{138}Ba$ followed by a 1435.8 keV γ-ray emitted in the ensuing nuclear de-excitation. Besides, Ba Kα, Kβ, L and M characteristic x-rays (weighted average energies equal to 32.1 keV, 36.4 keV, 5 keV and 1 keV, respectively) are emitted in the course of the atomic relaxation induced by the EC. This cascade process occurs inside the crystal itself, so the binding energy of the captured electron in the K shell of Ba, 37.4 keV (Deslattes et al., 2003) adds with the γ-ray energy and produces a peak at 1473 keV. However, Ba K x-rays have a certain probability to escape from the detector, hence escape peaks are expected at 1441 keV. Nevertheless, due to the limited energy resolution, these peaks overlap and appear as a broad shoulder to the left of the main peak at 1473 keV. The other decay mode (34.8%) is a $\beta^-$ transition to the first excited level of $^{138}Ce$ and it has an associated β continuum that extends up to 258 keV and a γ-ray of 788.7 keV from the de-excitation of $^{138}Ce$. This cascade produces a shifted $\beta$ continuum between 788.7 keV and ~ 1047 keV.

The presence of $^{227}Ac$ is due to chemical similitudes with lanthanum as they belong to the same group in the periodic table. In

new crystals the content of this radionuclide has been reduced (Saint-Gobain Crystals, 2009) but not completely removed. $^{227}$Ac decays mainly by $\beta^-$ transition to $^{227}$Th, however detected energies are not due to β particles, because these energies are similar to ones from $^{138}$La decay and they are hidden by them, but from α particles of $^{227}$Ac daughters decay (Milbrath et al., 2005). These α particles are detected with a γ-ray equivalent energy in the range ~1600 keV – 3000 keV. Due to $T_1/_2$ of $^{227}$Ac makes this spectrum to be time-dependant.

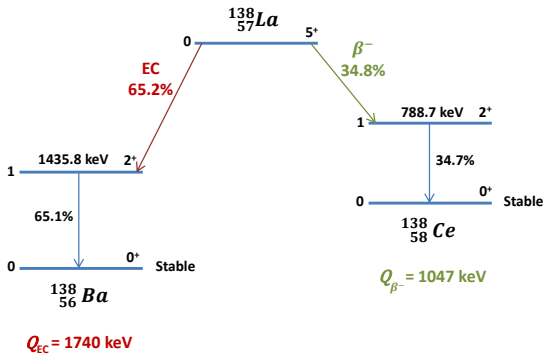


natural and artificial registered spectra and has a half-life of approximately $10^{11}$ years. Self-counting measurements may be carried out in underground ultra-low background laboratories to determine this internal background contribution. However, very few laboratories have access to such facilities.

In the following subsections, are shown the results of the internal background measurements in different scenarios. Moreover, is

described a novel method that employs a HPGe detector and Monte Carlo simulations to reproduce the background spectra caused by $^{138}La$ impurities, which would allow to determine 'in situ' the $LaBr_3(Ce)$ contamination.

### 2.5.1 Measurements on lakes

Main contribution to natural background in gamma spectrometry is due to radionuclides from $^{238}U$ (such as $^{214}Pb$ and $^{214}Bi$) and $^{232}Th$ (such as $^{228}Ac$, $^{212}Pb$ and $^{208}Tl$) decay chains, and $^{40}K$. These isotopes are present in soil and rocks and hence, they are detected in all measurements if no shielding is used.

To avoid this natural contribution, measurements could be performed over the water. If the shore and the bottom of the lake are far enough, the contribution of these natural radionuclides could be considered negligible and only the internal background and the influence of cosmic radiation would be measured.

#### 2.5.1.1 Banyoles lake

The lake of Banyoles is a natural lake (see Fig. 2.22) located ~120 km from Barcelona (42°07′31″N, 2°45′19″E). The lake is 2100 m by 750 m, with an average depth of 15 m that in several points is greater than 40 m.

Measurements were done 270 m from the shoreline and with a depth of more than 20 m. using a small rowboat of fiberglass. Spectra were registered with Monitor 2, since Monitor 1 was installed in a fix station at that time.


**Fig. 2.22.** Aerial view of the Banyoles lake (image obtained using Google Earth).

### 2.5.1.2 Edemissen lake

This lake is located ~15 km from PTB in Braunschweig (52°23'46.2"N, 10°20'59.4"E). It is 850 m by 200 m with an average depth of 2.5-3.5 m. In the middle of the lake, at ~100 m from the shore, there is one of the measurement sites of PTB, a floating platform made of rubber pontoons (see Fig. 2.23) used to study the cosmic radiation response of different types of dosemeters.

Measurements with the two 1" x 1" $LaBr_3(Ce)$ crystals, Monitor 1 and Monitor 2, were performed on the platform. Fig. 2.24 shows a comparison of the spectra obtained with each detector, it could be seen that the spectrum region due to $^{138}La$ is almost the same in both detectors, while the region of $^{227}Ac$ is different. This result is the one

expected, the specific activity of $^{138}La$ is almost constant for $LaBr_3(Ce)$ crystals with the same Ce doping (Camp et al., 2016); but that is not true for $^{227}Ac$, since it is time-dependant because of its short $T_{1/2}$.

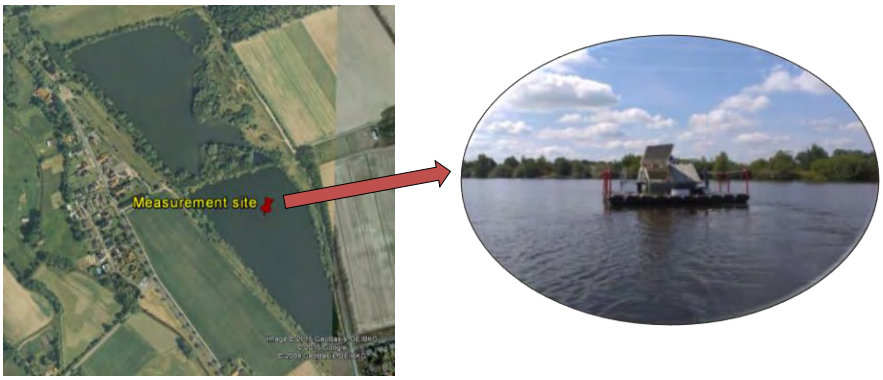


**Fig. 2.23.** Aerial view of the Edemissen lake (image obtained using Google Earth). The zoom shows a photograph of the floating platform.

It is remarkable to say that detector associated to microDXP spectroscopy system cuts-off low energies and, as a consequence, x-rays are not measured with this monitor.

A comparison of the spectra measured at both lakes is shown in Fig. 2.25. It could be observed that the count rate at low energies for the measurement performed at Banyoles lake is less than in the Edemissen lake. Right plot shows a zoom of the low energies region, the area above the baseline in the Edemissen spectrum (light grey) is greater than the area in the Banyoles spectrum (dark grey). The reason of this difference is mainly the value of cosmic radiation, as it will be shown in the next section 2.6. This leads to say that measurements at lakes remove almost all natural background, but not entirely.

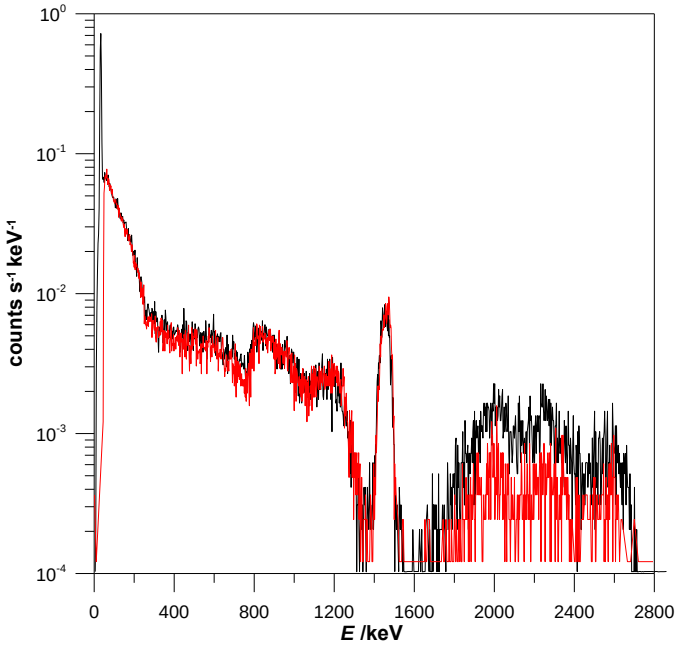


**Fig. 2.24.** Measurements performed on the lake platform with Monitor 1 (red line) and Monitor 2 (black line) ($t$ = 3600 s)

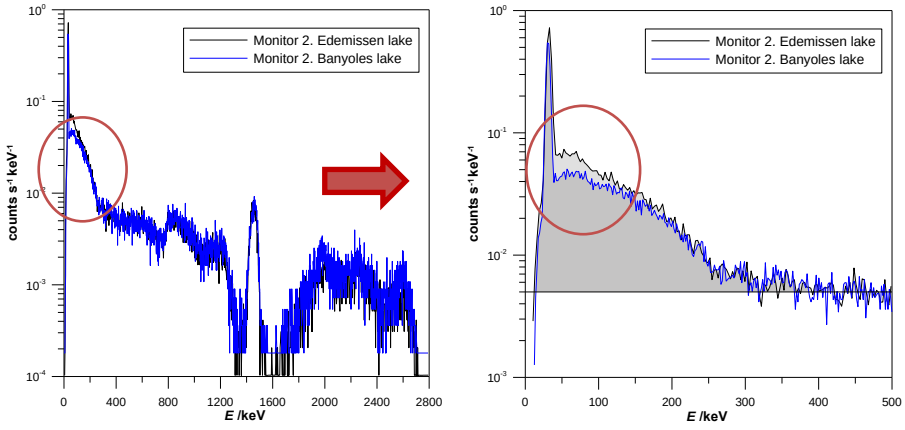


**Fig. 2.25.** Left plot show a comparison of the spectra measured by Monitor 2 in Banyoles and Edemissen lake. Right plot shows a zoom of the low energies region.

### 2.5.2 Measurements at low background laboratory (UDO II)

Low background laboratories remove almost entirely the natural background as well as the cosmic radiation. One of these laboratories, operated by PTB, is the Underground Laboratory for Dosimetry and Spectrometry (UDO II), located 430 m below ground in the salt mine of the *European Salt Company* (ESCO) in Grasleben. This laboratory replaced the old one UDO, in the Asse mine, installed first at -925 m level and after, at -490 m level (Neumaier and Dombrowski, 2014).

The low area dose rate of the background radiation, ~2 nSv $h^{-1}$, makes this laboratory well-suited to perform self-counting measurements of the $LaBr_3$(Ce) internal background. The calibration facility installed there, allows for studying the monitors response to photon radiation fields with low values of ambient dose rate. Fig. 2.26 shows an image of the UDO lab and the dose rate measured inside.


**Fig. 2.26.** Top imatge. The UDO II laboratory with photon calibration facility (Neumaier and Dombrowski, 2014). Bottom image. Lecture of the area dose rate meter in UDO II.

The internal background of both $LaBr_3(Ce)$ monitors was measured in a lead castle in order to subtract the possible remaining natural dose rate (Fig. 2.27). Results are shown in Fig. 2.28 together with spectra registered in the Edemissen lake. For both monitors the count rate reduction at low energies is noticeable, due to the absence of cosmic radiation. It can be observed that Monitor 1 does not show x-rays because of the threshold energy stablished.

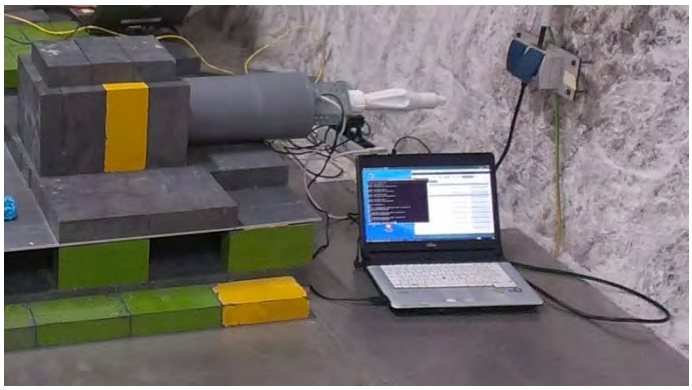

**Fig. 2.27.** Self-counting measurement with Monitor 2 in the lead castle at UDO II.

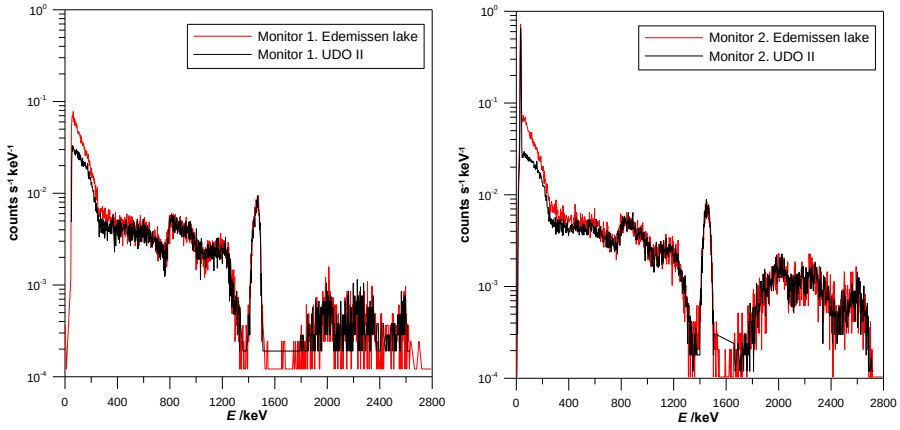


**Fig. 2.28.** Comparison of self-counting measurements performed at Edemissen lake and in the lead castle at UDO II with Monitor 1 and 2.

### 2.5.3 Internal background simulation

*This section in based on the publication Camp et al., (2015).*

Measurements at low background laboratories, like UDO II, provide better measurements of the internal background than measurements at lakes. However, very few laboratories have access to such facilities.

The following is a novel method that employs a HPGe detector and Monte Carlo simulation to reproduce the background spectra caused by $^{138}$La impurities, which would allow laboratories to determine 'in situ' the $LaBr_3$(Ce) contamination. The simulated background spectra have been compared with experimental spectra recorded at UDO and UDO II.

#### 2.5.3.1 Methodology

Since the decay of $^{138}$La comprises two γ-rays, the intrinsic radioactivity of the $LaBr_3$(Ce) crystal can be measured by gamma-ray spectrometry. The $^{138}$La activity is obtained according to the usual equation:

$$A = \frac{N_i}{t\, y_i\, \varepsilon(E_i)} \tag{2.23}$$

where $N_i$ refers to the number of counts accumulated in a particular peak $i$ of energy $E_i$ during the measurement time $t$, $y_i$ is the probability of emission of the particular $\gamma$-ray being measured and $\varepsilon(E_i)$ is the full-energy (FE) peak efficiency of the detector, which is calculated using MC simulations.

**Lanthanum-138 activity measurement with an HPGe detector**

To carry out the measurement of the internal activity in $LaBr_3(Ce)$, a high-purity germanium (HPGe) detector was employed. It consists of an eXtended Range (XtRa) coaxial germanium detector type p from Canberra; it has a relative efficiency larger than 40%, an endcap diameter of 83 mm and a crystal size of 61 mm × 59 mm ($\phi \times L$). The detector is surrounded by an external lead shielding to reduce background contributions with an internal copper layer that absorbs fluorescence x-rays from lead. The acquisition program used with this detector is the GENIE2000 software from Canberra.

The monitor selected to evaluate its $^{138}La$ content is a 1"×1" $LaBr_3(Ce:5\%)$ scintillator from Saint Gobain, which is coupled to a photomultiplier tube (PMT) model XP2060. The input window of the PMT is made of borosilicate glass (Photonis, 2007) and this implies the presence of $^{40}K$, which also contributes to the internal background and should therefore be evaluated as well.

To measure the $^{138}La$ activity in the 1"×1" $LaBr_3(Ce)$ detector, it was placed at a distance of 49.7 mm above the HPGe top window by means of a plastic spacer, as shown in Fig. 2.29. This distance decreases summing effects and reduces uncertainties in the efficiency determination. The $LaBr_3(Ce)$ crystal was protected laterally with foam. The most prominent features in the spectrum acquired during 59473 s with the HPGe detector were the 788.7 keV and 1435.8 keV peaks arising from the decay of $^{138}La$ and the peak at 1460.8 keV produced by $^{40}K$.

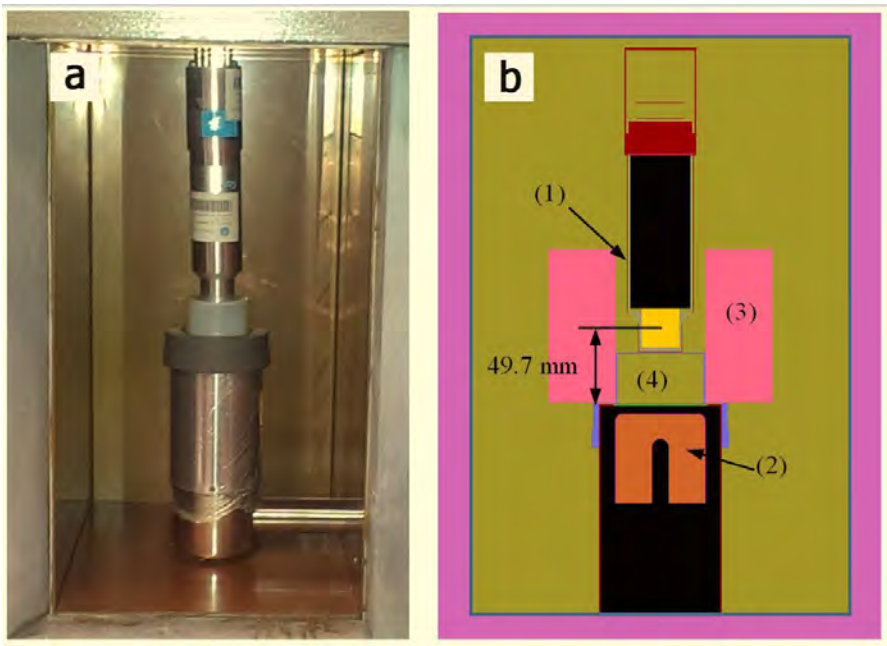


**Fig. 2.29.** (a) Picture of the $LaBr_3(Ce)$ monitor on the HPGe detector. The protection foam has been removed for better visualization of the set-up. (b) Two-dimensional section view of the $LaBr_3(Ce)$ and HPGe detectors, generated with PENELOPE's GVIEW2D visualization tool. It is shown the $LaBr_3(Ce)$ monitor (1), crystal in yellow colour, protected with foam (3) and located on a plastic spacer (4) which, in turn, is layed on the endcap of the HPGe detector (2).

### Monte Carlo calculation of the FE peak efficiencies

The FE peak efficiencies of the HPGe detector were obtained by MC simulations using PENELOPE (Salvat et al., 2011), a code for the coupled electron-photon transport in arbitrary materials in a wide energy range spanning from a few hundred eV to about 1 GeV. The core of the program is a set of Fortran subroutines. In this work, penEasy (Sempau et al., 2011) has been adopted as the steering main program, which includes a set of source models, tallies and variance-reduction techniques. penEasy is a modular code that facilitates the

modification of routines to user needs without having to change the main program. Coincidence summing effects had to be considered because the $^{138}$La background is within the detector crystal and cascade emission can produce sum peaks according to the decay scheme described above. Therefore, the penEasy subroutine that generates the initial state (position, energy, direction) of the particles was adapted to include the decay and cascade emissions of $^{138}$La in a similar way to that described in a previous work (Vargas et al., 2014).

The decay information introduced into the penEasy code was extracted from several databases. Transition probabilities assigned to each disintegration channel and nuclear de-excitation process were taken from the NUCLEIDE database (Bé, 2013). Internal conversion was disregarded due to its low probability ($\alpha \sim 10^{-3}$), thus only $\gamma$-rays have been simulated in the de-excitation paths of $^{138}$Ba and $^{138}$Ce. The Ba K and L x-rays emitted after EC were characterized having recourse to two databases to get the maximum information for x-ray energies and their probabilities, namely the National Nuclear Data Center (Sonzogni, 2003) and the Isotopes Project at the Lawrence Berkeley National Laboratory (Firestone and Ekström, 2004). The chosen cut-off emission probability to simulate Ba K x-rays is 1% and for L x-rays, which have low probabilities, the most probable transition is simulated, with an energy of 4.47 keV. In turn, the Fermi spectrum pertaining to the $\beta^-$ decay of $^{138}$La to $^{138}$Ce is displayed in Fig. 2.30. The considered theoretical models are (a) the Fermi spectrum generated by the EFFY program (Garcia-Toraño and Malonda, 1985) and (b) the energy distribution function predicted by the standard theory according to Quarati et al., (2012). These distributions are quite different, and both produce $\beta$ continua in the simulated background spectra which depart visibly from the

experimental ones. Apparently, theory encounters problems to model accurately forbidden $\beta$ transitions of high order like that proceeding from the ground level ($5^+$) of $^{138}$La to the first excited level ($2^+$) of $^{138}$Ce, see e.g.(Mougeot, 2015). Fig. 2.30 also includes the Fermi spectra reported by Quarati et al., (2012) (c) evaluated experimentally using a coincidence method and (d) extracted from measurement by means of numerical deconvolution. The two experimental energy distributions are similar, but the latter is in slightly better agreement with the measured spectra (see below) and is therefore preferable for the simulation of the internal background spectra.

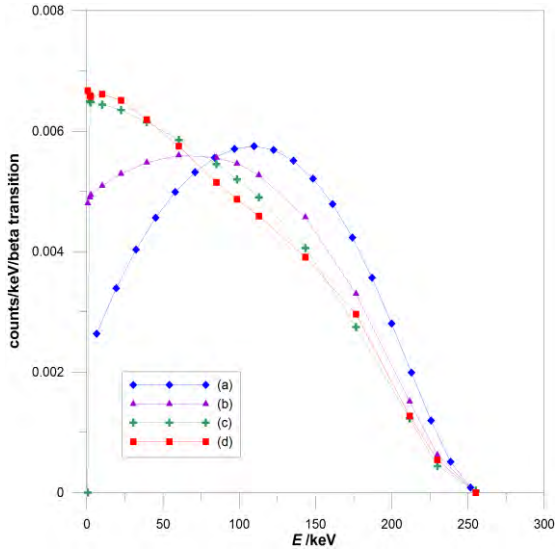


**Fig. 2.30.** Fermi spectrum of $^{138}$La. (a) Generated by the EFFY program (Garcia-Toraño and Malonda, 1985), (b) predicted by standard theory, (c) evaluated experimentally using a coincidence method, and (d) extracted from measurement by means of numerical deconvolution. The data belonging to curves (b), (c) and (d) have been taken from (Quarati et al., 2012).

The energy resolution (full width at half maximum, FWHM) of the detectors was characterized in order to convolute the simulated spectra and get peaks with realistic widths. The FWHM calibration was done with $^{241}$Am (59.5 keV), $^{137}$Cs (661.6 keV) and $^{60}$Co (1173.2 keV and 1332.5 keV) point sources with certified activities, purchased from Amersham, so as to cover the wide energy range found in environmental dosimetry. The peak width calibration function might be approximated according to Gilmore, 2008:

$$FWHM = \sqrt{a + bE} \tag{2.24}$$

The parameters for the 1" x 1" $LaBr_3$(Ce) scintillator are a = 0 and b = 0.657 keV, whereas those pertaining to the HPGe detector are a = 1.202 keV$^2$ and b = 1.84 x $10^{-3}$ keV.

In the MC simulations, the geometries of the $LaBr_3$(Ce) and HPGe detectors were defined following the specifications furn-ished by the respective manufacturers and using the PENGEOM package of PENELOPE. To validate these geometries we had re-course to the same radioactive point sources ($^{241}$Am, $^{137}$Cs and $^{60}$Co) employed for the FWHM calibration, assuming that point sources validation also hold for extended sources.

The geometry of the $LaBr_3$(Ce) detector included a 2.5-mm-thick external cylindrical aluminium housing that protects the detector in ambient monitoring. The sources were placed at a fixed distance of 50.6 mm from the aluminium housing and 74.5 mm from the detector top window. The experimental and simulated FE peak efficiencies, $\varepsilon_{exp}$ and $\varepsilon s_{im}$, are collected in Table 2.4. The combined uncertainties of the experimental efficiencies were estimated from the uncertainties of the activities of the point sources and the uncertainty of the net

number of counts of the FE peaks. The uncertainties of the simulated FE peak efficiencies combine in quadrature the type A (i.e. statistical) and type B contributions; the latter was assumed to be caused by a ±1 mm tolerance in the source-to-detector distance. The relative difference of simulated efficiencies compared to experimental results was reported as $100(\varepsilon_{sim}-\varepsilon_{exp})/\varepsilon_{exp}$. These differences are less than 5%. The largest deviation is 4.8% at 59.5 keV. This can be ascribed to small differences between the true and simulated geometries which have a greater effect on the efficiency at low energies owing to the higher attenuation of γ-rays in the absorbing layers. At high energies the relative discrepancies are at most 1.4%.

| Radionuclide | E /keV | $\varepsilon_{exp}$ | $\varepsilon_{sim}$ | Relative difference /% |
|---|---|---|---|---|
| $^{241}$Am | 59.5 | $4.36(36)\cdot10^{-3}$ | $4.57(24)\cdot10^{-3}$ | 4.8 |
| $^{137}$Cs | 661.6 | $9.2(8)\cdot10^{-4}$ | $9.2(5)\cdot10^{-4}$ | 0.0 |
| $^{60}$Co | 1173.2 | $4.4(6)\cdot10^{-4}$ | $4.46(19)\cdot10^{-4}$ | 1.4 |
| $^{60}$Co | 1332.5 | $4.0(4)\cdot10^{-4}$ | $3.96(12)\cdot10^{-4}$ | -1.0 |

**Table 2.4.** Experimental and simulated FE peak efficiencies of the 1"×1" $LaBr_3$(Ce) detector for point radioactive sources. Uncertainties are quoted with k = 2.

The verification of the HPGe geometry demands special care due to the dead layer of this detector, which has noticeable effects at low energies and whose thickness has to be defined experimentally because its value is not disclosed by the manufacturer. In this study the nominal value of dead layer was assessed to be 0.5 mm by measurements and Monte Carlo simulation, as it had been done previously in a similar way (Elanique et al., 2012; Huy, 2011). The aforementioned point sources were utilized again to check the HPGe geometry; they were located inside the lead shielding at 53.8 mm

from the detector top window. The experimental and simulated FE peak efficiencies are listed in Table 2.5; the relative deviation is less than 6%. As in the case of the $LaBr_3(Ce)$ detector, the largest discrepancy occurs at 59.5 keV. Examining the differences between measurements and simulation, it can be concluded that the defined geometries are valid for the present purposes.

| Radionuclide | E /keV | $\varepsilon_{exp}$ | $\varepsilon_{sim}$ | Relative difference /% |
|---|---|---|---|---|
| $^{241}Am$ | 59.5 | $4.53(36)\cdot10^{-2}$ | $4.27(5)\cdot10^{-2}$ | -5.7 |
| $^{137}Cs$ | 661.6 | $1.02(8)\cdot10^{-2}$ | $1.030(11)\cdot10^{-2}$ | 1.0 |
| $^{60}Co$ | 1173.2 | $6.4(5)\cdot10^{-3}$ | $6.55(13)\cdot10^{-3}$ | 2.3 |
| $^{60}Co$ | 1332.5 | $5.7(5)\cdot10^{-3}$ | $5.89(6)\cdot10^{-3}$ | 3.3 |

**Table 2.5.** Experimental and simulated FE peak efficiencies of the HPGe detector for point radioactive sources. Uncertainties are quoted with k = 2.

Once the geometries of the two detector are properly defined, the experimental set-up with the $LaBr_3(Ce)$ and HPGe detectors explained above was simulated, as it is depicted in Fig. 2.29b. The contamination in the $LaBr_3(Ce)$ crystal was defined as an extended source of $^{138}La$ homogeneously distributed inside the crystal and the $^{40}K$ contamination was regarded as an extended source spread in the PMT window. The output of the modified PENELOPE/penEasy program is detection probability in each energy bin per disintegration, that is, the MC FE peak efficiency ($\varepsilon_{MC}$). Since the geometry and the efficiency of the HPGe detector have been validated, $\varepsilon_{MC}/y$ can be identified with the FE peak efficiency of the measurement.

### 2.5.3.2 Results

**Internal $^{138}$La activity in the $LaBr_3$(Ce) crystal**

The $^{138}$La activity was determined from the ratio of the areas of the 788.7 keV and 1435.8 keV peaks detected experimentally to the simulated efficiency, i.e, $\varepsilon_{MC}$. The activity of 40K was deduced from the 1460.8 keV peak. Table 2.6 summarizes the results for the three peaks, *N* are counts measured with the HPGe detector during an acquisition time t, and $\varepsilon_{MC}$ is the calculated FE peak efficiency. As $^{138}$La emits two γ-rays, its activity was taken to be the weighted average value of the activities extracted from the 788.7 keV and 1435.8 keV peaks. The uncertainties of the experimental peak areas were estimated from the uncertainty of the net number of counts. As in the previous section, the uncertainties of the simulated peaks include type A and type B contributions. The combined uncertainties of the activities were calculated applying the error propagation law and for the mean value of $^{138}$La, the uncertainty of the weighted average is given. It can be pointed out that the $^{138}$La activity obtained for our 1" x 1" $LaBr_3$(Ce) detector is 19.7(9) Bq, i.e. 1.53(7) Bq cm$^{-3}$. This value is in excellent agreement with the expected 1.5 Bq cm$^{-3}$ $^{138}$La content in 5% doped $LaBr_3$(Ce) crystals (Menge et al., 2007).

| $E$ /keV | $N/t$ /s$^{-1}$ | $\varepsilon_{MC}$ | $A(^{138}La)$ /Bq | $A(^{40}K)$ /Bq |
|---|---|---|---|---|
| **788.7** | 4.74(20)·10$^{-2}$ | 2.35(13)·10$^{-3}$ | 20.0(14) | |
| **1435.8** | 5.88(21)·10$^{-2}$ | 3.03(15)·10$^{-3}$ | 19.5(12) | |
| **1460.8** | 9.6(10)·10$^{-3}$ | 3.07(15)·10$^{-4}$ | | 32.6(37) |
| | | $\langle A \rangle$ = | 19.7(9) | 32.6(37) |

**Table 2.6.** Activity of $^{138}$La and $^{40}$K in a 1"×1" LaBr3(Ce) crystal and its PMT, respectively, calculated from the indicated FE peaks. Uncertainties are quoted with k = 2.

The experimental and simulated spectra corresponding to the measurement with HPGe detector are shown in Fig. 2.31. $^{138}$La and $^{40}$K spectra were simulated scaling both simulations from PENELOPE/penEasy with the calculated activities, 19.7 Bq and 32.6 Bq, respectively. Thus, as can be seen in Fig. 2.31, both results were added and the measured spectrum was successfully reproduced, with a proper overlap in the peaks. The figure reveals that the contribution of $^{138}$La to the spectrum is significantly larger than that of $^{40}$K. Therefore, the contribution from $^{40}$K can be neglected.

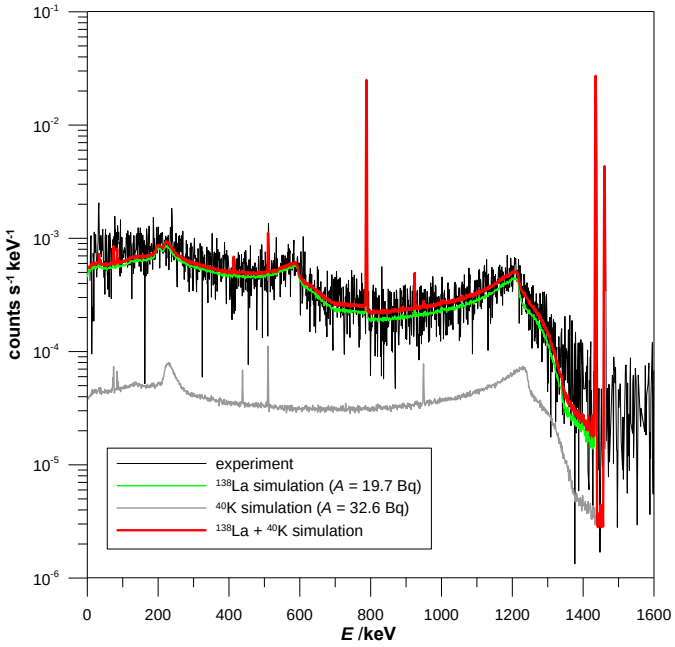


**Fig. 2.31.** Experimental and calculated background spectra of the 1"×1" $LaBr_3$(Ce) detector registered by HPGe. The experimental spectrum (black curve) was registered during 59473 s. The spectra calculated assuming 19.7 Bq of $^{138}$La and 32.6 Bq of $^{40}$K are plotted as coloured curves.

### Lanthanum-138 internal background simulation

The estimated $^{138}$La impurity content is now used to determine the $LaBr_3$(Ce) internal background spectrum by MC simulation. In Fig. 2.32, the simulated spectrum for a $^{138}$La activity of 19.7 Bq in a 1" x 1" crystal is compared with the experimental background spectrum acquired during 10200 s in the UDO II laboratory. As already explained, the wide peak located around 1470 keV is made up

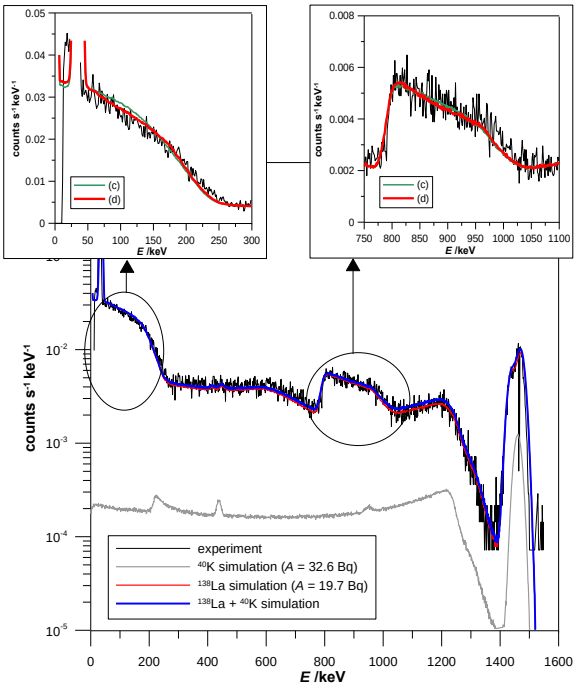


**Fig. 2.32.** Self-counting spectrum produced by the $^{138}$La contamination in a 1" x 1" $LaBr_3$(Ce) crystal. The calculated spectrum (red curve) pertaining to 19.7 Bq of $^{138}$La plus 32.6 Bq of $^{40}$K is compared with the experimental spectrum registered at UDO II during 10200 s (black curve). The insets expand the β continua of the spectrum to better visualize the small difference between the simulations done with the experimental Fermi spectra evaluated by Quarati et al., 2012 using (c) a coincidence method and (d) numerical deconvolution.

of three peaks, namely the 1441 keV and 1473 keV sum peaks from the decay of $^{138}$La, as well as the 1460.8 keV peak from the decay of $^{40}$K;the latter is masked by $^{138}$La sum peaks. The experimental spectrum is successfully reproduced by the PENELOPE/penEasy simulation.

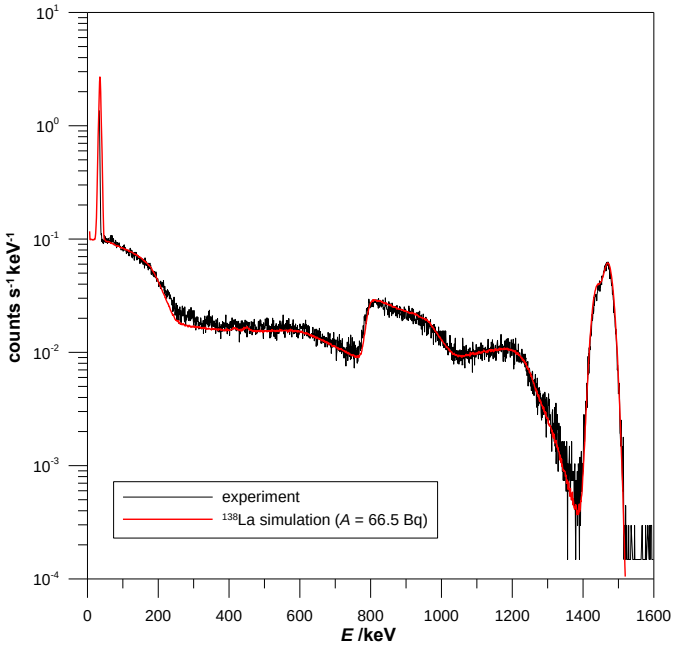


**Fig. 2.33.** Self-counting spectrum produced by the $^{138}$La contamination in a 1.5"×1.5" $LaBr_3$(Ce) crystal. The black curve is the experimental spectrum registered at the UDO facility during 8887 s. The red curve is the calculated spectrum corresponding to 66.5 Bq of $^{138}$La.

The activity of $^{138}$La per unit volume is similar for all detectors because it is determined by the natural abundance of this radionuclide. To check the proposed methodology and considering an activity per unit volume equal to 1.53 Bq cm$^{-3}$, the internal background for a 1.5" x 1.5" crystal investigated too. The probe employed in this self-counting measurement was also a model of

Saint Gobain, and the geometry was implemented in PENELOPE according to the manufacturer drawings In Fig. 2.33 the simulated spectrum scaled with a $^{138}$La activity of 66.5 Bq is compared with the experimental spectrum registered at UDO during 8887 s. Again, good agreement between the experimental and simulated spectra is achieved and the contribution of $^{40}$K was deemed negligible.

Table 2.7 lists the measured count rates for the ~1470 keV peak and for both detectors along with the simulated values. The calculated count rates from the PENELOPE/penEasy program were obtained according to the activities calculated for each crystal. The peak areas and their uncertainties were estimated according to the simple peak integration defined in Gilmore, 2008. It can be observed that the relative differences are smaller than 10%.

| Crystal size | Calc. A /Bq | MC /$s^{-1}$ | Exp /$s^{-1}$ |
|---|---|---|---|
| **1"×1"** | 19.7(9) | 0.480(24) | 0.456(14) |
| **1.5"×1.5"** | 66.5(30) | 3.14(16) | 2.90(4) |

**Table 2.7.** Areas of the ~1470 keV sum peak from $^{138}$La obtained by PENELOPE/penEasy simulation compared with the measurement at UDO and UDO II. Uncertainties are quoted with k = 2.

## 2.6 Effects of cosmic radiation

Cosmic radiation consists of high-energy particles coming from outside the Earth's atmosphere. Most particles interact in the upper atmosphere and produce secondary radiation, mainly pions, which in turn, interact at surface level and produce mainly, muons.

Muons decay into high-energy electrons and positrons, resulting in Compton events, backscatter and bremsstrahlung interactions when

they interact with spectroscopy crystals in the energy range up to 2000 keV. These effects produce differences shown at low energies in Fig. 2.25 and Fig. 2.28. Nevertheless, the number of counts detected is too low and remains hidden when terrestrial radiation is measured.

The contribution of cosmic radiation to the dose rate could be expressed by Equation (2.25) (Cortès, 2001). This equation takes into account pressure variations, since the thickness of the atmosphere affects the number of cosmic rays that reach the terrestrial surface.

$$\dot{D}_c(p) \approx \dot{D}_c(p_0) - a_c \cdot (p - p_0) \tag{2.25}$$

where $\dot{D}_c(p_0)$ is a constant value (30.094 nGy), $p_0$ is the reference pressure 1013 hPa, $p$ is the pressure at measurement time and $a_c$ is a constant experimentally adjusted (0.142 ± 0.004 nGy hPa$^{-1}$ for a proportional counter model FHZ601A and 0.096 ± 0.002 nGy hPa$^{-1}$ for a Reuter-Stokes chamber).

## 2.7 Internal background subtraction

To subtract measured or simulated internal background from the measured spectrum, energy calibration of the spectra should be properly corrected (see section 2.4), which implies that the first step must be the energy calibration.

Typical acquisition times in environmental monitoring are only several hundreds of seconds, which in some regions means a low number of counts with high uncertainties, i.e., according to Poisson statistics $u(C) = \sqrt{C}$, with $C$ the number of counts in a single channel (Knoll, 2010). Therefore, the process of internal background subtraction requires the use of counting decision limits. In each

channel, internal background subtraction is described by Equation (2.26).

$$NC = C - B \tag{2.26}$$

where $NC$ are the net counts, $C$ are counts from the row measurement and $B$ are counts from the internal background.

When $C \sim B$, the critical limit ($L_C$) gives the limit above which we can be confident in saying that a net count is significant (see Appendix 1). If the number of counts is reasonably high the Poisson distribution can be approximated to the Normal distribution. If we consider a confidence interval of 95%, the $k_\alpha$ factor would be 1.645 (we use one-tailed tables because of the $L_C$ definition) and the $L_C$ is defined by Equation (2.27).

$$L_C = 2.33\sqrt{B} \tag{2.27}$$

Counts above the critical ($L_c \leq NC$) limit are accepted, whereas those below the critical limit ($NC < L_C$) are not statistically significant. In the latter case, before rejecting the counts, we draw on the upper limit ($L_U$) (see Appendix 1). Counts are sorted in a Normal distribution between $L_U$ and $L_U$ according to Equation (2.28), where $\xi$ is a random number which follows a Gaussian distribution (see Appendix 2), with mean $NC$ and standard deviation $L_U$.

$$NC = L_U \cdot \xi \tag{2.28}$$

If $|NC| < |L_U|$ after this sort, the counts are sorted again. If counts are $NC$ values below 0, they are disregarded, while those above 0 are accepted.

In the case of a low number of counts ($C < 25$), the approximation to a Normal distribution is not valid and the Poisson distribution itself is used. For a particular degree of confidence defined by α, the $L_C$ is defined as the minimum value of $n$ for which the condition described by Equation (2.29) is satisfied (Gilmore, 2008).

$$\sum_{i=n}^{\infty} \frac{[B]^n}{n!} e^{-B} \leq \alpha \tag{2.29}$$

Any count below the critical limit would have to be interpreted as a non-detected count. Counts above this limit are accepted.

The methodology of internal background subtraction is applied to a natural spectrum registered with Monitor 1 in Fig. 2.34. Differences are clearly observed in the $^{227}$Ac and $^{138}$La peak regions.

The effects of statistical corrections detailed above are illustrated in Fig. 2.35. Details of the high energy region for two spectra measurements with 1-hour difference are shown. Spectrum acquisition time was $t = 900$ s on the left, while, on the right, the acquisition time was $t = 3600$ s. This energy region is representative of uncertainties in background subtraction because of the low number of counts. The counts are mainly produced by $^{227}$Ac contamination (see section 2.5) and the natural radioisotope $^{208}$Tl ($E = 2614.5$ keV).

On both plots, black bars show the experimental spectrum, green bars show the time-normalized internal background measured in the lead castle at the UDO II (section 2.5.2), the red dashed line shows the critical limit calculated according to Equation (2.27) and blue bars show the net spectrum after internal background subtraction. Due to the total number of counts, the Poisson distribution prevails in the

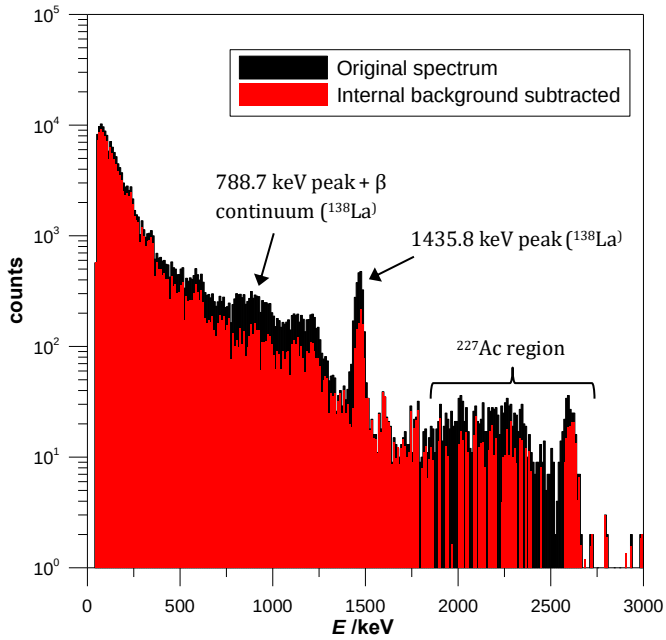


**Fig. 2.34.** Internal background subtraction for a natural background registered with 1" x 1" $LaBr_3(Ce)$ monitor (acquisition time $t$ = 3600 s).

900 s spectrum, whereas in the 3600 s spectrum the approximation to a Normal distribution is possible in most channels. As can be observed, more counts *survive* when the approximation to a Normal distribution is valid. In addition, the Compton edge of $^{208}Tl$ is marked with a green line in Fig. 2.35. In the multiple Compton area of this peak almost all counts are due to $^{227}Ac$ contamination.

An example of the relevance of uncertainties is seen in Fig. 2.36. The experimental spectrum (black points) is compared with the internal background (red points) for acquisition times $t$ = 900 s (left side) and $t$ = 3600 s (right side); uncertainties are the square root of the number of counts. In the short-time spectrum, counts and uncertainties from the experimental spectrum are almost fully overlapped by the internal background, which means $NC \sim 0$, and

statistical corrections lead to several zero values because the bulk of the counts should be analyzed as a Poisson distribution ($C < 25$). In contrast, with long acquisition times such as, $t = 3600$ s, statistical corrections are not as relevant since uncertainties are reduced.

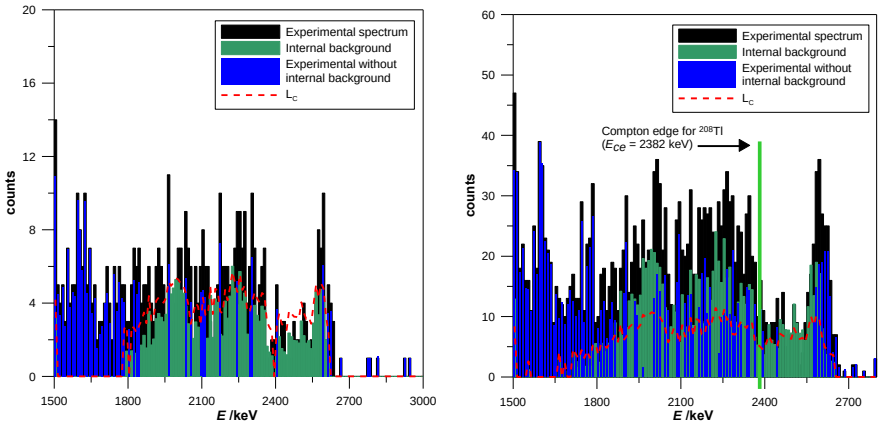


**Fig. 2.35.** Statistical effects on internal background subtraction for a natural gamma spectrum with $t = 900$ s (left side) and $t = 3600$ s (right side). Blue bars are a bit narrow for a better visualization.

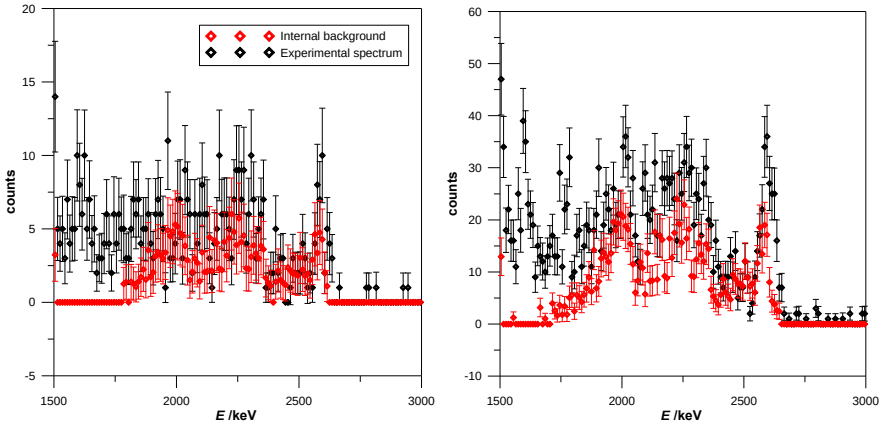


**Fig. 2.36.** Comparison of uncertainties associated to internal background and experimental spectrum for $t = 900$ s (left) and $t = 3600$ s (right).

# 3 Ambient dose equivalent rate from $LaBr_3$(Ce) spectra

## 3.1 Introduction

Nowadays there are more radiological surveillance networks installing spectrometric devices in addition to dosimetric probes. These detectors provide nuclide-specific information, allowing the identification and activity determination of radionuclides. In addition, some of them also provide ambient dose equivalent rate values ($\dot{H}^*(10)$) calculated from measured spectra.

In the following chapter two different methodologies to obtain $\dot{H}^*(10)$ from gamma-ray spectrum are compared. The first one, known as *stripping method*, subtracts out all partial absorptions in the measured spectrum in order to calculate the $\dot{H}^*(10)$ value from the outcoming flux. The second one, *conversion coefficients method*, divides measured spectrum into energy regions and applies energy-dependent conversion coefficients to obtain $\dot{H}^*(10)$.

Both methodologies make use of PENELOPE/penEasy (Sempau et al., 2011) Monte Carlo (MC) code to study detectors response.

### 3.1.1 Characterization of $LaBr_3$(Ce) detectors

First step to apply MC simulations is the definition of detector geometry and materials. In PENELOPE/penEasy PENGEOM subroutine permits working with geometries consisting of a number of homogeneous bodies limited by quadric surfaces with well-defined surfaces (detailed information is supplied in Salvat et al., 2011).

Materials in PENELOPE/penEasy were created using the program MATERIALS.EXE. The program use the own material database in PENELOPE ("pendbase") which contains several materials and elements or it also allows the definition of new materials. Thus, $LaBr_3$(Ce:5%) was created with the following chemical composition (mass %):

**La:** 34.85 %

**Br:** 60.15 %

**Ce:** 5 %

**Density:** 5.08 g $cm^{-3}$

As it has been already introduced in section 2.5.3, with materials and geometry well defined MC simulation provides the normalized probability distribution of deposited energy in each energy bin of specified detection material, according to bin width defined in the simulation. Thus, the simulated efficiency ($\varepsilon_{sim}$) in the photopeak is:

$$\varepsilon_{sim} = \frac{P_{FE}}{1\ history} \tag{3.1}$$

Where $P_{FE}$ is the probability of detection a history, that is, simulated particle (gamma particle) in the photopeak. The simulated spectrum can be then convolved with a Gaussian function according to detector FWHM in order represent the real peak-shape detected by scintillator detectors, which have a certain width due to generation of light, conversion of light to electrical charge and the amplification of signal.

Originally coincidence summing effects of radioactive decay was not considered in PENELOPE/penEasy. In order to take into account, the penEasy subroutine that generates the initial state (position, energy, direction) was adapted to include the decay and cascade

emissions for several radionuclides, including $^{241}$Am, $^{137}$Cs and $^{60}$Co used in the following.

## Monitor 1:

Monitor 1 including both the detector 1" x 1" and its housing is described in Fig. 3.1 and Fig. 3.2. Fig. 3.1 shows a drawing of the $LaBr_3$(Ce) detector from Saint Gobain and pictures of aluminium housing used to protect the detector of the external environment. On Fig. 3.2 it is illustrated the simulation of complete monitor geometry obtained with PENELOPE/penEasy. Each colour represents a material according to Table 3.1. It may be considered that geometry viewers (GVIEW2D and GVIEW3D) consider all materials as solids, which means that we are not able to see through air, as in common drawings.

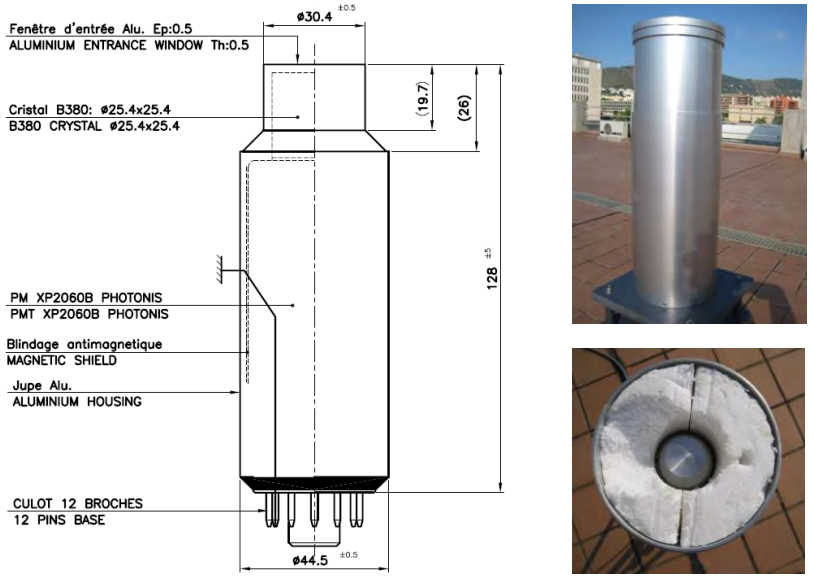


**Fig. 3.1.** Drawing of 1" x 1" $LaBr_3$(Ce) BrilLance380 model from Saint Gobain. On right side it is shown the aluminum housing (top) and a top view with detector inside housing (down).

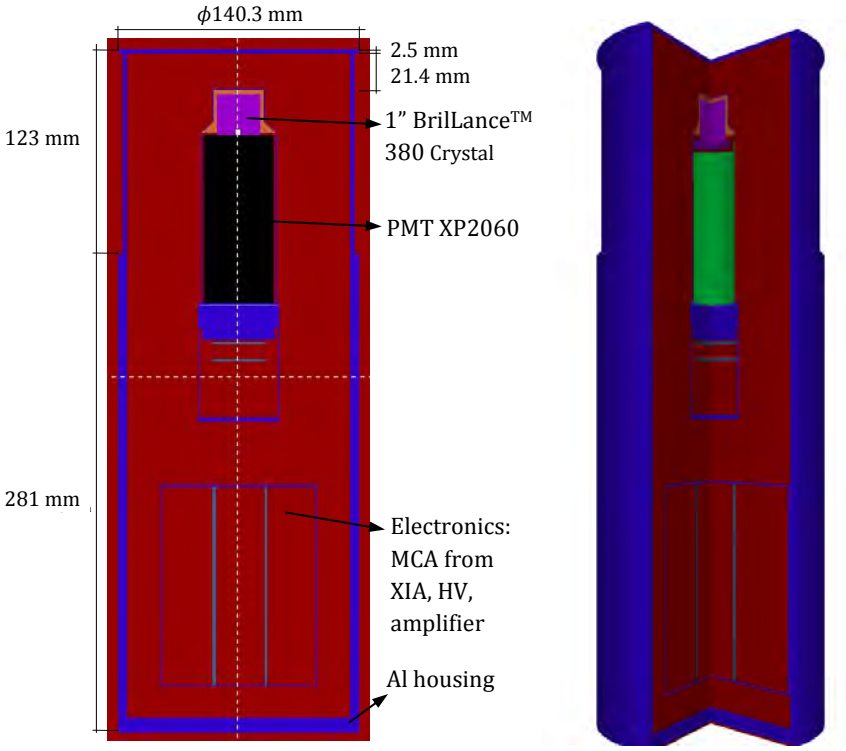


**Fig. 3.2.** Geometry of Monitor 1 defined with PENELOPE/penEasy. 2D view (left) is obtained with *GVIEW2D* and 3D view (right) with *GVIEW3D.*

| Colour | Material |
|---|---|
| | LaBr3(Ce) |
| | Teflon |
| | Aluminium |
| | Iron |
| | Air |
| | Silicon |
| | Bakelite |
| | Vacuum |

**Table 3.1**. List of materials used in the simulation.

Simulated geometry was evaluated through several exposures with certified point sources purchased from Amersham company, the same used in section 2.5.3. Fig. 3.3 shows the geometry of point sources, rectangular-shaped, and the simulated setup: point sources were located 50.6 mm above housing. Experimental and simulated efficiencies in the photopeaks obtained are listed in Table 3.2, which shows good agreement between experimental and simulated results. Furthermore, in Fig. 3.4 experimental and simulated spectra for three sources are plotted showing great match.

Monitor 2 geometry is not defined explicitly here, while it was also a 1" x 1" detector from Saint Gobain.

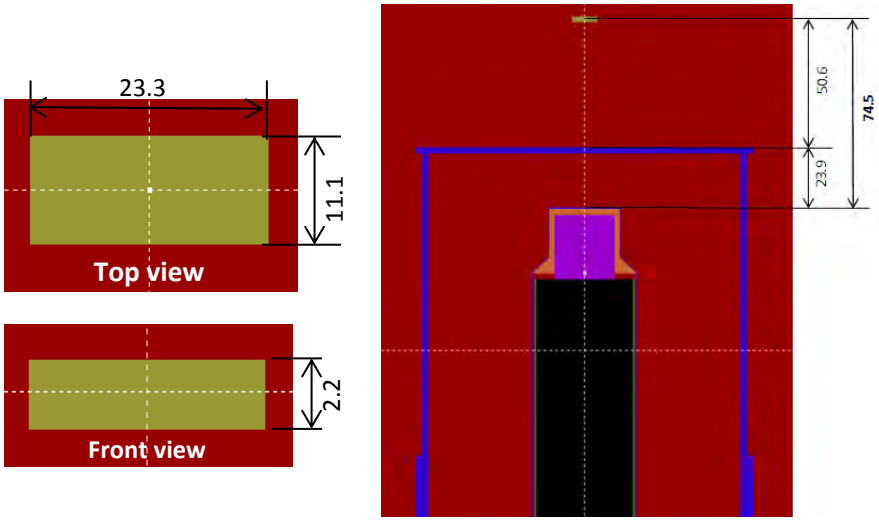


**Fig. 3.3.** Point sources geometry (left side) and geometry of the setup of the detector with point sources (right side). Views obtained with GVIEW2D.

| Radionuclide | E(keV) | $\varepsilon_{exp}$ (k=2) | $\varepsilon_{sim}$ (k=2) |
|---|---|---|---|
| $^{241}Am$ | 59.54 | $(4.4 \pm 0.4) \cdot 10^{-3}$ | $(4.57 \pm 0.02) \cdot 10^{-3}$ |
| $^{137}Cs$ | 661.6 | $(9.2 \pm 0.8) \cdot 10^{-4}$ | $(9.24 \pm 0.06) \cdot 10^{-4}$ |
| $^{60}Co$ | 1173.23 | $(4.4 \pm 0.6) \cdot 10^{-4}$ | $(4.46 \pm 0.06) \cdot 10^{-4}$ |
| $^{60}Co$ | 1332.49 | $(3.9 \pm 0.4) \cdot 10^{-4}$ | $(3.96 \pm 0.04) \cdot 10^{-4}$ |

**Table 3.2**. Experimental and simulated FE peak efficiencies of the Monitor 1 for point radioactive sources.

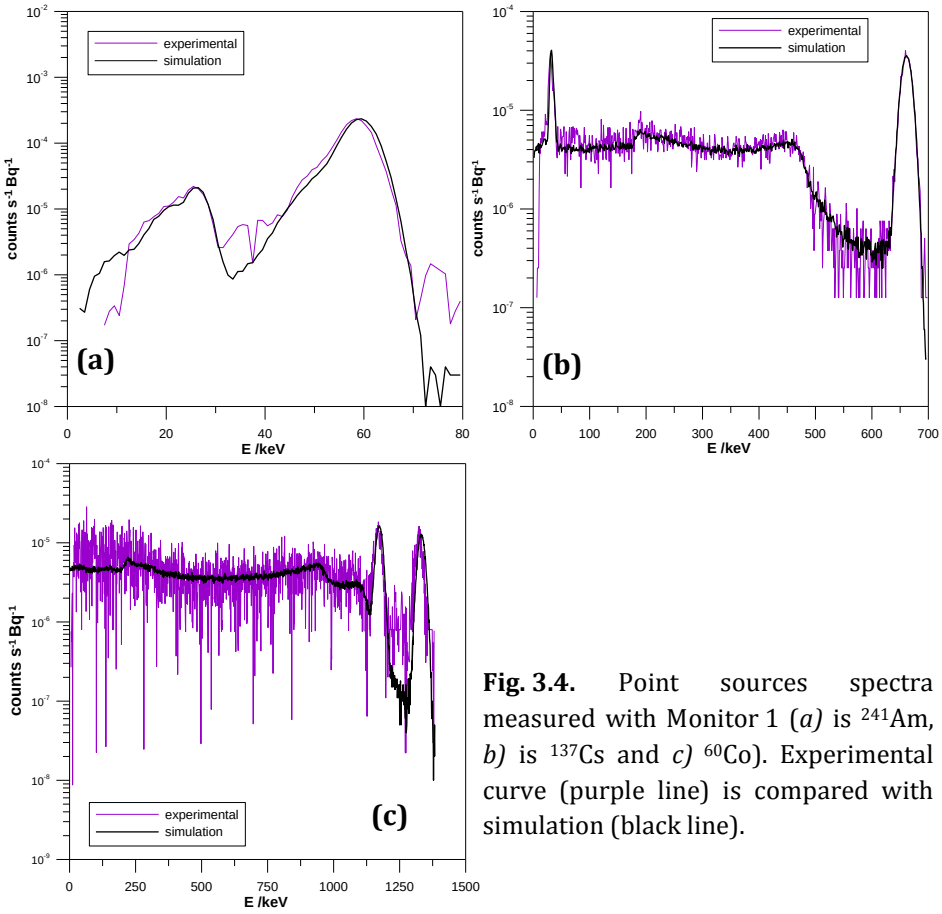


**Fig. 3.4.** Point sources spectra measured with Monitor 1 (*a)* is $^{241}Am$, *b)* is $^{137}Cs$ and *c)* $^{60}Co$). Experimental curve (purple line) is compared with simulation (black line).

**SpectroTRACER**:

SpectroTRACER including both the detector 1.5" x 1.5" and its housing is described in Fig. 3.5. It shows the simulation of complete monitor geometry obtained with PENELOPE/penEasy, it includes the detector and its electronics together with two Geiger-Müllers. This commercial model is equipped with them in order to cover high values of dose rates. Just as for Monitor 1, each colour represents a material according to Table 3.3. It may be considered that geometry viewers (GVIEW2D and GVIEW3D) consider all materials as solids, which means that we are not able to see through air.

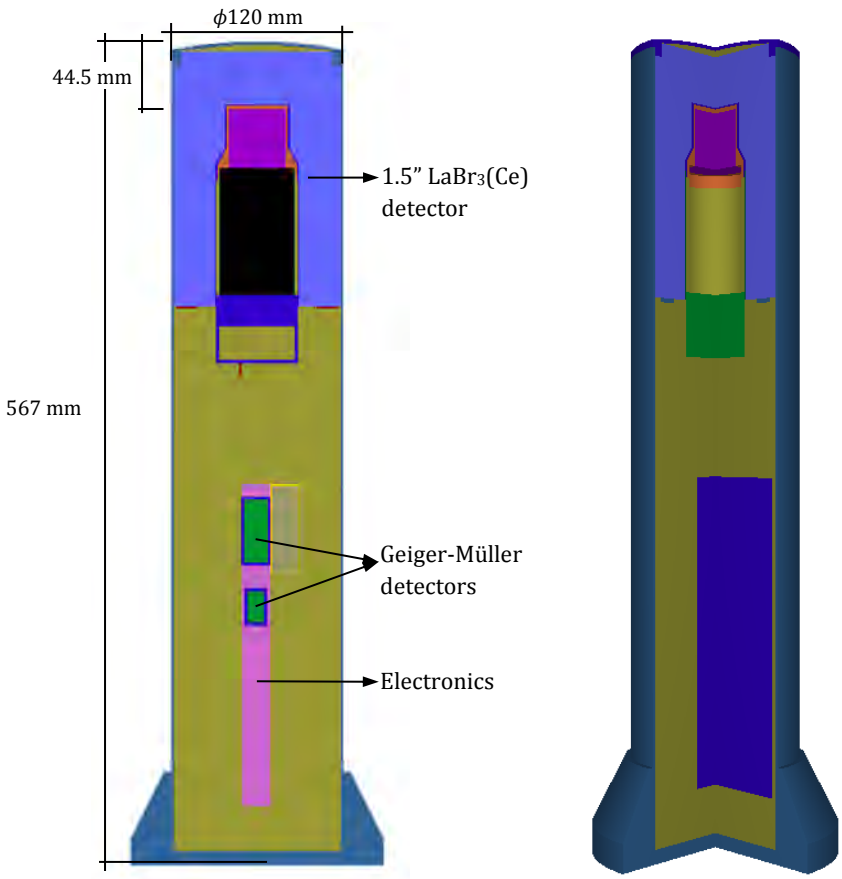


**Fig. 3.5.** Geometry of SpectroTRACER defined with PENELOPE/penEasy. 2D view (left) is obtained with *GVIEW2D* and 3D view (right) with *GVIEW3D.*

| Colour | Material |
|---|---|
| | $LaBr_3$ |
| | Teflon |
| | Aluminium |
| | Vacuum |
| | Iron |
| | Steel |
| | PVC |
| | Rubber (PLX 28) |
| | AlMgSi0.5 |
| | Air |
| | Plastic (ABS) |
| | Silica |
| | Gas(Ne) |

**Table 3.3.** List of materials used in the simulation.

Geometry of SpectroTRACER was checked in the context of MetroERM project through irradiations in the LCD with $^{241}$Am, $^{137}$Cs and $^{60}$Co sources. Simulation of such scenario would take huge amount of computational time since the source is located several meters away from the detector and inside the collimator, which means that in each history particle interacts thousand times before reaching the detector. For this reason, the *Detection Forcing* variance reduction technique was used. This method, which is explained in detail in MetroERM deliverable D.1.3.5, considers in each interaction the probability of the particle to reach the detector. Results obtained are shown in Fig. 3.6, simulated spectra were added to measured background in the lab and a good agreement with experimental spectra was achieved in the photopeak region. However, for higher values, it can be observed an underestimation in simulated spectra because simulations do not account for pile-up effect. In the Compton area, at energies lower than photopeak, there is also an

underestimation of simulations. The reason of this underestimation is due to the contribution of the scatterings produced by neighboring sources to the photon flux produced by the source used in the irradiation. Radioactive sources in the irradiator are located in a roulette and the geometry and materials cannot shield completely the photons coming from neighboring sources. Remarkable is for $^{60}Co$ source, since its activity was 0.407 GBq and scatterings were produced by a neighboring $^{137}Cs$ source with an activity of 507.5 GBq.

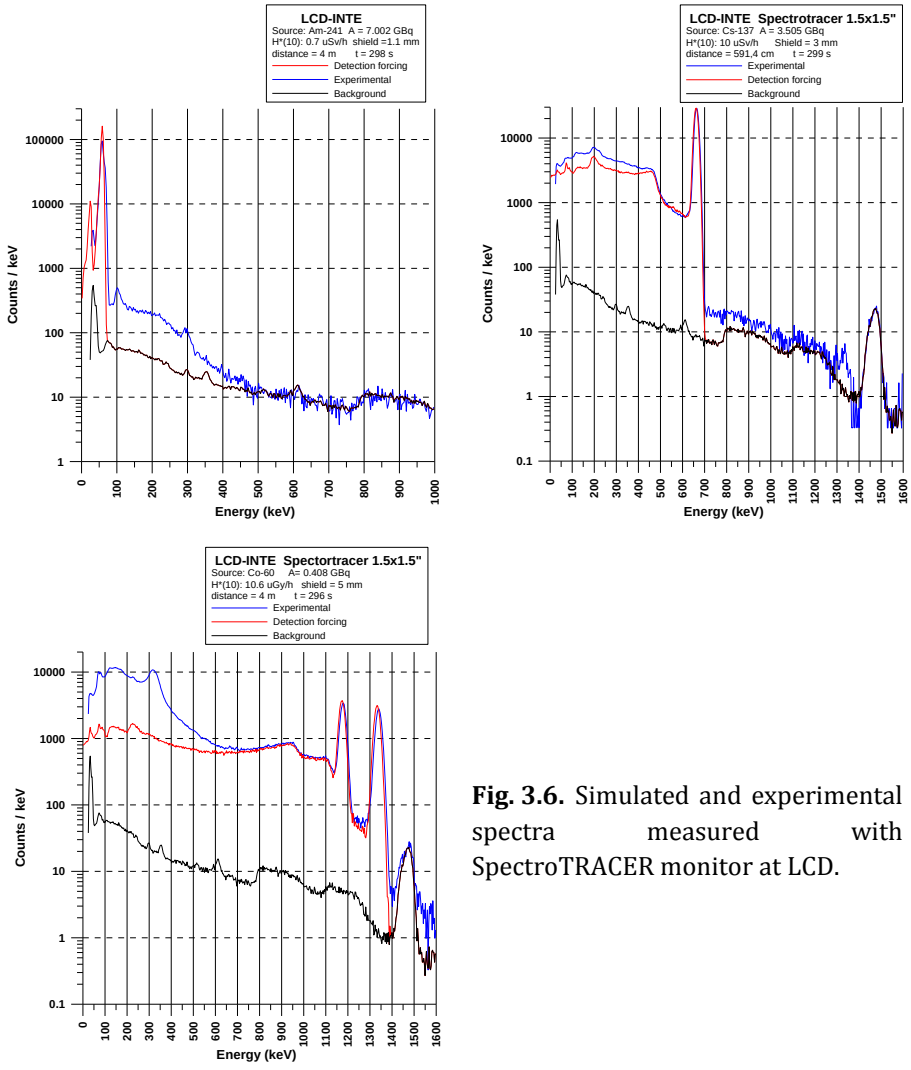


**Fig. 3.6.** Simulated and experimental spectra measured with SpectroTRACER monitor at LCD.

## 3.2 Stripping method

*This section in based on the publication (Camp and Vargas, 2014) and submitted paper (Vargas et al., 2017).*

The stripping method is based on the fact that, according to general definition of absorbed dose, the energy deposited by any source in a certain point can be calculated provided that we know the energy flux. Unfortunately, measured spectra with spectrometric systems do not provide directly this value, depending on the interaction of gamma radiation with matter sometimes only partially its energy will be deposited in the detector, due to Compton scattering or pair production with escape peaks. The stripping method consists on subtracting all partial absorptions from the experimental spectrum in order to have only full absorptions. Once the spectrum has been stripped, the full peak energy efficiency is used to estimate the external ambient flux and, subsequently, the absorbed dose. Thus, this method only requires knowledge of detector geometry which directly influences in partial absorptions, while external parameters are not needed.

The stripping method was commonly applied to germanium detectors (Miller, 1984; Clouvas et al., 1998), because high resolution spectrum can also provides individual full-energy (FE) peak count rates which aid in the calculation of air kerma rate. Nevertheless, their cost and cooling requirements do not make it advisable for continuum monitoring environmental radioactivity. A choice of some countries such as Finland are $LaBr_3$(Ce) detectors. These crystals have a resolution about 3 % at 662 keV, good enough to properly estimate air kerma rate applying the stripping method.

In this dissertation the stripping method has been set up and validated with experimental spectra from $LaBr_3$(Ce) measured at the Calibration and Dosimetry Laboratory (LCD) of the INTE-UPC (http://inte.upc.edu/laboratoris-en/calibration-and-dosimetry-laboratory), where reference irradiations are produced. In addition, the method has been applied to gamma spectra acquired on the roof of the INTE premises at Campus Sud (Barcelona), where an $LaBr_3$(Ce) operates in parallel with the RS04/WEB_R monitor. Fig. 3.7 shows the geographic location of this measurement site.


**Fig. 3.7.** Location of the INTE-UPC facilities near to Mediterranian coast.

The facility is located 41.383N 2.116E, 70 m a.s.l., and the measuring site is on the roof of the building 10 m a.g.l. As it is shown in Fig. 3.7 the city is placed in a coastal depression between two mountain ranges, parallel to the coast and linked to the pre-coastal range through the valleys of two rivers (Llobregat and Besos). Hence, the station is characterized by strong and frequent winds coming from the NW which, according to (Barros et al., 2003), are channelled into: i) the valley of the Llobregat river which is perpendicular to the

coastline and flows between the Collserola hill (200-400 m a.s.l.); and ii) the valley of Besos river, in the south part of the Litoral range (200-400 m a.s.l.).

### 3.2.1 Methodology

Partial absorptions produced in the detector are directly related with detector geometry, because both the monitor housing and the crystal shape and size have a noticeable influence on the way how radiation energy is deposited. To apply the stripping method in a simple and precise way, the detector response should be isotropic since the angular ambient flux is not known. Both for 1" x 1" and 1.5" x 1.5" $LaBr_3$(Ce) crystals this has been already demonstrate.

The first step is to characterize the response of the detector for each FE peak absorbed. This response could be obtained experimentally using different radionuclide sources to obtain detector response in a broad energy range (0-3000 keV). Nevertheless, the use of sources could produce unwanted scatterings outside the detector and sum-peaks effects associated to cascade decays. These effects should be taken into consideration and should be corrected. In return, using MC simulations all energies are available without limitation of sources availability and we can ensure no interferences from other energies. Therefore, in this study detector response has been obtained by MC simulation using PENELOPE/penEasy code (Sempau et al., 2011).

Once the detector response is known, the stripping methodology can be applied to the experimental spectrum and, from the obtained fluence, the $\dot{H}^*(10)$ can be calculated.

### 3.2.1.1 Detector response

The method to calculate the partial absorptions produced in the detector for different energy fluxes is described in the following steps.

1) Simulations of monoenergetic parallel beams are performed in steps of 10 keV in an energy range from 0 to 3000 keV, i.e. 300 simulations, with an energy bin width of 0.5 keV. The source is

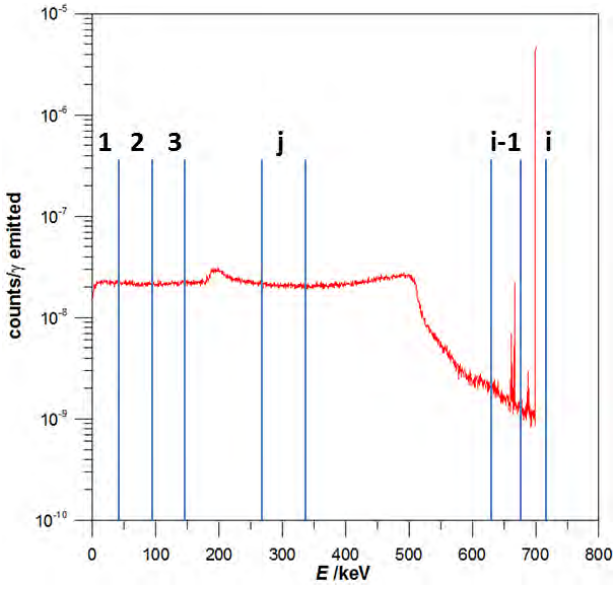


**Fig. 3.8.** Simulated spectrum of a 700 keV plane source.

located in front of the detector window with a radius large enough to cover the entire detector including the aluminium housing (see Fig. 3.9). The position does not matter because the detector shows an isotropic response (see chapter 2.3.2). An example for 700 keV is shown in Fig. 3.8.

2) Detected counts in a bin $i$ ($C_{j,i}$) produced by a monoenergetic beam of energy $j$ are normalized with detected counts in the FE peak ($C_{j,j}$):

$$c_{j,1} = \frac{C_{j,1}}{C_{j,j}}, \quad c_{j,2} = \frac{C_{j,2}}{C_{j,j}}, \quad \dots, \quad c_{j,j-1} = \frac{C_{j,j-1}}{C_{j,j}}, \quad c_{j,j} = \frac{C_{j,j}}{C_{j,j}} = 1 \tag{3.2}$$

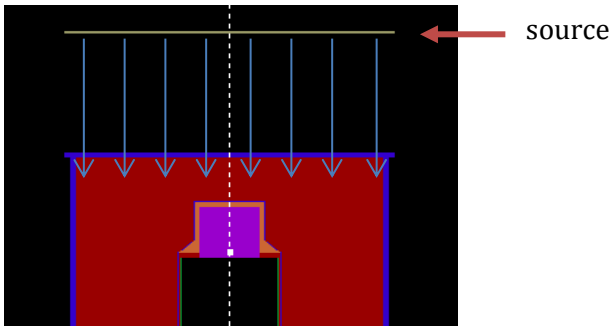


**Fig. 3.9.** Detail of the geometry of the $LaBr_3$(Ce) monitor with a monoenergetic parallel flux. Image obtained using GVIEW 2D.

### 3.2.1.2 Dose rate calculation with the stripping method

The procedure to obtain the stripped spectra and, subsequently, to estimate the true flux and the dose rate is described as follows.

1) Internal background must be subtracted from the experimental spectrum, because these counts do not proceed from an external flux, but from the crystal itself. Here, self-counting measurement at the Banyoles lake (see chapter 2.5) has been chosen, in order to remove both the internal background and counts due to cosmic radiation.

2) The energy bins of the acquired experimental spectrum are added in 10 keV energy bin, so that experimental and simulated spectra have the same bin width.

3) Equation (3.3) is applied (Miller, 1984) iteratively to strip the experimental spectrum. The stripping method starts in the highest energy bin and ends in the lowest one.

$$n'_i = n_i^{exp} - \sum_{j=i+1}^{k} n'_j \cdot c_{j,i} \tag{3.3}$$

where $n'_i$ are the counts in an energy bin due to full-energy absorptions, $n_i^{exp}$ are experimental counts measured in this energy bin, including full and partial absorptions, $n'_j$ are the previous stripped counts in the energy bins with higher energy than bin $i$ ($j$ values ranges from i+1 to $k$, where $k$ is the energy bin with the highest energy gamma line) and $c_{j,i}$ are partial absorptions defined in Equation (3.2).

Scheme 3.1 represents what is expressed by Equation (3.3). Experimental spectrum $N_0^{exp}$ is stripped from partial absorptions in iterative steps according to simulated spectra. It can be observed that $c_{n,n}$ values, that is, the detector response in the FE peak, are treated as 0 values, since only partial absorptions must be subtracted. It should be pointed out that negative counts resulting in the subtraction process are treated as zeros in the iterative steps, otherwise counts will be added, instead of subtracted, to the lower energy bands.

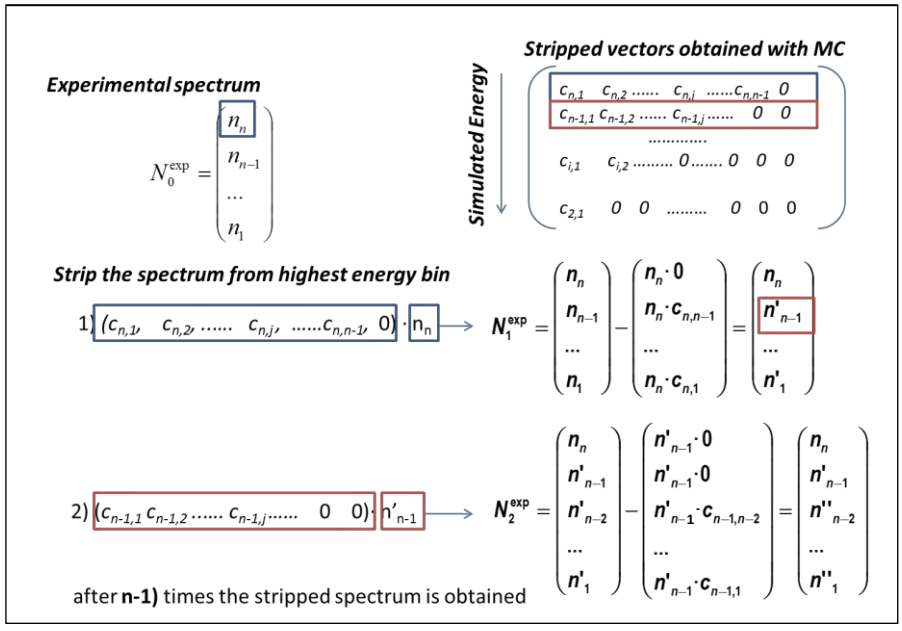


**Scheme 3.1.** Scheme of the iterative steps applied in the stripping method.

After this iterative procedure only full-absorptions remain in the spectrum, an example is shown in Fig. 3.10 for a $^{137}Cs$ point source. It can be observed that the FE peaks (661.6 keV and x-rays) does not suffer any variations, but the Compton region, corresponding to partial-absorptions, is substantially reduced. Remaining counts in the Compton area are due to full-absorptions of less energetic particles produced by scatterings in air, as well as, to the uncertainty associated to the measurement.

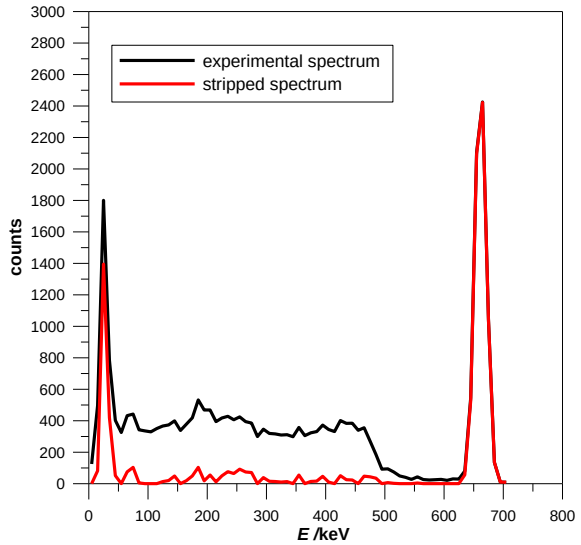


**Fig. 3.10.** Example of $^{137}Cs$ spectrum before and after stripping operation (energy bin width of 10 keV).

4) The incident fluence rate for every energy bin $i$ can be calculated from the counts calculated in the stripped spectrum using the following equation:

$$\phi_i[h^{-1}\,cm^{-2}] = \frac{n'_i}{\varepsilon_i \cdot t} \tag{3.4}$$

where $t$ is the spectrum measuring time in hours and $\varepsilon_i$ is the FE peak per incident fluence rate of energy $i$, which are calculated using Equation (3.5).

$$\varepsilon_i(cm^2) = p_i \left(\frac{1}{eV}\right) \Delta E_i\ (eV)\ S\ (cm^2) \tag{3.5}$$

where $p_i$ is the detection probability at bin $i$ per incident gamma of energy bin $i$ obtained from MC simulations, $\Delta E_i$ is the bin width in eV and $S$ is the surface of the incident fluence rate in the Monte Carlo simulation in $cm^2$.

5) Finally the $\dot{H}^*(10)$ ($\mu Sv\ h^{-1}$) is calculated from the incident fluence rate with Equation (3.6).

$$H^*(10)[\mu Sv\ h^{-1}] = 1.6 \times 10^{-10} \sum_{i=1}^{n} F_i \cdot \phi_i \cdot E_i \cdot \mu_i^{air} \tag{3.6}$$

where $Fi$ is the conversion factor from air-kerma into ambient dose equivalent (ISO 4037-3, 1999), $E_i$ is the energy of the particular energy bin (eV) and $\mu_i^{air}$ air is the mass absorption coefficient for air ($cm^2\ g^{-1}$) obtained from NIST Standard Reference Database (Hubbell and Seltzer, 1995).

### 3.2.1.3 Uncertainties in the stripping estimation

In this methodology there are two main sources of uncertainties, the first one associated to the number of counts ($n$). From Poisson statistics it can be expressed as $\sqrt{n}$. Applying this uncertainty to Equation (3.3) the law of propagation of errors yields to Equation (3.7).

$$u(n'_i) = \sqrt{n_i^{exp} + \sum_{j=i+1}^{k} n'_j \cdot (c_{j,i})^2} \tag{3.7}$$

Where $c_{j,i}$ uncertainties are disregarded because they are obtained from large scale MC simulations.

The total value of $\dot{H}^*(10)$ is calculated adding the $\dot{H}^*(10)_i$ contribution of each bin (see Equation (3.6)). As a consequence the other source of uncertainties is the inherent one associated to the band width. The uncertainty of the calculated ambient dose equivalent rate is (JCGM/WG1, 2008):

$$\begin{aligned} u(\dot{H}^*(10))[\mu Sv\ h^{-1}] = \\ = \frac{1.6 \times 10^{-10}}{t} \Bigg[ \sum_{i=1}^{n} \Bigg[ \left( \frac{\Delta F_i}{2\sqrt{3}} \cdot \frac{n'_i}{\varepsilon_i} \cdot E_i \cdot \mu_i^{air} \right)^2 \\ + \left( F_i \cdot \frac{u(n'_i)}{\varepsilon_i} \cdot E_i \cdot \mu_i^{air} \right)^2 + \left( F_i \cdot \frac{n'_i}{\varepsilon_i^2} \cdot E_i \cdot \mu_i^{air} \cdot \frac{\Delta \varepsilon_i}{2\sqrt{3}} \right)^2 \\ + \left( F_i \cdot \frac{n'_i}{\varepsilon_i} \cdot E_i \cdot \frac{\Delta \mu_i^{air}}{2\sqrt{3}} \right)^2 + \left( F_i \cdot \frac{n'_i}{\varepsilon_i} \cdot \frac{\Delta E_i}{2\sqrt{3}} \cdot \mu_i^{air} \right)^2 \Bigg] \Bigg]^{0.5} \end{aligned} \tag{3.8}$$

where $\Delta E_i$, $\Delta F_i$, $\Delta \varepsilon_i$ and $\Delta \mu_i^{air}$ means, respectively, the variation of $E_i$, $F_i$, $\varepsilon_i$ and $\mu_i^{air}$ between the upper and lower limit of each energy bin and follow the rules of type B uncertainties.

## 3.2.2 Validation of the methodology

### 3.2.2.1 Effects of the energy bin width

Each simulated spectra means the detector response for a certain energy fluence. The energy bins of the experimental spectrum should match with bins in the simulated spectra and with simulated energies. Following, two methodologies are explained and compared.

The experimental spectrum used to validate the methodology was obtained from a measurement of a $^{137}Cs$ point source with certified activity of 39.6 ± 1.6 kBq, purchased from Amersham Company. At the time of the measurement the activity was 26.4 ± 1.3 kBq and the source was located at a distance of 8.77 ± 0.01 cm from the crystal middle point.

The dose rate produced by a $^{137}Cs$ point source at this distance is 0.262 μGy $h^{-1}$, value obtained using the program Rad Pro Calculator (McGinnis, 2009). It should be noted that this program only considers photopeak contribution, but it is a good approximation since the measurement was done with a point source. Applying a conversion factor of 1.2 (ISO 4037-3, 1999), the ambient dose equivalent rate is 0.314 μSv $h^{-1}$.

**Stripping method using experimental energy bin width**

Incident gamma energies are simulated in steps of 10 keV. The experimental energy bin width is lower than 10 keV. In order to avoid calculating all the simulations, the response function is determined by interpolation between experimental spectrum and closest simulation using the position of Compton edge in both spectra.

The result of the stripped spectrum using the experimental bin width, which in this case was 0.514 keV, is displayed in Fig. 3.11. Table 3.4 shows a comparison between $\dot{H}^*(10)$ calculated from point source activity and distance (theoretical value) and $\dot{H}^*(10)$ calculated with the stripping method (calculated value), see Equation (3.6).

| Source | $\dot{H}^*(10)_{theoretical}$ /μSvh$^{-1}$ | $\dot{H}^*(10)_{calculated}$ /μSvh$^{-1}$ |
|---|---|---|
| $^{137}$Cs | 0.314 | 0.332 ± 0.008 |

**Table 3.4.** Ambient dose equivalent rate from a $^{137}$Cs point source. Theoretical value is obtained with Rad Pro Calculator (McGinnis, 2009) and calculated value applying the stripping method to measured spectrum. Uncertainty reported with $k$ = 2.

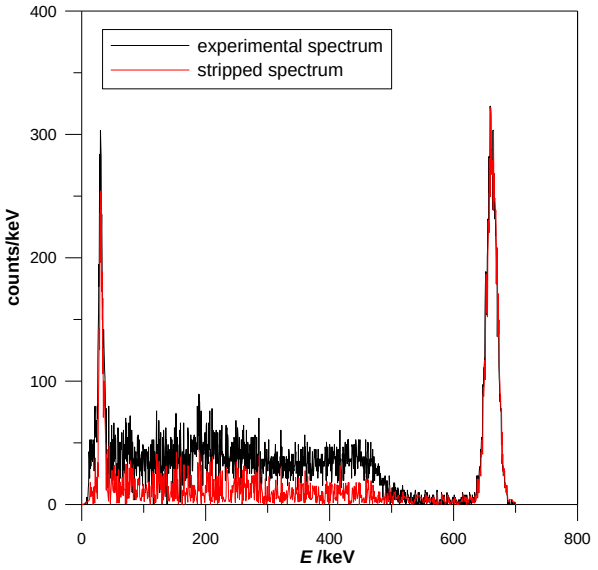


**Fig. 3.11.** Example of $^{137}$Cs spectrum before and after stripping operation (experimental energy bin width ~ 0.5 keV). Acquisition time 300 s.

### Stripping method using 10 keV and 50 keV energy bin width

Two possibilities are studied, incident gamma energies simulated in steps of 10 keV and in steps of 50 keV. Channels of experimental and simulated spectra are added to reach an energy bin width of 10 keV (50 keV), i.e. detector response is known for all incident gamma energies.

Fig. 3.12 shows a comparison of the stripping obtained with an energy band of 10 keV (left side) and 50 keV (right side). Calculated dose equivalent rates are shown in Table 3.5.

| Source | $\dot{H}^*(10)_{theoretical}$ /μSvh$^{-1}$ | $\dot{H}^*(10)_{calc.\Delta E=10keV}$ /μSvh$^{-1}$ | $\dot{H}^*(10)_{calc.\Delta E=50keV}$ /μSvh$^{-1}$ |
|---|---|---|---|
| $^{137}$Cs | 0.314 | $0.327 \pm 0.014$ | $0.35 \pm 0.05$ |

**Table 3.5.** Ambient dose equivalent rate from a $^{137}$Cs point source. Theoretical value is obtained with Rad Pro Calculator (McGinnis, 2009) and calculated value applying the stripping method to measured spectrum with energy bin width of 10 keV and 50 keV. Uncertainties reported with $k = 2$.

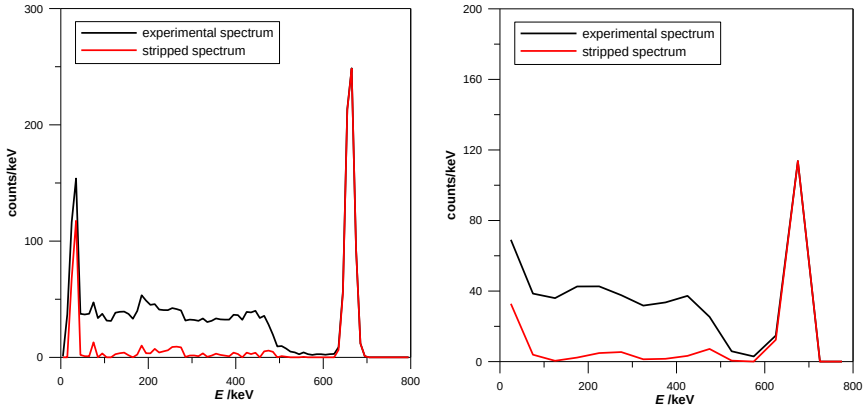


**Fig. 3.12.** Example of $^{137}$Cs spectrum before and after stripping operation using an energy bin width of 10 keV (left side) and 50 keV (right side). Acquisition time = 300 s.

In this dissertation the choice has been the use of energy bands of 10 keV.

### 3.2.2.2 Validation in the LCD

At the LCD laboratory is it possible to produce controlled irradiations. With the aim to check the stripping method, several irradiations of Monitor 1 (1" x 1" crystal) and SpectroTRACER (1.5" x 1.5" crystal) were carried out using $^{137}$Cs sources.

Estimated values of $\dot{H}^*(10)$ obtained applying the stripping method to measured spectra are shown in Table 3.7 and Table 3.6, together with $\dot{H}^*(10)$ reference values. All $\dot{H}^*(10)$ obtained with the stripping method were calculated with an energy bin width of 10 keV. Results show that differences are less than 10 % in both detectors, even though above 200 μSv the method starts to overestimate the results probably because of the higher contribution of the pile-up gammas.

Uncertainties of calculated values reported are obtained according to section 3.2.1.3.

| $\dot{H}^*(10)$ /μSvh$^{-1}$ | $\dot{H}^*(10)_{calculated}$ /μSvh$^{-1}$ | Relative difference (%) |
|---|---|---|
| 2.00 ± 0.12 | 1.92 ± 0.30 | -4 |
| 5.0 ± 0.4 | 4.8 ± 0.5 | -4 |
| 10.0 ± 0.6 | 9.4 ± 0.6 | -6 |
| 50.0 ± 2.9 | 47.5 ± 1.5 | -5 |
| 100 ± 5.9 | 100.6 ± 0.6 | 0.6 |

**Table 3.7.** $\dot{H}^*(10)$ calculated values from measured spectra with Monitor 1 in the LCD compared with nominal values (measurements with $t$ = 300 s). Uncertainties quoted with $k$ = 2.

| $\dot{H}^*(10)$ /μSvh$^{-1}$ | $\dot{H}^*(10)_{calculated}$ /μSvh$^{-1}$ | Relative difference (%) |
|---|---|---|
| 2.00 ± 0.12 | 2.08 ± 0.01 | 4 |
| 10.0 ± 0.6 | 10.44 ± 0.09 | 4.4 |
| 50.0 ± 2.9 | 52.6 ± 0.6 | 5.2 |
| 200 ± 12 | 220 ± 6 | 10 |
| 2000 ± 117 | 2484 ± 51 | 24.2 |

**Table 3.6.** $\dot{H}^*(10)$ calculated from measured spectra with SpectroTRACER in the LCD compared with nominal values (measurements with $t$ = 300 s). Uncertainties quoted with $k$ = 2.

## 3.3 Conversion coefficients methodology

This method is based on the definition of calibration coefficients to convert the energy deposited on the detector to air kerma rate. Given that the energy deposited can be obtained from detected counts, a relation is stablished between number of counts in measured spectra and the air kerma responsible of these counts. A description of this methodology can be found elsewhere (Grasty et al., 2001; Dombrowski, 2014) for different detector types.

The use of a unique conversion coefficient between energy deposited in the detector and kerma in air requires a constant ratio, i.e. a linear relationship between mass energy absorption coefficients in air and in the crystal. This can be true at high energies but at low energies the ratio ceases to be constant, as it is shown in Fig. 3.13. The reason is that photoelectric interactions prevail at low energies and

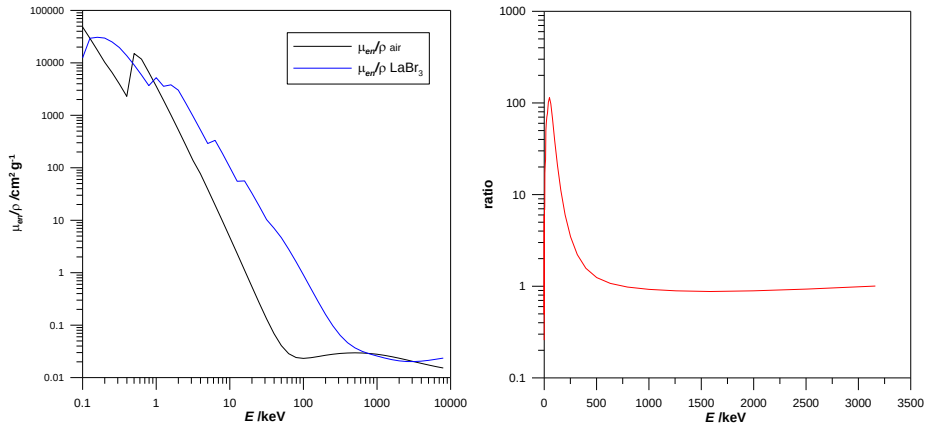


**Fig. 3.13.** *Left side.* Values of mass energy-absorption coefficient as a function of photon energy for $LaBr_3$(Ce) and dry air (values obtained from simulations with PENELOPE). *Right side.* Ratio of the mass energy-absorption coefficients between $LaBr_3$(Ce) and dry air.

they are coupled with characteristic absorption edges corresponding to binding energies at electron shells. These binding energies and in turn, discontinuities in the photoelectric absorption curve, depend on the atomic composition of the material.

To solve this problem the spectrum is divided in several energy regions and for each one, a calibrated conversion coefficient is used. So the total air kerma ($K$) results from the sum of $n$ partial values of kerma, each one calculated for an energy region.

$$K = \sum_{i=1}^{n} w_i n_i E_i \tag{3.9}$$

Where $w_i$ is the conversion coefficient of energy region $i$ in $eV^{-1}$, $n_i$ the number of counts of the region $i$ and $E_i$ the mean energy of the energy band $i$ in eV. The value $n_i E_i$ corresponds to the energy deposited in the region *i.*

Actually, as it has been explained in previous sections, the recommended magnitude to use in environmental monitoring is $\dot{H}^*(10)$. In ISO 4037-3, 1999 document the conversion coefficients that should be used to convert air kerma to ambient dose equivalent are shown. If the conversion coefficients ($w_i$) are obtained by Monte Carlo (MC) simulation, the energy deposited in the detector can be directly related with $\dot{H}^*(10)$ and then Equation (3.9) moves to:

$$\dot{H}^*(10) = \sum_{i=1}^{n} w_i n_i E_i \tag{3.10}$$

### 3.3.1 Methodology

The basis to obtain $\dot{H}^*(10)$ from measured spectrum with this methodology is to determine the conversion coefficients ($w_i$).

For each energy band a calibration measurement (experimental or simulated) is required, with known $H^*(10)$ and a gamma-ray emission of the same energy as the energy band. Thus, for $n$ energy bands, $n$ measurements should be performed and, following Equation (3.10), $n$ linear relationships can be defined between the ambient dose equivalent and the energy deposited in each energy region of the spectrum (Toivonen et al., 2008).

$$\begin{pmatrix} H^*(10)_1 \\ \vdots \\ H^*(10)_n \end{pmatrix} = \begin{pmatrix} n_{1,1}E_1 & \cdots & n_{1,n}E_n \\ \vdots & \ddots & \vdots \\ n_{n,1}E_1 & \cdots & n_{n,n}E_n \end{pmatrix} \begin{pmatrix} w_1 \\ \vdots \\ w_n \end{pmatrix} \tag{3.11}$$

Where $H^*(10)_i$ is the ambient dose equivalent of the measurement $i$, $n_{i,j}$ are number of counts for a measurement $i$ at the energy interval $j$, $E_j$ is the mean energy of the energy band $j$ and $w_j$ is the energy-dependent conversion coefficient to be determined.

From Equation (3.11) it is obtained a system of $n$ linear equations (corresponding to $n$ calibration measurements) of the form $\vec{A} \cdot \vec{x} = b$ (in particular, $(\overrightarrow{n \cdot E}) \cdot \vec{w} = H^*(10)$). To solve the system different matrix operations can be used, such as the Cholesky decomposition. The general solution obtained is:

$$w_i = \frac{H^*(10)_i - \sum_{j=1}^{i-1} n_{ij}E_j w_j}{n_{ii}E_i} \tag{3.12}$$

The number of energy regions in which the spectrum is divided and thereby, the number of conversion factors to be used is not fixed. If they are determined experimentally, the limitation is the availability of sources, since one measurement is required for each energy band. For example, in Toivonen et al., (2008), seven regions are defined; and in Grasty et al., (2001), ten regions are used.

Alternatively Monte Carlo simulations can be performed without restrictions in sources availability. In Yi et al., (1997), the response matrix is 50 x 50, i.e. 50 energy bands are used and hence, 50 simulations.

These coefficients can have an angular dependence if the energy deposited in the detector varies with the angle of the incident gamma flux. In Grasty et al., (2001), a series of weighting factors are proposed to represent a real semi-infinite source. However in cylindrical detectors, like studied $LaBr_3$(Ce), deviations observed in detector response at different angles are small and, as it is proposed in Dombrowski, (2014), this angular dependence can be neglected.

#### 3.3.1.1 Calculation of conversion coefficients using Monte Carlo simulations

In this dissertation the conversion coefficients were determined by MC simulations using PENELOPE/penEasy (Sempau et al., 2011). The response of the detector, that is, the energy deposited in each energy region was simulated with broad parallel beams incident normally to the central axis of the monitor (left side of Fig. 3.14), each simulated beam with the middle energy of an energy region.

Following the definition of the ambient dose equivalent, the $H^*(10)$ value corresponding to each energy flux was obtained exchanging the monitor by the ICRU sphere (right side of Fig. 3.14). According to

$H^*(10)$ definition, the absorbed dose in the ICRU sphere was measured at a depth of 10 mm using concentric spherical regions with infinitesimal radius increase. Obtained value at this point is, by definition itself, the ambient dose rate for the simulated energy flux.

Selected energy bands in this dissertation together with obtained conversion coefficients are shown in Table 3.8 and Table 3.9, Monitor 1 and SpectroTRACER, respectively. For Monitor 1 they have been chosen similarly to energy bands proposed in Toivonen et al., (2008) and some more have been used for SpectroTRACER. Using these coefficients, three different fit functions have been defined in the energy ranges <140 keV, 140-830 keV and >830 keV, as it is shown in Fig. 3.15 (Monitor 1) and Fig. 3.16 f(SpectroTRACER). Using these fitting functions Equation (3.13) can be replaced by:

$$H^*(10) = \sum_{i=1}^{n} w_i(E_i) n_i E_i \tag{3.13}$$

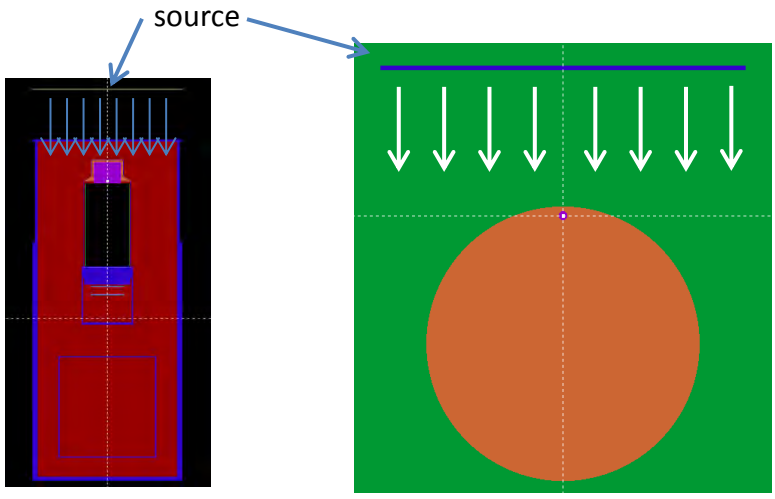


**Fig. 3.14.** *Left side.* Two-dimensional section view of the 1" x 1" $LaBr_3$(Ce) monitor exposed to a particular parallel energy flux. *Right side.* Two-dimensional section view of the ICRU sphere exposed to a particular parallel energy flux (views generated with PENELOPE's GVIEW2D visualization tool).

It should be pointed out that the shape described by values of $w_i$ is in direct link with the behaviour of the mass-absorption coefficients ratio between $LaBr_3$(Ce) and air (right side of Fig. 3.13). The sudden falls at low energies match with the peak in the ratio between coefficients.

| Energy region /keV | $w$ /nSv h$^{-1}$ keV$^{-1}$ s |
|---|---|
| 25 – 75 | $(9.18 \pm 0.12)\cdot10^{-3}$ |
| 75 - 105 | $(3.97 \pm 0.05)\cdot10^{-3}$ |
| 105 – 175 | $(3.90 \pm 0.01)\cdot10^{-3}$ |
| 175 – 205 | $(4.37 \pm 0.06)\cdot10^{-3}$ |
| 205 - 375 | $(5.98 \pm 0.08)\cdot10^{-3}$ |
| 375 - 585 | $(1.05 \pm 0.02)\cdot10^{-2}$ |
| 585 - 735 | $(1.28 \pm 0.32)\cdot10^{-2}$ |
| 735 - 925 | $(1.35 \pm 0.11)\cdot10^{-2}$ |
| 925 - 1435 | $(1.26 \pm 0.10)\cdot10^{-2}$ |
| 1435 - 3005 | $(9{,}83 \pm 0.38)\cdot10^{-3}$ |

**Table 3.8.** Conversion coefficients calculated for Monitor 1, 1" x 1" $LaBr_3$(Ce) crystal. Uncertainties quoted with $k$ = 2.

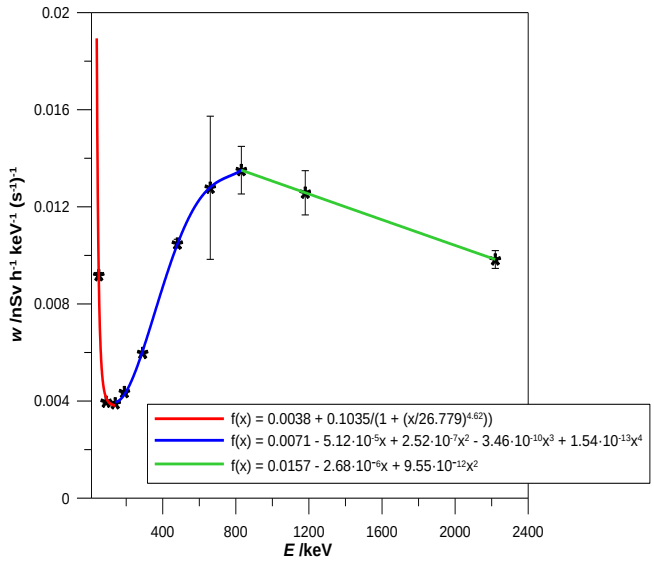


**Fig. 3.15.** Fitting functions obtained from calculated conversion coefficients for Monitor 1. Vertical bars show uncertainties ($k$ = 2).

| Energy region /keV | $w$ /nSv h$^{-1}$ keV$^{-1}$ s |
|---|---|
| 25 – 55 | $(7.56 \pm 0.08)\cdot10^{-3}$ |
| 55 - 65 | $(2.13 \pm 0.04)\cdot10^{-3}$ |
| 65 – 95 | $(1.63 \pm 0.02)\cdot10^{-3}$ |
| 95 – 105 | $(1.57 \pm 0.02)\cdot10^{-3}$ |
| 105 - 155 | $(1.48 \pm 0.02)\cdot10^{-3}$ |
| 155 - 205 | $(1.59 \pm 0.01)\cdot10^{-2}$ |
| 205 - 295 | $(1.81 \pm 0.01)\cdot10^{-2}$ |
| 295 - 505 | $(2.64 \pm 0.01)\cdot10^{-2}$ |
| 505 - 755 | $(3.53 \pm 0.02)\cdot10^{-2}$ |
| 755 - 985 | $(4.07 \pm 0.10)\cdot10^{-3}$ |
| 985 – 1315 | $(3.96 \pm 0.13)\cdot10^{-3}$ |
| 1315 – 1685 | $(3.82 \pm 0.19)\cdot10^{-3}$ |
| 1685 - 2315 | $(3.42 \pm 0.17)\cdot10^{-3}$ |
| 2315 – 2685 | $(3.20 \pm 0.40)\cdot10^{-3}$ |
| 2685 – 3115 | $(2.42 \pm 0.62)\cdot10^{-3}$ |

**Table 3.9.** Conversion coefficients calculated for SpectroTRACER, 1.5" x 1.5" $LaBr_3(Ce)$ crystal. Uncertainties quoted with $k$ = 2.

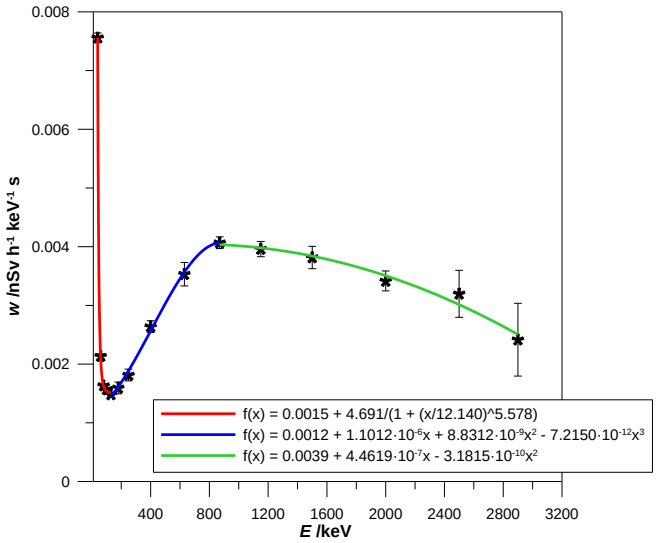


**Fig. 3.16.** Fitting functions obtained from calculated conversion coefficients for SpectroTRACER. Vertical bars show uncertainties ($k$ = 2).

### 3.3.1.2 Uncertainties using conversion coefficients

Applying propagation of errors to Equation (3.10), uncertainty in $H^*(10)$ can be calculated with the following expression:

$$u(H^*(10)) = \\ = \sqrt{\sum_{i=1}^{n}\left[(w_i(E_i)u(n_i)E_i)^2 + (\Delta w_i(E_i)n_i E_i)^2 + \left(w_i(E_i)n_i\frac{\Delta E_i}{2\sqrt{3}}\right)^2\right]} \quad (3.14)$$

Uncertainty $u(n_i)$ is associated to experimental number of counts $n_i$ and according to Poisson statistics is $\sqrt{n_i}$. Uncertainty in $\Delta E_i$ and $\Delta w_i(E_i)$ are type B, associated to the width of energy bands and to variations observed in the fitting functions respectively.

In case that conversion coefficients are experimentally determined, effects of scatterings should be also taken into account as a source of uncertainties (Dombrowski, 2014).

## 3.3.2 Validation of the methodology

### 3.3.2.1 Validation with a $^{137}$Cs point source

The conversion coefficients methodology is applied to the same measurement with a $^{137}$Cs point source used to validate the stripping methodology. Result obtained is shown in Table 3.10 together with calculated value with the stripping method using 10 keV energy band width.

| Source | $\dot{H}^*(10)_{theoretical}$ /μSvh$^{-1}$ | $\dot{H}^*(10)_{strip.\Delta E=10keV}$ /μSvh$^{-1}$ | $\dot{H}^*(10)_{conversion\ coeff.}$ /μSvh$^{-1}$ |
|---|---|---|---|
| $^{137}$Cs | 0.314 | $0.327 \pm 0.014$ | $0.30 \pm 0.04$ |

**Table 3.10.** $\dot{H}^*(10)$ from a $^{137}$Cs point source calculated with the stripping and conversion coefficients method. Uncertainties quoted with $k = 2$.

### 3.3.2.2 Validation in the LCD

Same irradiations performed at LCD used to validate the stripping method are used to validate this methodology. Results are shown in Table 3.11 for Monitor 1 and Table 3.18 for SpectroTRACER.

| $\dot{H}^*(10)$ /μSvh$^{-1}$ | $\dot{H}^*(10)_{calculated}$/μSvh$^{-1}$ | Relative difference (%) |
|---|---|---|
| 2.00 ± 0.12 | 1.84 ± 0.18 | -8 |
| 5.0 ± 0.4 | 4.6 ± 0.5 | -8 |
| 10.0 ± 0.6 | 9.1 ± 0.9 | -9 |
| 50.0 ± 2.9 | 46.7 ± 4.8 | -6.6 |
| 100 ± 5.9 | 95.7 ± 9.5 | -4.3 |

**Table 3.11.** $\dot{H}^*(10)$ obtained from Monitor 1 spectra in the LCD compared with nominal values (measurements with $t$ = 300 s). Uncertainties are quoted with $k$ = 2.

| $\dot{H}^*(10)$ /μSvh$^{-1}$ | $\dot{H}^*(10)_{calculated}$ /μSvh$^{-1}$ | Relative difference (%) |
|---|---|---|
| 2.00 ± 0.12 | 2.06 ± 0.01 | 3 |
| 10.0 ± 0.6 | 9.82 ± 0.15 | -1.8 |
| 50.0 ± 2.9 | 49.5 ± 0.6 | -1 |
| 200 ± 12 | 207 ± 6 | 3.5 |
| 2000 ± 117 | 2350 ± 51 | 17.5 |

**Table 3.12.** $\dot{H}^*(10)$ obtained from SpectroTRACER spectra in the LCD compared with nominal values (measurements with $t$ = 300 s). Uncertainties are quoted with $k$ = 2.

It can be observed that results do not differ substantially from ones obtained with the stripping method (see section 3.2.2.2). Although relative differences are greater for Monitor 1, values reported are about 10% lower than for SpectroTRACER, a similar

behaviour can be observed in calculated values with the stripping method (see Table 3.7 and Table 3.6).

## 3.4 Results

### 3.4.1 Measurements in a comparison at PTB

In the framework of the MetroERM project, a comparison campaign was organized at Physikalisch-Technische Bundesanstalt (http://www.ptb.de). Two scenarios were selected to analyse the response of several dose rate monitors and spectrometric detectors to reference dose rate values produced by artificial sources. Complete results and comparisons between devices will be published as a project delivery. Nevertheless, results obtained with Monitor 1 and Monitor 2 are shown in the following.

#### 3.4.1.1 Low-level underground laboratory

Measurements were performed at UDO II laboratory, defined at section 2.5.2. The goal of the measurements was to determine the inherent background of each monitor and the study of detector response at low dose rate range.

As it has been previously detailed, the inherent background of monitors was determined from a self-counting measurement performed in a lead castle, in order to subtract residual natural contribution in the lab. The stripping method was applied to Monitor 1 and Monitor 2 without any internal background subtraction, since actually it was the one to be measured. Results are shown in Table 3.13, together with value measured by a commercial monitor. Commercial model belongs to another group who kindly provide us their results. It can be observed that, in terms of $\dot{H}^*(10)$, the internal

background calculated for Monitor 2 is greater than for Monitor 1, while Monitor 2 and commercial monitor show closer values. The reason is the decay of the internal background due to $^{227}Ac$ $T_{1/2}$ (see

| Calculated value /nSv $h^{-1}$ (Monitor 1) | Calculated value /nSv $h^{-1}$ (Monitor 2) | Commercial monitor/nSv $h^{-1}$ |
|---|---|---|
| 57.4 ± 2.1 | 81.0 ± 2.5 | 86.9 ± 1.8 |

**Table 3.13.** Values of the inherent background obtained in the lead castle measurement.

section 2.5). Fig. 3.17 shows self-counting measurements obtained by the three monitors and the number of counts at $^{227}Ac$ region is clearly lower for Monitor 1.

UDO II background has a reference value of 1.4 nSv $h^{-1}$. Due to its unique conditions there is a calibration facility for photon radiation fields (Sáez-Vergara et al., 2007) (Fig. 3.18) which is the only one worldwide to be traceable to primary standards for dose rates of 100 nSv $h^{-1}$ and below.

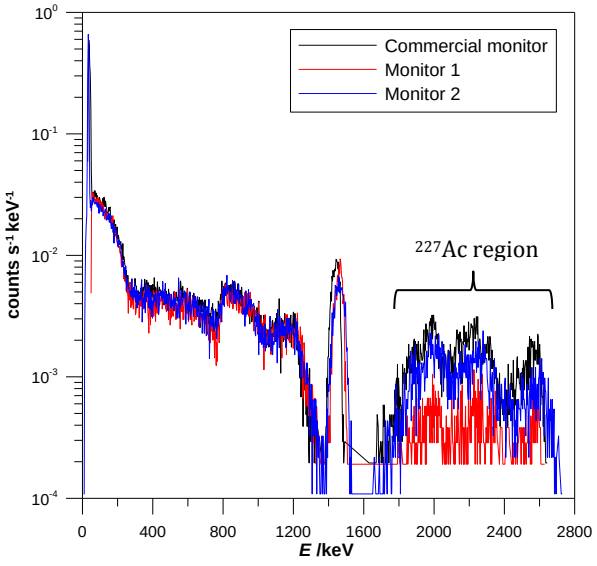


**Fig. 3.17.** Self-counting spectrum obtained inside the lead castle at UDO II by Monitor 1 and 2 and by a commercial one. All detectors are 1" x 1" $LaBr_3(Ce)$ monitors.

**Fig. 3.18.** Calibration facility at UDO II laboratory. Three monitors are on the platform in front of the shutter during exposures.

In order to study the sensitivity of both monitors in conditions of low dose rate range, detectors were installed in this irradiation facility in continuous measurement with t = 120 s. Sealed sources of $^{137}$Cs, $^{57}$Co, $^{241}$Am, $^{226}$Ra and $^{60}$Co were used to produce different values of $\dot{H}^*(10)$.

Net values calculated with stripping and coefficients methods compared with reference ones and with values reported by a Reuter-Stokes monitor are shown in Table 3.15 and Table 3.16. Laboratory background has been subtracted according to Equation (3.15).

$$\dot{H}_n^*(10) = \dot{H}_0^*(10) - \dot{H}_{UDO}^*(10) \qquad (3.15)$$

Where $\dot{H}_n^*(10)$ is the value reported for each source, $\dot{H}_0^*(10)$ is the calculated value from the measured spectra and $\dot{H}_{UDO}^*(10)$, is the background of the UDO II lab. The inherent background, the spectrum measured inside the lead castle has been subtracted.

The value $\dot{H}^*_{UDO}(10)$, with reference value 1.4 nSv h$^{-1}$, was calculated in two different ways. First, applying the stripping and coefficients methodologies to measured gamma spectra in the lab without any artificial source during t = 134 min (Monitor 1) and t = 522 s (Monitor 2). The other one is based on the linearity in detectors response. Four $^{137}$Cs radioactive sources with different strengths were used as they are listed in Table 3.15 and Table 3.16. The ratio between $\dot{H}_0$*(10) calculated values and reference ones may be the same in all these four measurements, since detector response to the photopeak energy (661.6 keV) is the same. In Fig. 3.19 and Fig. 3.20 are plotted $\dot{H}_0$*(10) calculated raw values with the stripping and conversion coefficients methodology respectively, against reference values. The intercept $y_0$ parameter of linear regressions should be identified as the laboratory background ($\dot{H}_{UDO}$*(10)). Table 3.14 reports UDO II calculated background values from lab measurements together with values obtained using linear regression. Reported background value in Table 3.15 and Table 3.16 is the average between two values reported in Table 3.14.

| | **Stripping methodology** | | **Conversion coeff. methodology** | |
|---|---|---|---|---|
| | **Calculated /nSv h$^{-1}$** | **Intercept in linear regression /nSv h$^{-1}$** | **Calculated /nSv h$^{-1}$** | **Intercept in linear regression /nSv h$^{-1}$** |
| **M1** | 6.1 ± 0.4 | 7.0 ± 2.5 | 3.4 ± 0.3 | 1.3 ± 1.3 |
| **M2** | 8.2 ± 1.7 | 9.4 ± 1.3 | 4.5 ± 0.5 | 4.0 ± 0.2 |

**Table 3.14.** $\dot{H}$*$(10)_{UDO}$ calculated with the stripping/conversion coefficients method to measured spectrum in the UDO lab with Monitor 1 and 2, together with value obtained from the linear regression of $^{137}$Cs measurements Uncertainties quoted with $k$ = 2.

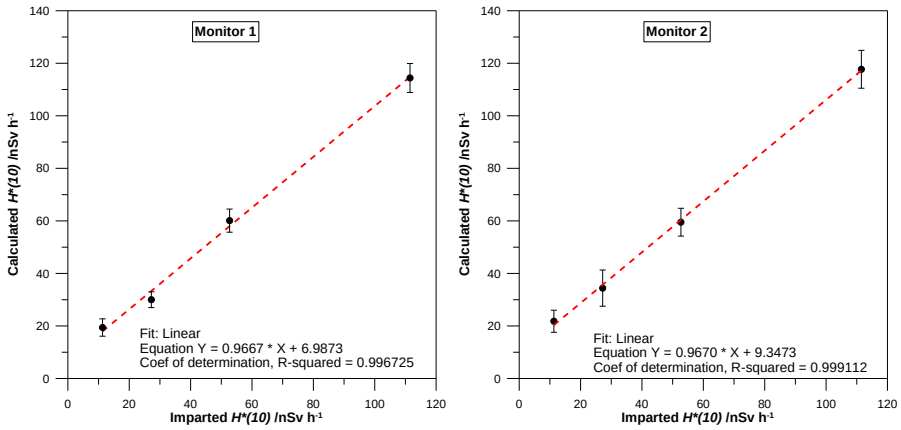


**Fig. 3.19.** Linear regression obtained from calculated $\dot{H}^*(10)$ with the stripping methodology. Measurements were performed with Monitor 1 (*left side*) and Monitor 2 (*right side*) at UDO II irradiator facility using four $^{137}$Cs radioactive sources. Intercept of the fit provides the inherent background in the laboratory.

| Source | Measured /nSv h$^{-1}$ (Reuter Stokes) | Calculated /nSv h$^{-1}$ (M1) | Calculated /nSv h$^{-1}$ (M2) | Reference /nSv h$^{-1}$ |
|---|---|---|---|---|
| UDO background | 1.3 ± 0.4 | 6.6 ± 1.3 | 8.8 ± 1.1 | 1.4 |
| $^{137}$Cs | 108.0 ± 1.3 | 107.9 ± 5.5 | 108.9 ± 7.2 | 111.5 |
| $^{137}$Cs | 52.0 ± 1.0 | 53.5 ± 4.4 | 50.7 ± 5.3 | 52.7 |
| $^{137}$Cs | 26.5 ± 1.3 | 23.4 ± 3.0 | 25.6 ± 6.9 | 27.2 |
| $^{137}$Cs | 10.7 ± 0.6 | 12.8 ± 3.3 | 13.0 ± 4.2 | 11.3 |
| $^{241}$Am | 13.3 ± 0.6 | 72.8 ± 19.4 | 67.4 ± 3.8 | 62.6 |
| $^{57}$Co | 144.2 ± 0.9 | 176.2 ± 4.4 | 158.8 ± 10.0 | 157.2 |
| $^{60}$Co | 104.3 ± 1.5 | 112.9 ± 9.5 | 111.3 ± 9.8 | 103.9 |
| $^{226}$Ra | 283.0 ± 1.7 | 281.8 ± 16.3 | 260.9 ± 3.3 | 283.0 |

**Table 3.15.** Calculated values of $H^*(10)$ obtained with the stripping methodology from $LaBr_3$(Ce) measurements. Several radioactive sources have been used. Uncertainties quoted with $k$ = 2.

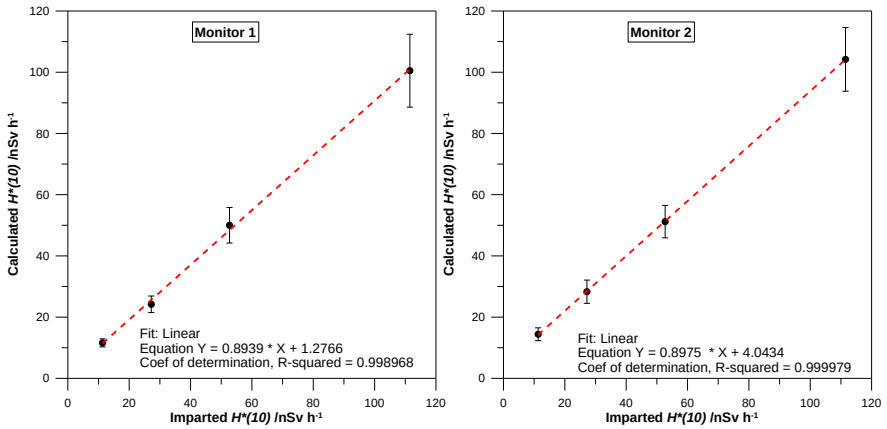


**Fig. 3.20.** Linear regression obtained from $H^*(10)$ calculated values with the conversion coefficients methodology. Measurements were performed with Monitor 1 (*left side*) and Monitor 2 (*right side*) at UDO II irradiator facility using four $^{137}Cs$ radioactive sources. Intercept of the fit provides the inherent background in the laboratory.

| Source | Measured /nSv $h^{-1}$ (Reuter Stokes) | Calculated /nSv $h^{-1}$ (M1) | Calculated /nSv $h^{-1}$ (M2) | Reference /nSv $h^{-1}$ |
|---|---|---|---|---|
| UDO background | 1.3 ± 0.4 | 2.4 ± 0.7 | 4.3 ± 0.3 | 1.4 |
| $^{137}Cs$ | 108.0 ± 1.3 | 98.1 ± 11.9 | 99.9 ± 10.4 | 111.5 |
| $^{137}Cs$ | 52.0 ± 1.0 | 47.6 ± 5.8 | 46.9 ± 5.3 | 52.7 |
| $^{137}Cs$ | 26.5 ± 1.3 | 21.8 ± 2.7 | 24.0 ± 3.8 | 27.2 |
| $^{137}Cs$ | 10.7 ± 0.6 | 9.2 ± 1.3 | 10.1 ± 2.1 | 11.3 |
| $^{241}Am$ | 13.3 ± 0.6 | 54.6 ± 5.0 | 70.8 ± 1.1 | 62.6 |
| $^{57}Co$ | 144.2 ± 0.9 | 152.2 ± 3.8 | 146.7 ± 11.4 | 157.2 |
| $^{60}Co$ | 104.3 ± 1.5 | 95.0 ± 2.5 | 95.7 ± 3.5 | 103.9 |
| $^{226}Ra$ | 283.0 ± 1.7 | 252.6 ± 7.2 | 245.7 ± 9.1 | 283.0 |

**Table 3.16.** Calculated values of $H^*(10)$ obtained with the conversion coefficients methodology from $LaBr_3(Ce)$ measurements. Several radioactive sources have been used. Uncertainties quoted with $k = 2$.

**Discussion**

Monitor 1 and Monitor 2 were measuring in the UDO II lab with almost no terrestrial nor cosmic contribution. These unique conditions allow the study of detectors response and sensitivity and, moreover, allow the measurement of devices internal contamination.

$LaBr_3(Ce)$ crystals have an inherent radioactivity due to the presence of $^{138}La$ and $^{227}Ac$ (see chapter 2.5). Results obtained in this section show values of 57.4 nSv $h^{-1}$ for Monitor 1 and 81.0 nSv $h^{-1}$. These values could be compared with terrestrial contamination, which highlights the importance to take this inherent background in consideration to avoid overestimations in measurements. Differences due to half-life of $^{227}Ac$ decay is around 30 nSv $h^{-1}$ between both crystals, this makes advisable to take this factor in consideration.

Measurements performed in the irradiation facility with several radioactive sources allows to evaluate the goodness of calculated $\dot{H}^*(10)$ values from different gamma spectra. Table 3.17 shows relative differences obtained for both monitors and using both methodologies according to reported results. Conversion coefficients method shows lower values than ones obtained with the stripping methodology however, it does not mean worst results: for $^{241}Am$, $^{57}Co$ and $^{60}Co$ reference values are between both calculation methods.

For the first $^{137}Cs$ source (reference $\dot{H}^*(10)$ = 111.5 nSv $h^{-1}$) relative difference obtained with the stripping method is similar to the obtained from measurement with the Reuter Stokes. In this case, calculated value with conversion coefficients shows more difference. Reason is that 661.6 keV is near to an inflection point in the response function of these detectors (see Fig. 3.15) and this also produces

greater uncertainties in calculated values. An additional correction may be recommended to be studied.

Differences obtained for 241Am source with calculated values are much smaller than difference obtained with reported with Reuter Stokes monitor. The reason is the underestimation of ionization chambers at low energies.

| | Relative difference /% | | | | |
|---|---|---|---|---|---|
| | | Stripping | | Conversion coefficients | |
| Source | Reuter Stokes | M1 | M2 | M1 | M2 |
| $^{137}$Cs-111.5 nSv h$^{-1}$ | -3.1 | -3.2 | -2.3 | -12.0 | -10.4 |
| $^{241}$Am-62.6 nSv h$^{-1}$ | -78.8 | 16.3 | 7.7 | -12.8 | 13.1 |
| $^{57}$Co-157.2 nSv h$^{-1}$ | -8.3 | 12.1 | 1.0 | -3.2 | -6.7 |
| $^{60}$Co-103.9 nSv h$^{-1}$ | 0.4 | 8.7 | 7.1 | -8.6 | 7.1 |
| $^{226}$Ra-283.0 nSv h$^{-1}$ | 0.0 | -0.4 | -7.8 | -10.7 | -13.2 |

**Table 3.17.** Relative differences to reference values obtained from measured values with Reuter Stokes and calculated values with the stripping and conversion coefficients method for both monitors.

### 3.4.1.2 Free Field

Measurements were performed in an almost flat lawn of ~85 x 120 m$^2$ at PTB facilities. Detectors response was studied with $^{60}$Co, $^{137}$Cs and $^{226}$Ra sealed sources. In addition a radioactive plume was artificially produced, also with sealed sources, in order to shape detectors sensitivity to $\dot{H}^*(10)$ variations.

Detectors were set in continuum measurement of t = 600s during more than 8h. In that period, organizers brought participant proves under different types of exposures. Results obtained to particular

sealed sources are shown in Table 3.18 and Table 3.19, using stripping and coefficients methods respectively. Terrestrial background has been subtracted according to Equation (3.16).

$$\dot{H}_n^*(10) = \dot{H}_0^*(10) - \dot{H}_{bkg}^*(10) \tag{3.16}$$

Where $\dot{H}_n^*(10)$ is the value reported for each source, $\dot{H}_0^*(10)$ is the calculated value from the measured spectra and $\dot{H}_{bkg}^*(10)$, is the terrestrial background of the free field also reported in tables. Spectrum of the inherent background has been subtracted from measured spectra.

The PTB team, organizers of the intercomparison, kindly supplied reference values and measurements from an ion chamber probe type Reuter Stokes. Uncertainties of the calculated values include type A and type B contributions.

Measurements obtained during plume exposure are shown in Fig. 3.21. Red line is the $\dot{H}^*(10)$ reference level and blue dots are calculated values from Monitor 1 and 2 measured spectra, stripping methodology was used. These plots have been made by intercomparison organizers from data we supplied.

| (nSv h$^{-1}$) | Reference values | Measured (Reuter Stokes) | Calculated (Monitor 1) | Calculated (Monitor 2) |
|---|---|---|---|---|
| **Terrestrial background** | | 41.9 ± 3.7 | 47.9 ± 5.4 | 48.5 ± 5.9 |
| **$^{137}$Cs** | 281.2 ± 8.4 | 275.6 ± 3.7 | 273.5 ± 8.3 | 258.0 ± 7.7 |
| **$^{60}$Co** | 391.3 ± 9.0 | 402.9 ± 5.3 | 377.0 ± 15.7 | 357.0 ± 15.0 |
| **$^{226}$Ra** | 381.4 ± 11.6 | 381.4 ± 4.6 | 360.0 ± 17.9 | 329.0 ± 15.9 |

**Table 3.18.** Calculated mean values of $\dot{H}^*(10)$ obtained with the stripping method. Uncertainties quoted with $k$ = 2.

| (nSv h$^{-1}$) | Reference values | Measured (Reuter Stokes) | Calculated (Monitor 1) | Calculated (Monitor 2) |
|---|---|---|---|---|
| **Terrestrial background** | | 41.9 ± 3.7 | 43.9 ± 0.9 | 34.7 ± 1.7 |
| **$^{137}$Cs** | 281.2 ± 8.4 | 275.6 ± 3.7 | 258.1 ± 25.0 | 249.2 ± 21.1 |
| **$^{60}$Co** | 391.3 ± 9.0 | 402.9 ± 5.3 | 361.0 ± 8.2 | 346.1 ± 7.9 |
| **$^{226}$Ra** | 381.4 ± 11.6 | 381.4 ± 4.6 | 342.0 ± 8.5 | 324.6 ± 10.0 |

**Table 3.19.** Calculated mean values of $\dot{H}^*(10)$ obtained with the coefficients method. Uncertainties quoted with $k = 2$.

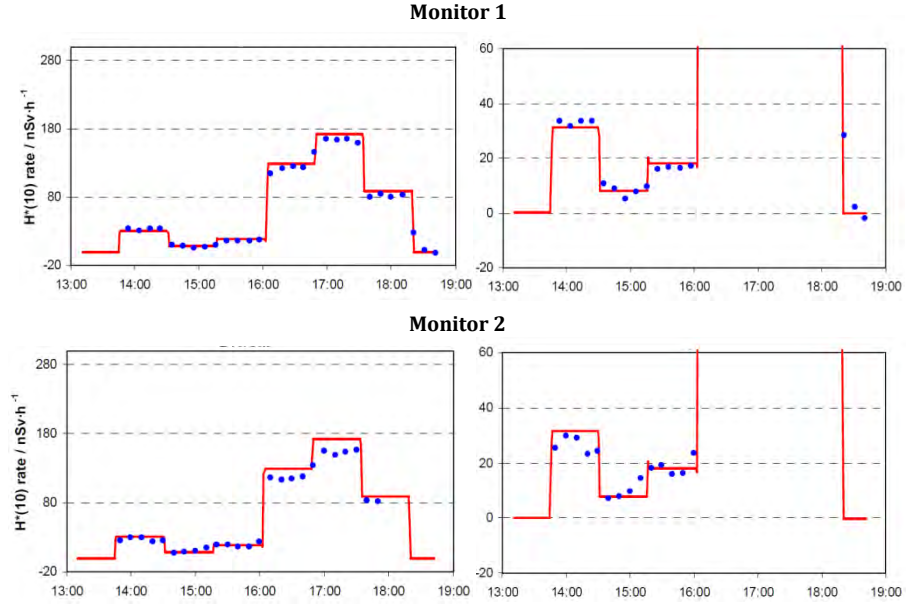


**Fig. 3.21.** Calculated $\dot{H}^*(10)$ values from Monitor 1 (*up*) and Monitor 2 (*down*) measured spectra during a plume simulation exposure. Right plots are a zoom of low dose rates region. Red line represents the calculated reference level and blue dots are calculated values applying the stripping method.

**Discussion**

In the free field both monitors were in continuous measurement during several hours. During this time radioactive sources were used to produce artificial contamination, calculated values of $\dot{H}^*(10)$ are shown in results section, relative differences with reference values are listed in Table 3.20.

| | | Relative difference /% | | | |
|---|---|---|---|---|---|
| | | Stripping | | Conversion coefficients | |
| Source | Reuter Stokes | M1 | M2 | M1 | M2 |
| $^{137}$Cs-281.2 nSv h$^{-1}$ | -2.0 | -2.7 | -8.3 | -8.2 | -11.4 |
| $^{60}$Co-391.3 nSv h$^{-1}$ | 3.0 | -3.6 | -8.8 | -7.7 | -11.6 |
| $^{226}$Ra-381.4 nSv h$^{-1}$ | 0.0 | -5.6 | -13.7 | -10.3 | -14.9 |

**Table 3.20.** Relative differences to reference values obtained from measured values with Reuter Stokes and calculated values with the stripping and conversion coefficients method for both monitors.

As it has been observed in previous section, values calculated with conversion coefficients method are lower than values calculated with stripping. However, in this case all calculated values are lower than reference ones.

## 3.4.2 Long-time measurements of ambient dose equivalent rate values

At the roof of the INTE facilities it is installed Monitor 1, a 1" x 1"·$LaBr_3$(Ce), measuring continuously with acquisition times $t$ = 600 s or $t$ = 900 s. Also it is installed a proportional counter model RS04L/WEB from Bitt Technology Company. This probe reports $\dot{H}^*(10)$ values every 600 s and sends the data to the French

radiological surveillance network, managed by l'Institut de Radioprotection et de Sûrete Nucléaire (IRSN).

Spectra measured with the $LaBr_3$(Ce) detector is used to obtain values of ambient dose rate equivalent applying two methodologies described previously: stripping method and conversion coefficients. These values are compared with data provided by the proportional counter. Although it is known that these probes have an overestimation at high energies and, usually, ionization chambers are recommended as a reference monitors, the aim of this comparison is to show if calculated data performance is the same for data provided by a commercial monitor. That is, the aim is to check if $LaBr_3$(Ce) can be so sensitivity with ambient dose equivalent rate values as a dose rate monitor. This comparison has been carried out over a year (period 2014-2015).

In order to compare $\dot{H}^*(10)$ results obtained applying the stripping method with values obtained with an ambient dose rate monitor, as the RS04/WEB_R probe, cosmic radiation should be taken in consideration. $LaBr_3$(Ce) monitors do not interact with cosmic radiation in the same manner as proportional counters, so a calculated value is added a posteriori using Equation 2.25, which takes into account pressure oscillations. Even though the proportional counter is a different model, the value of $a_c$ = 0.142 ± 0.004 nGy $hPa^{-1}$.

Usually, energy ranges in gamma spectrometry are up to 2000 keV. However, as it has been explained in this chapter, in the stripping methodology counts in high channels have direct effects on low energy channels. Therefore, in this dissertation it has been used an energy range of 40 keV – 3000 keV. $\dot{H}^*(10)$ calculated values with both methodologies are shown below for significant weeks of each

season. With the aim to study the effect of considering less channels, values are compared in the next section with results obtained using an energy range of 40 keV – 2000 keV.

For each week results obtained from the dose rate monitor RS04L/WEB are compared with values calculated from the $LaBr_3$(Ce) monitor with the stripping method (left) and with conversion coefficients (right). Also values of pressure and rain are reported in order to show the relation between radon progeny washout and $\dot{H}^*(10)$ peaks. Meteorological information is obtained from a station located at 41.379N, 2.105E, 79 m a.s.l., close to INTE-UPC facilities, which belongs to the weather station network of the Meteorological Service of Catalonia.

More results obtained with the stripping methodology are reported in Appendix 3, covering 1-year period.

### 3.4.2.1 Energy Range 40-3000 keV

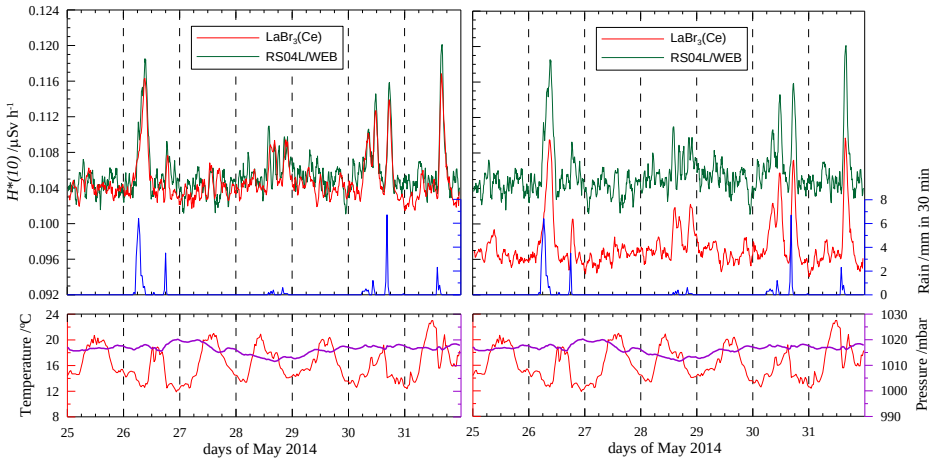


**Fig. 3.22.** Running average of the $H^*(10)$ values obtained with the stripping method (*left side*) and conversion coefficients (*right side*) compared with ones provided by the monitor RS04L/WEB. Both plots refer to the last week of May 2014 and show meteorological values (pressure, temperature and rain).

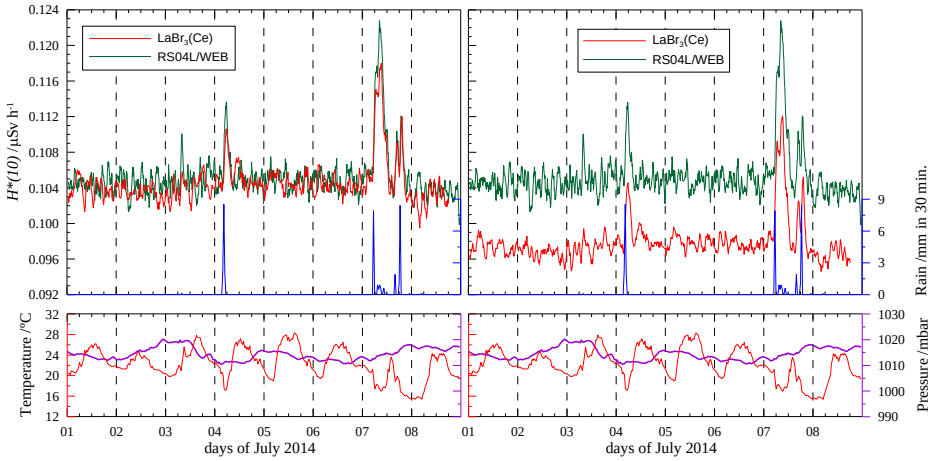


**Fig. 3.17.** Running average of the $H^*(10)$ values obtained with the stripping method (*left side*) and conversion coefficients (*right side*) compared with ones provided by the monitor RS04L/WEB. Both plots refer to the first week of July 2014 and show meteorological values (pressure, temperature and rain).

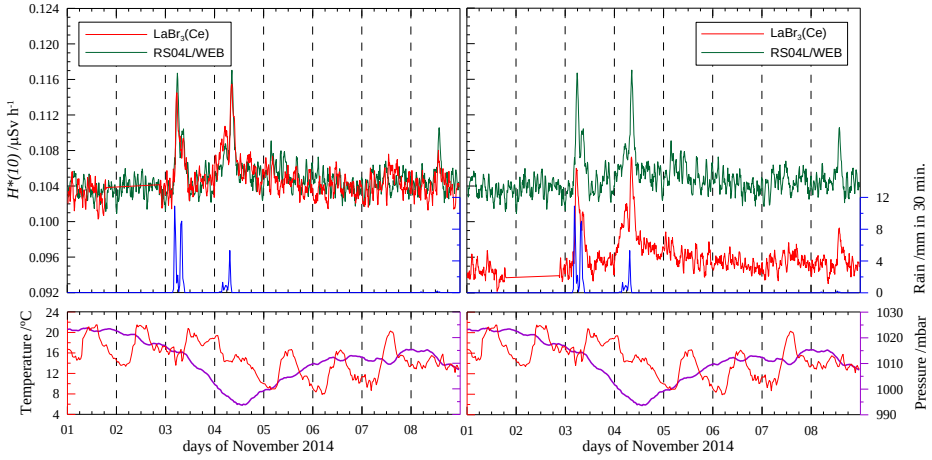


**Fig. 3.18.** Running average of the $H^*(10)$ values obtained with the stripping method (*left side*) and conversion coefficients (*right side*) compared with ones provided by the monitor RS04L/WEB. Both plots refer to the first week of November 2014 and show meteorological values (pressure, temperature and rain).

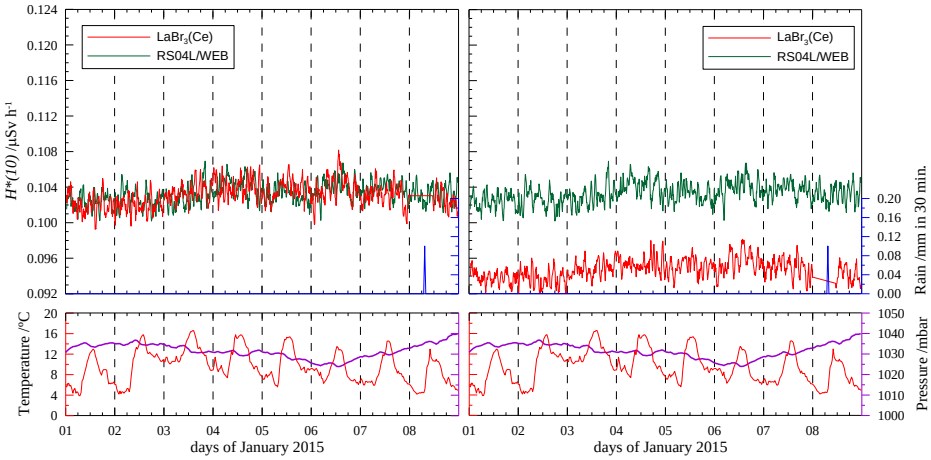


**Fig. 3.19.** Running average of the $H^*(10)$ values obtained with the stripping method (*left side*) and conversion coefficients (*right side*) compared with ones provided by the monitor RS04L/WEB. Both plots refer to the first week of January 2015 and show meteorological values (pressure, temperature and rain).

| | **May 2014** | **Jul. 2014** | **Nov. 2014** | **Jan. 2015** |
|---|---|---|---|---|
| **Stripping** | 1.007 ± 0.059 | 1.005 ± 0.057 | 1.005 ± 0.064 | 0.998 ± 0.063 |
| **Conv. coeff.** | 1.084 ± 0.059 | 1.073 ± 0.056 | 1.096 ± 0.064 | 1.087 ± 0.065 |

**Table 3.21.** Ratio between values obtained with the dose rate monitor RS04L and calculated values with stripping / conversion coefficients method. Uncertainties quoted with $k = 2$.

### 3.4.2.2 Energy Range 40-2000 keV

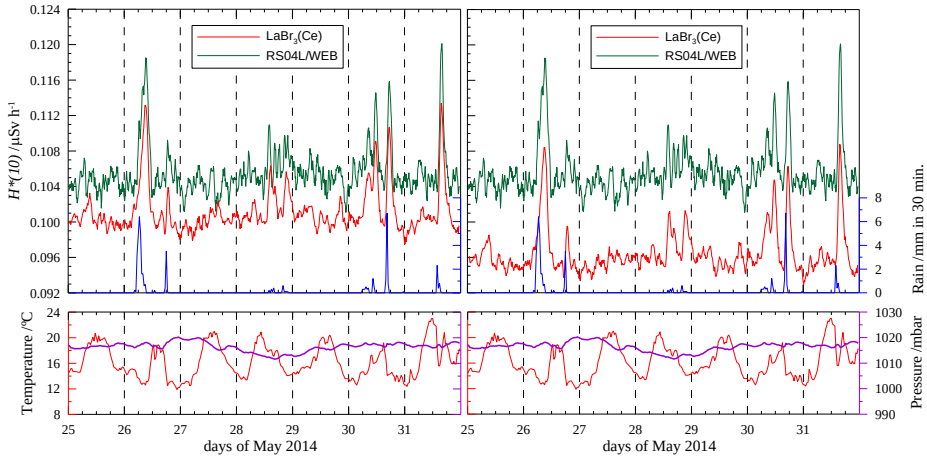


**Fig. 3.20.** Running average of the $H^*(10)$ values obtained with the stripping method (*left side*) and conversion coefficients (*right side*) compared with ones provided by the monitor RS04L/WEB. It has been considered an energy range up to 2000 keV. Both plots refer to the last week of May 2014 and show meteorological values (pressure, temperature and rain).

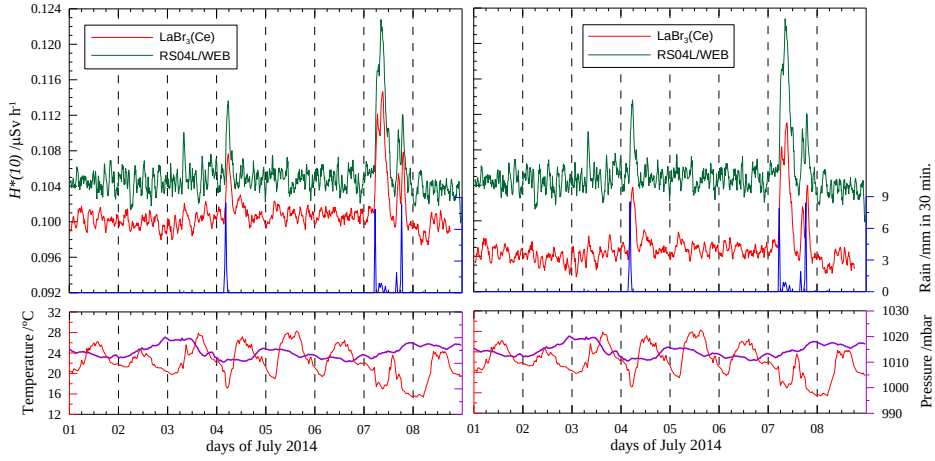


**Fig 3.21.** Running average of the $H^*(10)$ values obtained with the stripping method (*left side*) and conversion coefficients (*right side*) compared with ones provided by the monitor RS04L/WEB. It has been considered an energy range up to 2000 keV. Both plots refer to the last week of May 2014 and show meteorological values (pressure, temperature and rain).

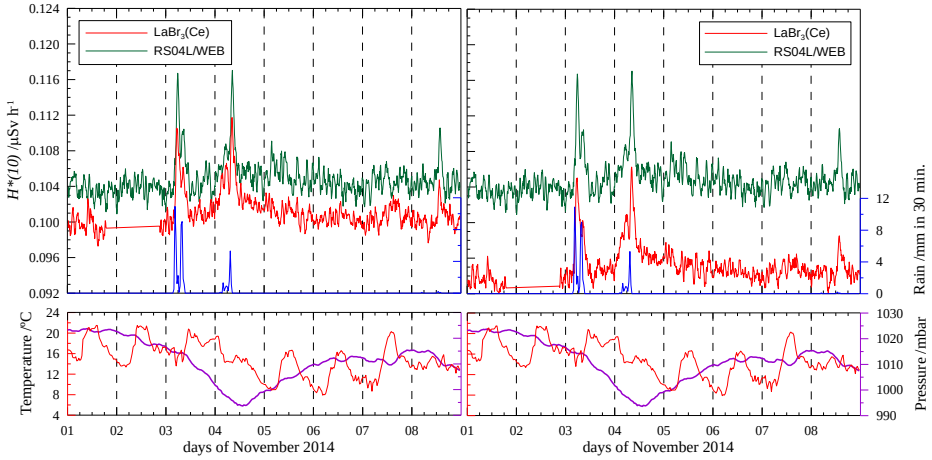


**Fig. 3.22.** Running average of the $H^*(10)$ values obtained with the stripping method (*left side*) and conversion coefficients (*right side*) compared with ones provided by the monitor RS04L/WEB. It has been considered an energy range up to 2000 keV. Both plots refer to the first week of November 2014 and show meteorological values (pressure, temperature and rain).

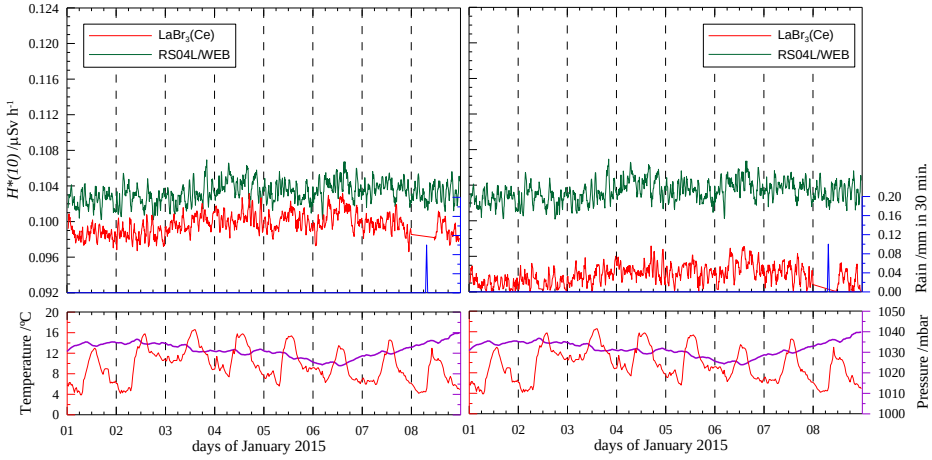


**Fig. 3.23** Running average of the $H^*(10)$ values obtained with the stripping method (*left side*) and conversion coefficients (*right side*) compared with ones provided by the monitor RS04L/WEB. It has been considered an energy range up to 2000 keV. Both plots refer to the first week of January 2015 and show meteorological values (pressure, temperature and rain).

| | May 2014 | Jul. 2014 | Nov. 2014 | Jan. 2015 |
|---|---|---|---|---|
| **Stripping** | 1.044 ± 0.056 | 1.041 ± 0.053 | 1.040 ± 0.058 | 1.033 ± 0.058 |
| **Conv. coeff.** | 1.096 ± 0.059 | 1.084 ± 0.056 | 1.105 ± 0.064 | 1.097 ± 0.065 |

**Table 3.22.** Ratio between values obtained with the dose rate monitor RS04L and calculated values with stripping / conversion coefficients method. It has been considered an energy range up to 2000 keV. Uncertainties quoted with $k = 2$.

**Discussion**

$\dot{H}^*(10)$ has a known a dependence of some meteorological variables. Probably the most studied variation is that produced by rainy periods (Blaauboer and Smetsers, 1996). Rain produces a washout of radon in air (see section 3.4.3) and, as a consequence, accumulated descendants on soil produce an increase in $\dot{H}^*(10)$. In all plots this effect can be observed, peaks of calculated and measured $\dot{H}^*(10)$ values coincide with measured rainy periods.

Another meteorological variable which has influence on $\dot{H}^*(10)$ is the pressure, due to the thickness of the atmosphere and its effect on cosmic radiation (Cortès, 2001). This effect can be clearly observed in the plot of January 2015 period, oscillations on $\dot{H}^*(10)$ values are inverse to oscillations in pressure.

Results in sections 3.4.2.1 and 3.4.2.2 show that values calculated with the stripping method, are in a very good agreement with values obtained with the RS04/WEB_R. However the goal of this section is to study the sensitivity of calculation methods, and both methodologies show the same response. Actually the gap between values obtained with the stripping method and coefficients method is constant over

time and is similar to results obtained in section 3.4.1. In Fig. 3.30 it is displayed the ratio between both methodologies, from the linear dependence the gap can be set to ~8 nSv $h^{-1}$ (~5 nSv $h^{-1}$) when an energy range up to 3000 keV (2000 keV) is considered. This gap is in agreement with results obtained in section 3.4.1.

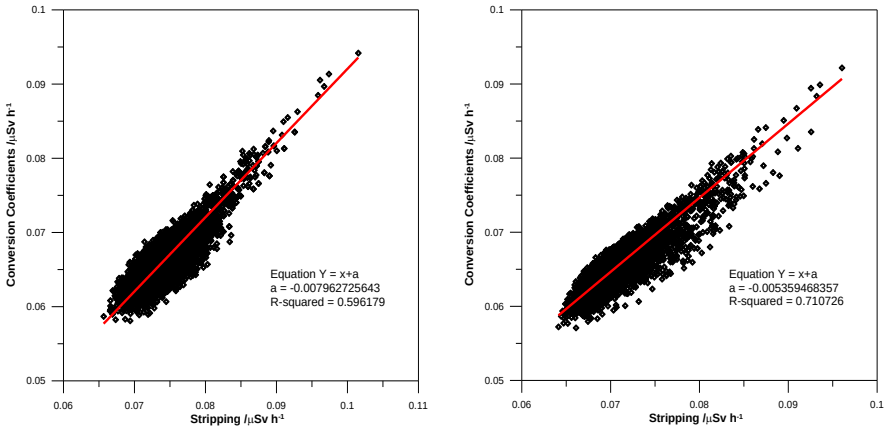


**Fig. 3.30.** Ratio between $\dot{H}^*(10)$ values obtained with the stripping method and coefficients method. *Left side.* Energy range 40-3000 keV. *Right side.* Energy range 40-2000 keV.

## 3.4.3 Measurements of $^{222}$Rn and progeny

Radon is a radioactive noble gas. Its most stable isotope is $^{222}$Rn with $T_{1/2}$ = 3.8 days, which is a decay product of $^{226}$Ra from the $^{238}$U decay chain. It decays by alpha emission and it is colourless, odourless and tasteless so, the main effects on the population are due to its inhalation and contributes to the natural radiation to which people are exposed. Because of radium, and hence radon, is a common element in building materials, a lot of studies have been performed over the years with the aim to determine its concentration in air and

its health effects (Grossi et al., 2012; Kendall and Smith, 2002; Porstendörfer, 1994).

Radon progeny or radon daughters are shown in Fig. 3.31. From this chain, $^{214}$Pb and $^{214}$Bi have gamma emissions with enough probability and energy to be detected by environmental dose rate monitors. In such a way, during rainy periods, the radon wash out of the air accumulates radon daughters on the soil (Cortes et al., 2001; Minato, 1980) and it can be observed an increase in the ambient dose equivalent rate, as well as an increase in the count rate at 609.32, 1120.3 and 1764.5 keV ($^{214}$Bi) and 295.2 and 351.9 keV ($^{214}$Pb) energies.

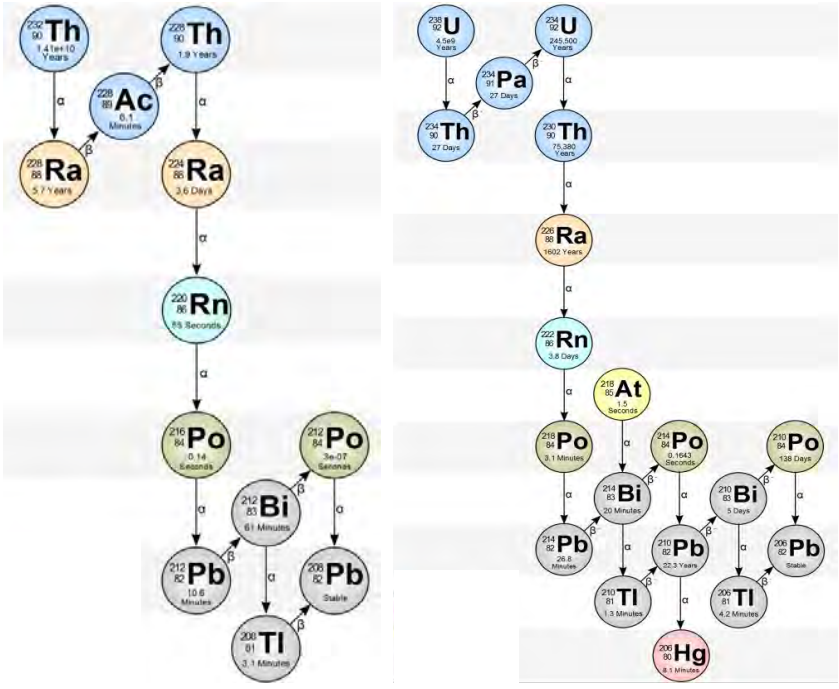


**Fig. 3.31.** $^{238}$U and $^{232}$Th series (Decay chain, n.d.)

Besides the effects of rain, radon concentration in air suffers daily and seasonal variations as a consequence of changes in the atmospheric boundary layer (Galmarini, 2006; Vargas et al., 2015). With the aim to see if these variations could have a direct influence on the ambient dose equivalent rate, measurements in the facilities of the INTE-UPC and at ESMERALDA (CIEMAT, Madrid) were performed.

### 3.4.3.1 Measurements at INTE-UPC

The station at INTE-UPC is the one defined at the beginning of this chapter (see section 3.2). In this facility, the monitor used to measure $^{222}$Rn concentration is based on alpha spectrometry of positive ions of $^{218}$Po which are electrostatically collected on a Passivated Implanted Planar Silicon (PIPS) detector surface by an electrostatic field inside a spherical volume of approximately 20 l. The monitor has been developed at INTE and is named ARMON. A scheme is shown in Fig. 3.32 and it is well-described and characterized elsewhere such in (Grossi et al., 2012; Vargas et al., 2015).

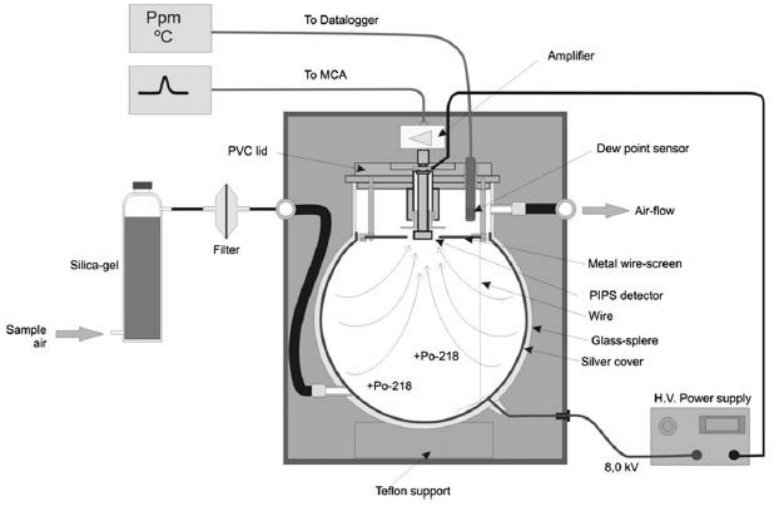


**Fig. 3.32.** Scheme of the electrostatic sphere used to measure $^{222}$Rn concentration in the atmosphere (Grossi et al., 2012).

The monitor for continuously air radon progeny measurement is named RAPROM. It is a self-developed system based on $\alpha$-spectrometry which was described in Vargas et al., (2004). A

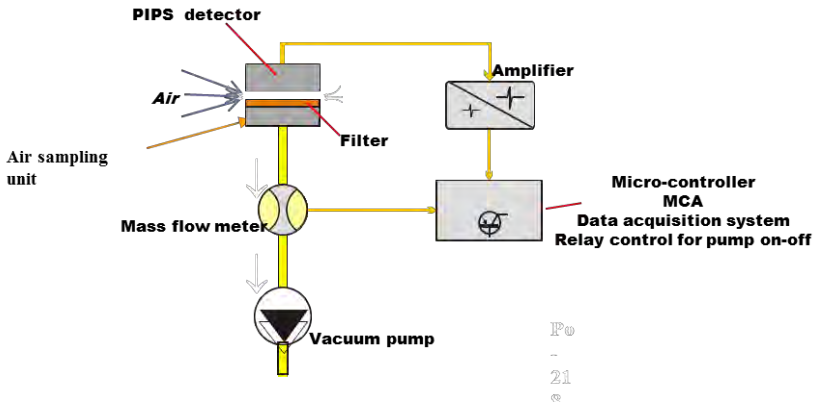


**Fig. 3.33.** Scheme of the $^{222}$Rn progeny measuring system.

scheme of the monitor is shown in Fig. 3.33, being the amplifier the model AMP01-03 from Sarad GmbH (http://sarad.de/) and the Multi-channel anal**y**zer a PALMTOP MCA8k-01 developed by the Institute of Nuclear Research of the Hungarian Academy of Science, MTA Atomki.

ARMON and RAPROM have been measuring during several months of the period 2014-2015, covering a time period from October 2014 to May 2015. In Fig. 3.34 are shown monthly results for $^{222}$Rn together with $^{218}$Po, $^{214}$Pb and $^{214}$Bi concentrations. Also meteorological variables are shown for each month: wind velocity, absolute pressure, wind direction, relative humidity, temperature and rain. Meteorological information is obtained from a station located at 41.379N, 2.105E, 79 m a.s.l., close to INTE-UPC facilities, which belongs to the weather station network of the Meteorological Service of Catalonia.

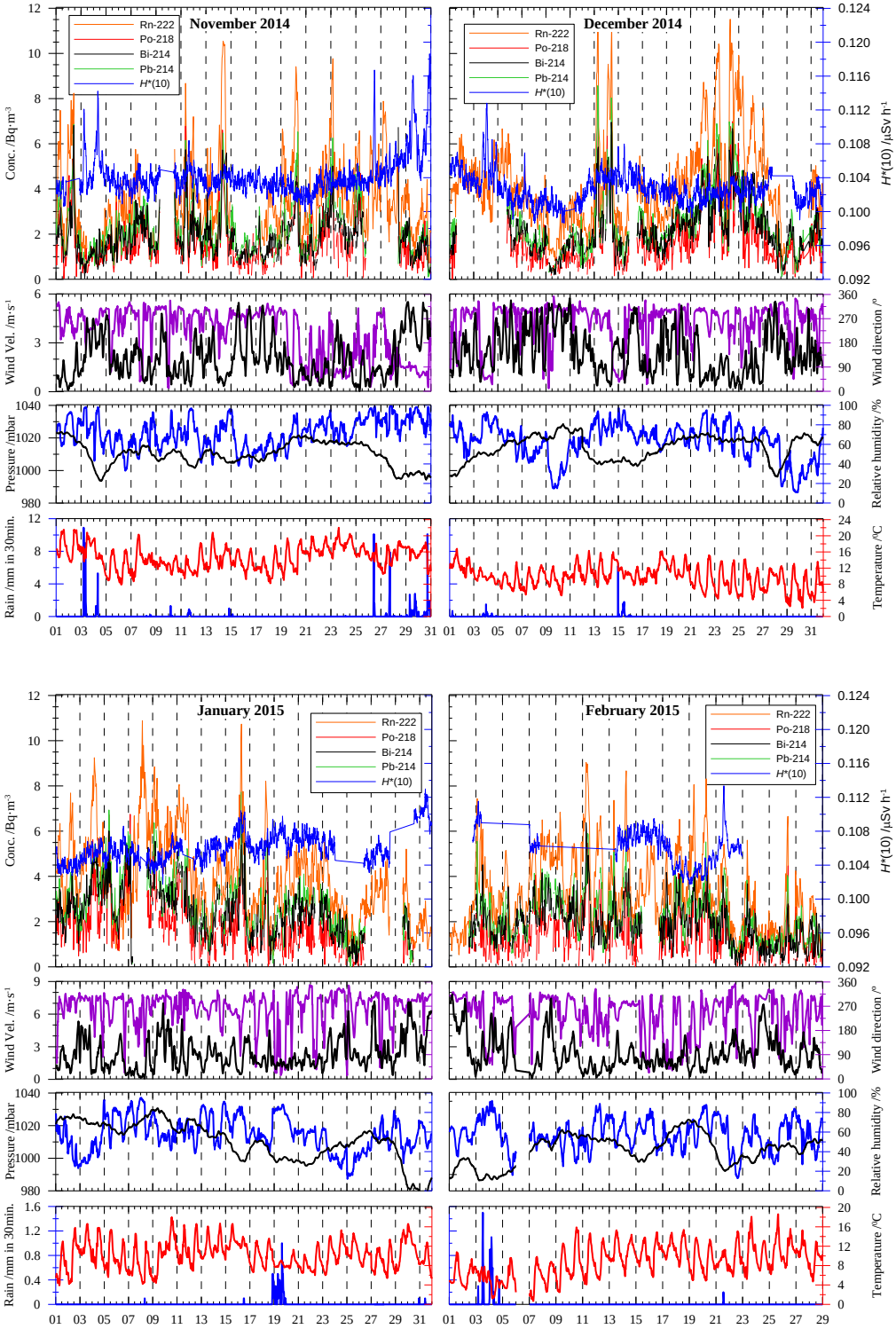
November 2014
December 2014
January 2015
February 2015
Rn-222
Po-218
Bi-214
Pb-214
H*(10)
Conc. /Bq·m-3
H*(10) /μSv h-1
Wind Vel. /m·s-1
Wind direction /°
Pressure /mbar
Relative humidity /%
Rain /mm in 30min.
Temperature /°C

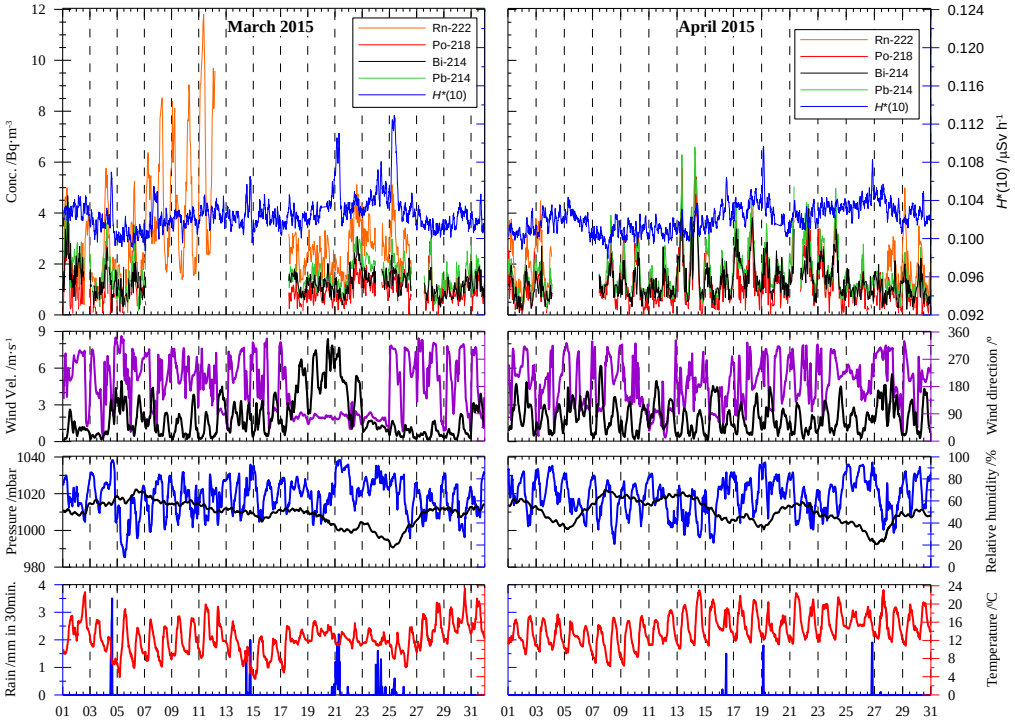


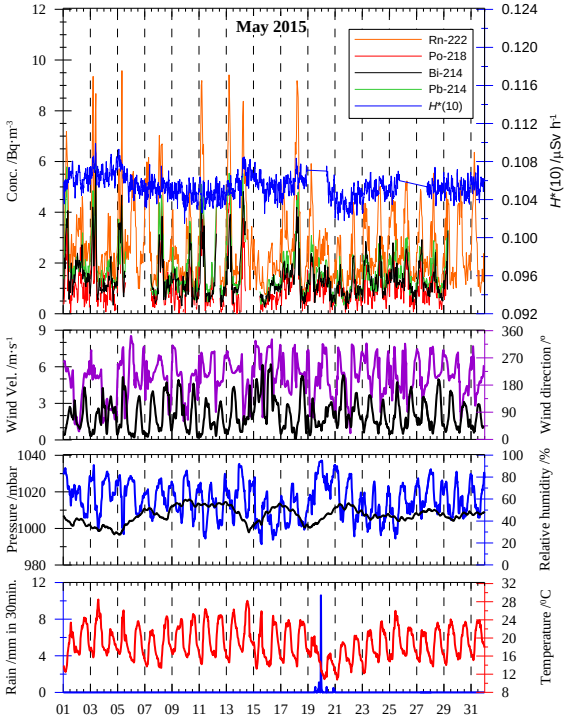


**Fig. 3.34.** Monthly $^{222}Rn$ and daughters ($^{218}Po$, $^{214}Pb$ and $^{214}Bi$) measured concentrations together with meteorological variables: wind velocity, absolute pressure, wind direction, relative humidity, temperature and rain obtained from http://meteo.cat/.

**Discussion**

It can be observed that radon and its daughters show a similar behaviour. Low winds, i.e. with calm conditions, are associated to higher $^{222}Rn$ concentrations since radon exhaled accumulates in the lower atmospheric layers, as it is numerically shown in Table 3.20. In addition $^{222}Rn$ concentration is enhanced by winds from NW direction, that is, from the Colleserola hill, richer in radon content than winds coming from the sea. However, it is not possible to clearly observe a direct relation between rainy events and decrease in radon concentration, as it actually happens due to wash out of air.

The effects of air concentration variations of $^{222}Rn$ and daughters on the *H*(10)* value reported by the WEBDL0501 dose rate monitor are analysed with Pearson correlations on Table 3.21. It can be observed that there is no clearly correlation from November to February, however from March onwards there is a low positive correlation with values ~0.2. This can be explained looking to variations of $^{222}Rn$ and daughters in Fig. 3.34; warm months show greater oscillations in concentrations and hence, effects on $\dot{H}^*(10)$ grow relevant. Anyway, previous works (Blaauboer and Smetsers, 1996) stablish a conversion factor of 0.364 nSv $h^{-1}$ $Bq^{-1}$ $m^3$ for $^{214}Bi$ and 0.056 nSv $h^{-1}$ $Bq^{-1}$ $m^3$ for $^{214}Pb$. Since concentrations of $^{214}Pb$ and $^{214}Bi$ are <10 Bq $m^{-3}$, they are insufficient to produce great variations in the *H*(10)*.

Daily behaviour of $^{222}Rn$ concentration is shown in Fig. 3.35. Each hour is an average over the three months of each season (22th of September to 21th of December, autumn; 21th of December to 20th of March, winter; and 20th of March to 21th of June, spring). It can be observed the characteristic increase during night hours and a decrease in concentration with the sun rise. The position of the

mixing layer during night is commonly near to zero, avoiding air mixing and producing and accumulation of radon at lowest layers; with sunny hours, position of mixing layer increases and concentration of $^{222}Rn$ starts to go down. Hence, the position of maximum and minimum varies following the sunrise and the sunset. Maximum values are 4.5-5 Bq $m^{-3}$ and minimum values are ~3 Bq $m^{-3}$ in autumn and winter and ~1.5 Bq $m^{-3}$ in the springtime. These values are in agreement with those reported in Cortès, (2001). Because sunny months facilitate the rise of mixing layer, the oscillation between maximum and minimum in radon concentration becomes greater.

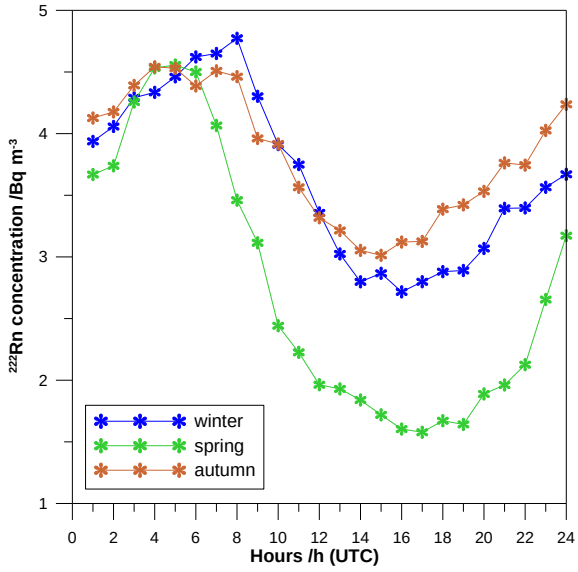


**Fig. 3.35.** Diurnal variation of $^{222}Rn$ concentration in each measured season.

| Pearson Correlation | | | | | | |
|---|---|---|---|---|---|---|
| *Nov 2014* | *Dec 2014* | *Jan 2015* | *Feb 2015* | *Mar 2015* | *Apr 2015* | *May 2015* |
| -0.117 | 0.139 | 0.085* | 0.027 (0.502) | 0.266 | 0.255 | 0.267 |

**Table 3.21.** Pearson correlation between EEDC and *H*(10)*. Asterisk indicates significance $p < 0.005$ and values in parenthesis correspond to $p > 0.005$; other values have $p < 0.001$.

| Pearson Correlation | | | | | | |
|---|---|---|---|---|---|---|
| *Nov 2014* | *Dec 2014* | *Jan 2015* | *Feb 2015* | *Mar 2015* | *Apr 2015* | *May 2015* |
| -0.406 | -0.436 | -0.311 | -0.363 | -0.333 | -0.489 | -0.469 |

**Table 3.20.** Pearson correlation between $^{222}Rn$ concentration and wind velocity. Values have a significance $p < 0.001$.

### 3.4.3.2 Measurements at ESMERALDA-CIEMAT

*This section in based on the submitted paper Vargas et al., 2017.*

The station ESMERALDA was established at CIEMAT premises (Madrid, Spain) in 1996 as a reference site for the study of the radiation instruments aimed to perform continuous or long-time investigations of the environmental radiation and airborne radioactivity. Different passive and active devices monitor the environmental external radiation dose in a continuous way. The influence of meteorological parameters, radon progeny air

concentrations and radioactive aerosols is also monitored with specific instruments. A more detailed description of this station, including the installed instruments and the measurements carried out can be found elsewhere (Sáez-Vergara et al., 2004, 1996).

Shown below the calculated $\dot{H}^*(10)$ using stripping and conversion factors, together with the $\dot{H}^*(10)$ obtained from the RS monitor for several months of 2016 (rest of months can be seen on Appendix 3) The data corresponding to the RS were provided by ESMERALDA station (Sáez Vergara J.C. 2016).

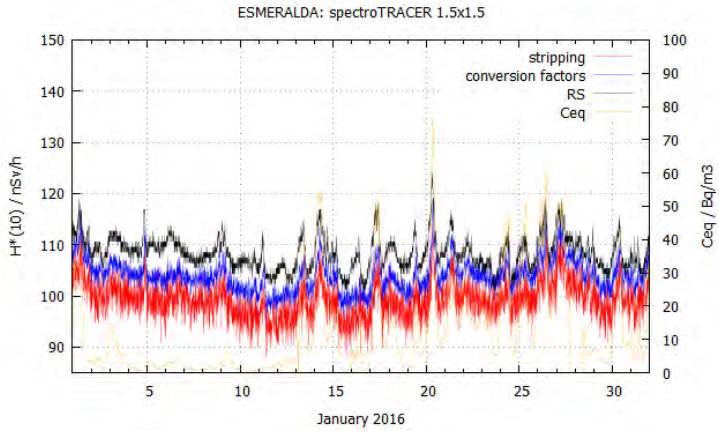


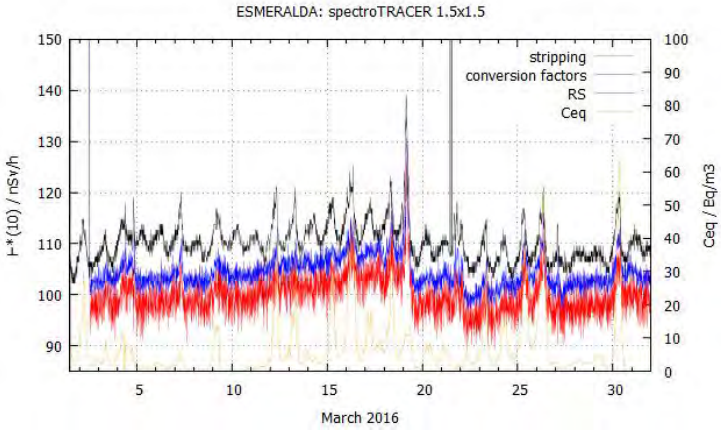

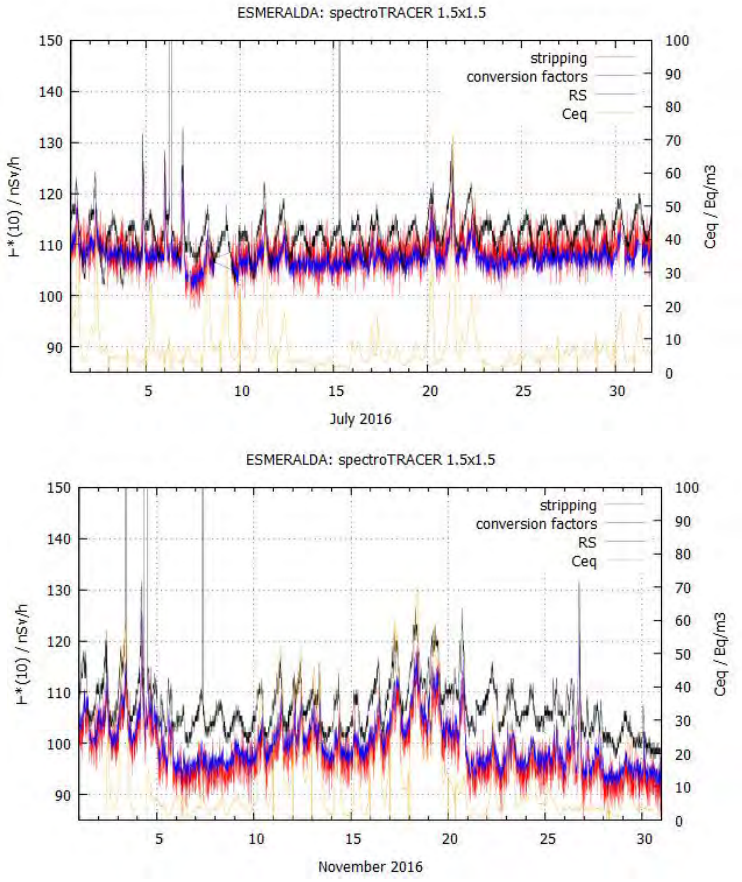


**Fig. 3.36.** $\dot{H}^*(10)$ rates calculated with stripping (red line), conversion factor (blue line) and compared with RS monitor during several months of 2016. Radon progeny pattern is also shown (orange line).

## Discussion

It can be shown that the pattern obtained with different methods for $\dot{H}^*(10)$ calculation is similar. In order to compare the $\dot{H}^*(10)$ calculated using conversion factors applied to the spectra measured by the spectrometric monitor and values from RS monitor, a constant value of 45 nSv $h^{-1}$ have been subtracted to the RS monitor. This value

is approximately the contribution of the cosmic radiation to the RS monitor.

$\dot{H}^*(10)$ values calculated from the spectrometric monitors and measured by RS are quite similar. The off-set between calculated $\dot{H}^*(10)$ maintains constant over time. However, in some periods, for example during March 2016, it can be appreciated some differences in the pattern compared to the RS monitor. This difference could be explained by the different behaviour and properties between both monitors. For example, response of the monitors to cosmic radiation and the difference of the deposition rate on the walls of the monitors due to the housing materials could explain partially these differences.

As it has been also observed in section 3.4.2, during rainy periods there is an increase in $H^*(10)$ values due to the fact that radon progeny is soil deposited. Here in addition, there is a daily variation in $\dot{H}^*(10)$, still without rain, as direct consequence of radon progeny concentration variation in the air. In Esmeralda station, oscillations of 10 Bq $m^{-3}$ easily occurs and peaks of 70 Bq $m^{-3}$ are reached, producing the variation both in calculated and measured $\dot{H}^*(10)$ values, calculated values show 2 – 4 nSv $h^{-1}$ per 10 Bq $m^{-3}$ although sensitivity of RS is greater. In the INTE-UPC station (section 3.4.3.1) it was not possible to observe these variations since radon progeny concentrations were much lower.

During summer, the RS monitor has an enhanced daily cycle of $\dot{H}^*(10)$, with high values in the night and lower in the day compared to the spectrometric monitors. Significant variation of RS compared with the spectrometric monitor is shown during July 2016. There is a clearly temperature dependence but the analysis of the RS monitor to apply the necessary corrections will be studied in a future.

# 4 Response study of a 1" x 1" $LaBr_3$(Ce) monitor for ground deposited artificial radionuclides

## 4.1 Introduction

In order to carry out the characterization of $LaBr_3$(Ce) monitors, one of the first steps is to study their response in case of fresh ground deposition due to artificial radionuclides. The use of Monte Carlo (MC) codes has the advantage that allows the simulation of any activity concentration for different radionuclides, for several scenarios and any detector size. However, one drawback of MC tool is the time consumption in case of large surfaces and small detectors, i.e., typical situations in superficial contaminations. Therefore, variance reduction techniques are strongly recommended.

In this chapter, with the aim to simulate the fresh radionuclides deposition that would be detected during first hours in a surveillance network in case of a radiological accident, the technique named reciprocal method (Zähringer and Sempau, 1997) is combined with the probability of detection of a 1" x 1" $LaBr_3$(Ce) monitor, in order to obtain, in a reasonable computing time, the gamma spectra that would be measured. Three validations for this methodology have been carried out. First, the photon fluence produced by ground deposition in an infinite surface is compared with previous studies which also use the same variance reduction technique. Then, the response of the detector in a large contaminated surface is simulated with and without variance reduction techniques, in order to compare

the results obtained. Finally, as a qualitative test, experimental spectrum measured with a point source is contrasted with a simulation of a surface contamination, both of them producing the same $\dot{H}^*(10)$. After validation tests, the method is used to study the monitor response in case of a fresh ground deposition of $^{137}$Cs, $^{134}$Cs and $^{131}$I.

## 4.2 Materials and methods

Detector used in this study is the Monitor 1 already explained in Chapter 2, a 1" x 1" $LaBr_3$(Ce) crystal from Saint Gobain Company coupled to a photomultiplier tube model XP2060B. The monitor together with the electronics is protected with an aluminium housing which allows continuous measurement outdoors. The monitor is installed at 1 m height on the roof of the INTE facilities; the surface of the site is about 300 m$^2$.

Detector response ($R$) produced by an incident fluence of particles of energy $E$ ($\Phi(E)$)can be generally described by Equation (4.1).

$$R = P(E)\Phi(E) \tag{4.1}$$

Where $P(E)$ is the probability of detection of the monitor due to an incident particle of energy $E$.

Fluence $\Phi(E)$ reaching the detector will depend on the site geometry, since particles can suffer several scatterings in their path from radioactive source to detector. It can be calculated using MC simulations although a tool of reduction variance will be required in order to reduce computing time. In this work it was used the PENELOPE/penEasy (Sempau et al., 2011) code with the reciprocal transformation as a variance reduction tool. As it is extensively

explained in Zähringer and Sempau, (1997), given a detector ('*D*') and an extended source ('*S*'), it is possible to perform a geometrical equivalence and work in a 'reciprocal system', where a localized source ('*S**)' and an extended detector ('*D**') highly improve the simulation efficiency. Reciprocal transformations can be expressed as:

$$\begin{aligned} V_S(x_S, y_S, z_S) &\rightarrow V_{S^*}(x_D, y_D, z_S) \\ V_D(x_D, y_D, z_D) &\rightarrow V_{D^*}(x_S, y_S, z_D) \end{aligned} \tag{4.2}$$

Where $V_S(\boldsymbol{r})$ and $V_D(\boldsymbol{r})$ are the volumes of the source and the detector respectively, and $V_{S^*}(\boldsymbol{r})$ and $V_{D^*}(\boldsymbol{r})$, are the volumes of the reciprocal source and detector. The use of this technique is not free, there are some symmetrical constraints that should be accomplished. First, source and detector geometries must be defined as a function of *x* and *y* over a *z*-interval. Second, the source strength can be vary only in *z* and finally, the unit response function $a(\boldsymbol{r_1; r_2})$ needs the following symmetry:

$$a(x_1, y_1, z_1; x_2, y_2, z_2) = a(x_2, y_2, z_1; x_1, y_1, z_2) \tag{4.3}$$

These conditions lead to the fact that multilayered planar geometries are required to apply reciprocal transformations, which is the case in the present study.

Actually, with reciprocal transformation, photon fluence ($\Phi(E)$) is calculated in a cylinder of air with the source surface and detector height, named $V_{D^*}$ in the geometry equivalence. PENELOPE uses the *track length estimator* (Salvat et al., 2011) to evaluate the fluence, which provides the mean distance travelled in *D** by a particle belonging to an energy interval [E-ΔE/2, E+ΔE/2], that is, tallied as a function of the energy, and per unit simulated history. Since this *track*

*length* is directly proportional to the fluence, in the following is identified as $\Phi'(E)$[cm $eV^{-1}$].

Probability of detection can be also calculated using MC simulations. As it has been explained in Chapter 3, partial and full absorptions produced in the detector for different energy fluences was evaluated with simulations of monoenergetic parallel beams in steps of 10 keV and in an energy range from 0 to 3000 keV.

In a spectrum scored with *n* energy channels, Equation (4.1) can be detailed and the response of the detector at bin *i* ($R_i$) produced by a certain photon fluence would be described by the following equation.

$$R_i = \Delta E \cdot P(E_{i,j}) \cdot S_P \cdot \frac{\Phi'(E_j)}{V_{D^*}} \tag{4.4}$$

Where the $P(E_{i,j})$ is the probability per gamma of a detection at bin *i* produced by an incident particle of energy $E_j$ emitted from a surface $S_P$ [$cm^2$]; $\Phi'(E_j)$ [cm $eV^{-1}$] is the distance travelled in *D** by a particle with energy *j*; $\Delta E$ [$eV$] is the width of energy band with mean value $E_j$ and $V_{D^*}[cm^3]$ is the volume of *D**. From Equation (4.4) follows that each energy band tallied at $\Phi'(E_j)$ needs a probability of detection.

When a particular radioisotope is considered, the contribution of each γ-ray emission should be taken into account. In a contaminated surface, $S_S$ [$m^2$], with an activity *A* [Bq $cm^{-2}$] deposited on the ground of a certain radionuclide with *k* gamma emissions each one with probability $y_k$, the number of detections at bin *i* ($N_i$) in a time [s] is described by Equation (4.5).

$$N_i = A \cdot S_S \cdot \Delta E \cdot \sum_k \left( y_k \cdot P_k(E_{i,j}) \cdot S_P \cdot \frac{\Phi'_k(E_j)}{V_{D^*}} \right) \tag{4.5}$$

It should be pointed out that the term $S_S$ can be simplified from Equation (4.5), since $S_S = S_{D^*}$ in the reciprocal transformation. In this way there is no surface dependence and Equation (4.5) easily transforms to:

$$N_i = A \cdot \Delta E \cdot \sum_k \left( y_k \cdot P_k(E_{i,j}) \cdot S_P \cdot \frac{\Phi'_k(E_j)}{z_D} \right) \tag{4.6}$$

Where the relation $V_{D^*} = S_{D^*} \cdot z_D$ has been applied.

Calculated $N_i$ provides the *ideal* gamma spectrum since it uses MC simulations to calculate detector response. In order to have a true gamma spectrum, an energy resolution should be considered. The energy resolution (full width at half maximum) applied for this $LaBr_3$(Ce) monitor is $FWHM = 0.81\sqrt{E}$, obtained experimentally using point sources (see section 2.3.5).

In a real measurement, any ground deposition is not isolated from the natural background produced mainly by terrestrial radiation. For this reason, calculated counts in the simulated gamma spectra due to artificial deposited radionuclides were added to a natural background measured with the monitor, which includes, besides terrestrial radioactivity, the typical internal background of $LaBr_3$(Ce) crystals (see section 2.5).

Simulations usually have low uncertainties since the number of counts is very high so, in order to add a typical experimental noise and improve the built spectrum, a Box-Müller transformation is applied in order to sort counts in each channel; mean value is the number of counts and sigma is the square root of this number of counts.

It should be noticed that besides the detector response, with the tallied $\Phi'(E_j)$ also the air kerma rate, $\dot{K}$ [$Gy\ s^{-1}$], produced by a surface activity $A$ [Bq cm$^{-2}$] can be obtained.

$$\dot{K} = A \cdot \Delta E \cdot k \cdot \sum_i \left( y_i \cdot \frac{\mu_{tr}(E_i)}{\rho} \cdot \frac{\Phi'_i(E_j)}{z_D} \right) \tag{4.7}$$

Where $k$ is 1.602·10$^{-16}$ J g eV$^{-1}$ kg$^{-1}$ and $\frac{\mu_{tr}(E_i)}{\rho}$ [cm$^2$ g$^{-1}$] is the mass-energy transfer coefficient, calculated with the program **mutren.f**, from PENELOPE package.

### 4.2.1 Validation of the methodology

To verify the proposed methodology the two steps of the procedure has been considered. Validation of the simulated fluence was carried out through the calculation of the air kerma produced by ground deposition of $^{137}$Cs, $^{134}$Cs and $^{131}$I. And validation of the complete methodology, that is, the calculation of detector response, was carried out by both, comparing with an analog simulation and with an experimental spectrum using a $^{137}$Cs point source.

The air kerma produced by $^{137}$Cs, $^{134}$Cs and $^{131}$I in an infinite surface was calculated at 1 m height using Equation (4.7), the typical detector position in environmental monitoring. It can be noticed that in environmental energy range, the air kerma can be identified with the dose rate. Results obtained are compared on Table 4.2 with values obtained in Zähringer and Sempau, (1997), where also the PENELOPE code was used, and in Namito et al., (2012), where the MC code EGS5 (Hirayama et al., 2005) was used. In all cases, the variance reduction technique based on the reciprocal transformation was applied, but geometrical conditions and materials definition were not identical,

they are summarized on Table 4.1. Statistical uncertainties in Table **4.2** are reported with 2σ. It can be observed that differences are less than 2% in spite of soil differences.

| | **This study** | **Zähringer and Sempau** | **Namito et al.** |
|---|---|---|---|
| Soil composition (relative number of atoms) | 30.5% H, 50.2% O, 5.5% Al, 13.1% Si and 0.7% Fe | 29.2% H, 51.5% O, 4.5% Al, 13.4% Si and 1.4% Fe | 29.4% H, 1.8% C, 50.4% O, 2.7% Al, 13.6% Si, 0.4% K, 1.4% Ca and 0.3% Fe |
| Soil density (g $cm^{-3}$) | 1.27 | 1 | 1.6 |
| Soil thickness (cm) | 150 | 100 | 600 |
| Gamma rays considered (emission ratio) | >1% | >0.01% | (Japan Isotope Association, 2001) |

**Table 4.1.** Conditions employed in MC simulations.

| | **This study** | **Zähringer and Sempau** | **Namito et al.** |
|---|---|---|---|
| $^{137}Cs$ | 2.536 ± 0.004 | 2.572* | 2.58 ± 0.05 |
| $^{134}Cs$ | 6.869 ± 0.008 | 6.939* | 6.94 ± 0.14 |
| $^{131}I$ | 1.711 ± 0.002 | 1.739* | 1.71 ± 0.03 |

*2σ<1.5%

**Table 4.2**. Air kerma rate in pGy $h^{-1}$ at a 1 m height above ground for $^{137}Cs$, $^{134}Cs$ and $^{131}I$. Source strength is 1 Bq $m^{-2}$. The source is deposited on surface (β = 0 g $cm^{-2}$).

Validation of the complete methodology was firstly performed by comparison with an analog simulation. Fig. 4.1 shows spectra produced by a source ground deposited with photon energy 660 keV in a surface with radius 50 m. Black line corresponds to the gamma spectrum simulated with the analog simulation, while red line corresponds to the calculated spectrum using proposed methodology. Blue line shows the photon fluence obtained in the air volume of the crystal detector using the reciprocal method.

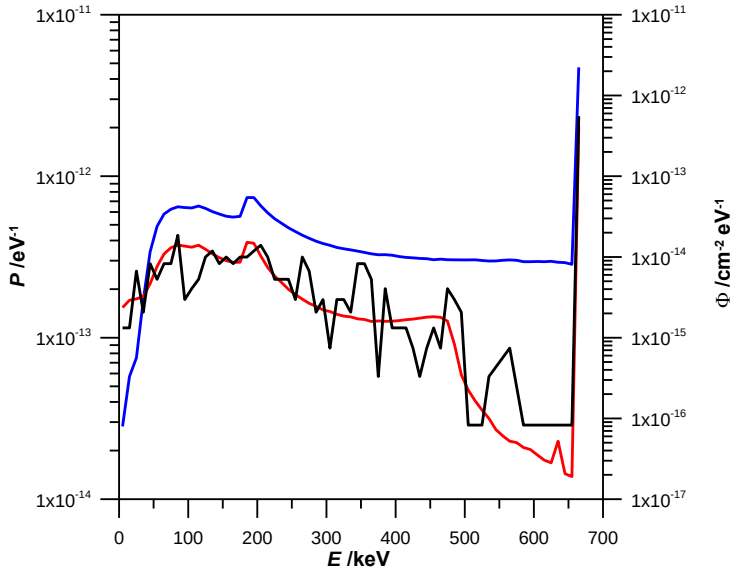


**Fig. 4.1.** Simulated spectrum of ground deposition of a source with photon energy 660 keV with R = 50 m. Black line shows simulation without any variance reduction technique; blue line is the fluence simulated using the reciprocal transformation and, after applying detector response, simulated spectrum is obtained (red line). Energy bin width of 10 keV.

As it could be expected, uncertainties are much larger when no variance reduction technique is used, but it could be seen that both spectra converge to similar shapes. In the simulation with no variance reduction technique detection probability in the full energy peak is $(2.4 \pm 0.5)\cdot 10^{-12}\,eV^{-1}$ with $3.5\cdot 10^{9}$ histories and ~ 2 months of

computing time. On the other hand, analog MC simulation applying reciprocal transformation provides a detection probability of $(2.029 \pm 0.007)\cdot10^{-12}$ $eV^{-1}$ with $3.5\cdot10^{9}$ histories and $\sim 2$ hours of computing time.

Validation of proposed methodology has been also carried out using a $^{137}$Cs point source to check if in case of a low activity deposition, detector response simulated would be similar to a real one produced in the roof of our facilities ($S$ = 300 $m^2$). With this aim, a $^{137}$Cs certified point source from the Amersham Company was located close to the monitor, about 60 cm off the center of the crystal. The activity of the source was 23.7 kBq, which produces a dose rate of $\dot{D} \sim 5$ nGy $h^{-1}$, according to the general Equation (4.8) and disregarding scatterings produced in the air.

$$\dot{D} = k \cdot \frac{A \cdot y \cdot E \cdot (\mu_{en}/\rho)}{4\pi r^2} \tag{4.8}$$

Where $(\mu_{en}/\rho)$ [$cm^2$ $g^{-1}$] is the mass-energy absorption coefficient, 0.02932 $cm^2$ $g^{-1}$ at 661.6 keV, interpolating values from NIST (Hubbell and Seltzer, 1995)) and $r$ [$cm^2$] is the distance of the source to the center of the crystal.

The same ambient dose rate would be produced by 4 kBq $m^{-2}$ of $^{137}$Cs ground deposited in a surface of radius $R$ = 10 m, according to air kerma calibration factors calculated in Zähringer and Sempau (1997) and considering electronic equilibrium. Such surface produces about 15 % of scattered flux.

In Fig. 4.2 the experimental measurement performed with the point source (black line), and the simulated spectra obtained with the aforementioned surface contamination (grey line) is shown. In order

to compare the results with the experimental spectrum, simulated monitor response was added to a common background previously measured in this site (red line). Both spectra, simulated and measured are in agreement. It should be noted in this experiment that uncertainties due the distance of the source to the crystal and also the high background counts, led to this experience to have a significant uncertainty.

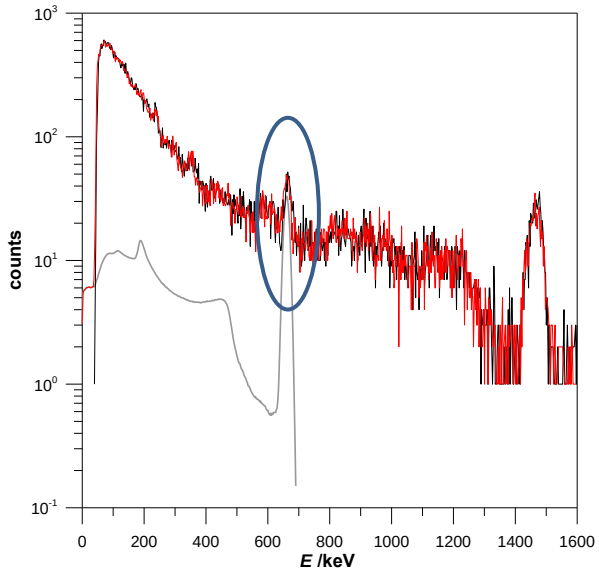


**Fig. 4.2.** Experimental measurement with a $^{137}$Cs point source (black line) compared with simulated $^{137}$Cs ground deposited (red line). Grey line indicates the simulation isolated of 4.2 kBq m$^{-2}$ of $^{137}$Cs, previously to be added to any background. In both cases the ambient dose equivalent rate increase is ~ 6.3 nSv h$^{-1}$. Measurement time $t$ = 900 s.

## 4.3 Results

The possibility to simulate situations with ground deposition, allows us to know the detector response in case of different contaminated scenarios. In this study, 1 kBq m$^{-2}$ of $^{134}$Cs, $^{137}$Cs and $^{131}$I surface ground deposited were simulated. Calculation geometry was a

soil layer of 10 m radius and 150 cm thickness (Fig. 4.3), and an infinite air layer. The soil composition and density is the same as the previously defined in Table 4.1. Considered gamma emissions are listed on Table 4.3; only gamma rays with gamma yield >5% have been considered, knowing that less probable decays hardly would be distinguished from the background.

Selected period for the study was from 3rd to 8th of November 2014 and simulated ground depositions using this methodology were added in two non-consecutive days to the natural background spectra measured with the 1" x 1" $LaBr_3$(Ce) (acquisition time = 10 min). The

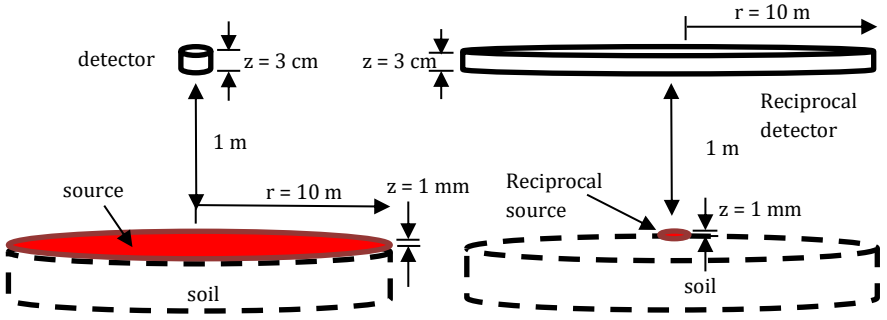


**Fig. 4.3.** Schematic representation of the reciprocal transformation applied in the simulation of the INTE's roof scenario.

| $^{134}$Cs | | $^{137}$Cs | | $^{131}$I | |
|---|---|---|---|---|---|
| **E /keV** | **Yield (%)** | **E /keV** | **Yield (%)** | **E /keV** | **Yield (%)** |
| 563.25 | 8.34 | 661.66 | 85.10 | 284.31 | 6.12 |
| 569.33 | 15.37 | | | 364.49 | 81.5 |
| 604.72 | 97.62 | | | 636.99 | 7.16 |
| 795.86 | 85.46 | | | | |
| 801.95 | 8.69 | | | | |

**Table 4.3.** Gamma-ray emissions considered for each radionuclide.

period of interest includes rainy events in order to observe possible mask effects in the spectra due to wet deposition of radon progeny.

Results obtained are shown in Fig. 4.4. The four graphs correspond the studied period which show in two different days (horizontal red bars) an artificial surface contamination. This contamination was simulated and added to an experimental background as it has been already explained. It includes a) 1 kBq $m^{-2}$ of $^{137}Cs$, b) 1 kBq $m^{-2}$ of $^{134}Cs$, c) 1 kBq $m^{-2}$ of $^{131}I$ and d) 3 kBq $m^{-2}$ from a mixture of the three radionuclides (1 kBq $m^{-2}$ for each radionuclide). Every graph shows two plots. In waterfall plots, gamma spectra are shown sequentially in time and, in bottom plots, time series of $\dot{H}^*(10)$ (black line) together with rainy events are shown. Grey line indicates $\dot{H}^*(10)$ of background measurements. Values of $\dot{H}^*(10)$ have been obtained directly from gamma spectra using the stripping methodology (see section 3.2).

It can be observed that from $\dot{H}^*(10)$ time series, which would be the values provided by a classical dose rate probe, it is difficult to attribute any increase on to the artificial ground contamination. The increase produced by 1 kBq $m^{-2}$ of ground deposition is only about 1.5 nSv $h^{-1}$ for $^{137}Cs$, 3.8 nSv $h^{-1}$ for $^{134}Cs$ and 1 nSv $h^{-1}$ for $^{131}I$. These increases are in good agreement with calibration factors provided by Zähringer and Sempau, (1997) for a soil radius of 10 m, and they are similar to $\dot{H}^*(10)$ peaks produced by rainy events. On the other hand, the increase in the number of counts in waterfall plots can be easily identified at those energies belonging to γ-ray emissions. Beyond the lines belonging to natural γ emissions, like $^{40}K$, an increase in colour intensity is observed in energy regions of $^{137}Cs$ (661.6 keV), $^{134}Cs$ (mainly 604.7 and 795.9 keV) and $^{131}I$ (mainly 364.5 keV).

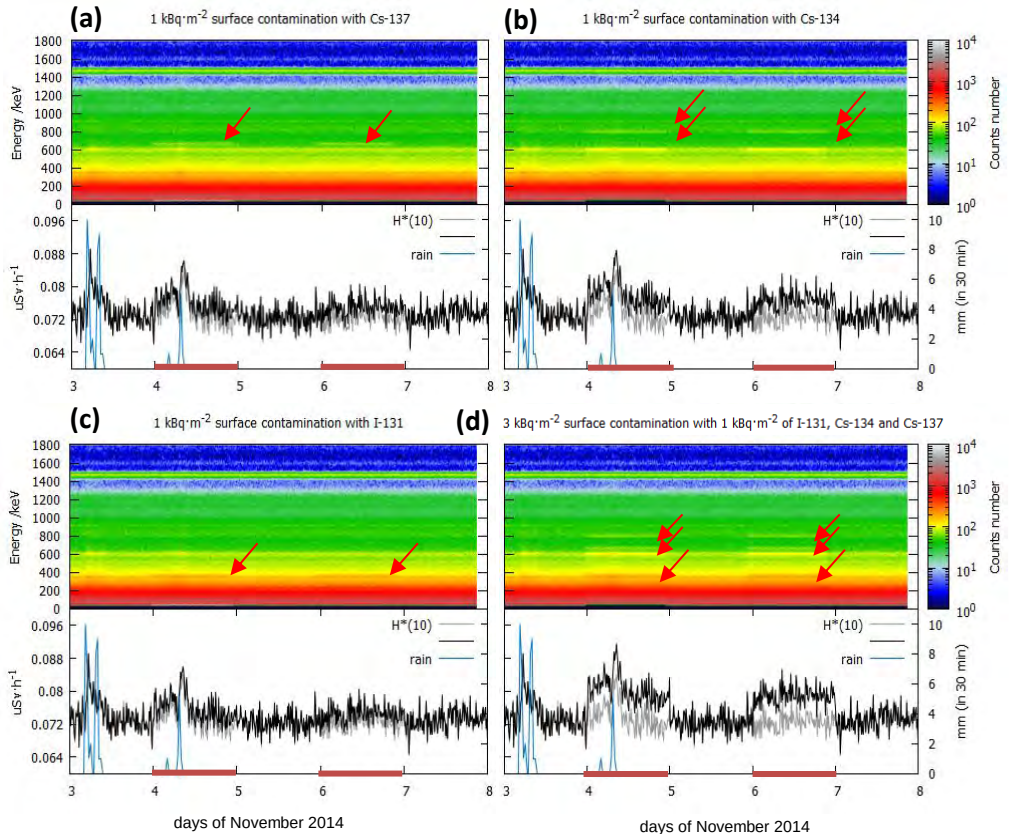


**Fig. 4.4.** Simulated 1 kBq $m^{-2}$ superficial contamination of $^{137}Cs$ (a), $^{134}Cs$ (b), $^{131}I$ (c) and a mixture of the three radionuclides (d) added to 10-min series of measured background. Red lines indicate contaminated periods and red arrows point energies of simulated gamma rays in each radionuclide.

As it was expected, meteorological conditions could produce mask effects on the analysis of $\dot{H}^*(10)$ and waterfall plots. Ambient dose equivalent rate during the strongest rainy event suffer an increase close to 10 nSv $h^{-1}$, much greater than any one produced by 1 kBq $m^{-2}$ of surface contamination. Colour rise produced by 604.7 keV and 364.5 keV γ-rays is not much more greater than ones produced by natural $^{214}Bi$ (609.3 keV) and $^{214}Pb$ (351.9 keV) during strong rainy events. However in these situations, γ-ray energies isolated from natural ones are helpful to detect artificial radionuclide presences.

For radionuclides studied in this work, $^{137}$Cs is easily identified on any occasion, $^{134}$Cs, in case of strong rain, can be identified by its 795.9 keV gamma ray, and $^{131}$I could be masked by rain if the ground deposition has a low activity, because its main γ-ray (364.5 keV) has an energy close to one from $^{214}$Pb (351.9 keV). For $^{131}$I, larger activities than 1 kBq m$^{-2}$ would be needed to be easily identified.

In case of a mixture of radionuclides ($^{137}$Cs+$^{134}$Cs+$^{131}$I), the increase can be observed in both, number of counts and $\dot{H}^*(10)$, since the total contamination is 3 kBq m$^{-2}$.

## 4.4 Conclusions

The study of detector response in case of radionuclides ground deposited is one of the critical points to decide the suitability of a novel spectrometric monitor in a certain surveillance network. In this work, a methodology based on MC simulations using the reciprocal method as a variance reduction technique, has been developed and applied to calculate gamma spectra in case of surface contamination in a reasonable computing time.

The procedure has been applied to a 1"x1" $LaBr_3$(Ce) monitor and three validations have been performed. First of all, a comparison with previous studies of the air kerma produced for an homogeneous and isotropic surface source of $^{137}$Cs, $^{134}$Cs and $^{131}$I. After that, the complete methodology has been validated through a comparison with an analog simulation and with the measured spectrum of a $^{137}$Cs point source, which provided the same $H^*(10)$ as 4kBq m$^{-2}$ of $^{137}$Cs ground deposition. In all cases a good agreement was obtained.

Furthermore, this method has been applied to study the sensibility of the detector for $^{137}$Cs, $^{134}$Cs and $^{131}$I ground deposition. Results

obtained show that, visually, the contamination produced by 1 kBq $m^{-2}$ of these radionuclides can be distinguished from the background, but would not be detected by a classical bulk dose rate monitor currently installed in the national surveillance networks. Therefore, it is advisable to the national authorities to develop a plan in order to install spectrometric monitors in these networks.

# 5 Measurements with Remote Pilots Aircraft Systems

## 5.1 Introduction

Emergency situations with accidental releases of radiological contaminants, such as the last accident in the Fukushima power plant, reveal the need to perform measurements and obtain instantly information trying to minimize human exposures to radiation.

Unmanned aerial vehicles (UAV's), commonly known as drones, are nowadays being implemented in several aspects of our lives; they have applications on search and rescue, inspections of powerlines and pipelines, aerial photography, science research, etc. Their application in radiation surveillance has obvious benefits; they could be used for wide-area measurements avoiding the exposure of the crew, as it may happen in a common helicopter or airplane. In this sense, different studies and projects have started being developed: designs for sampling and measure radioactive particles in flight and remote sensing systems for radiation detection and aerial imaging (Kurvinen et al., 2005; MacFarlane et al., 2014; Pöllänen et al., 2009; Sanada and Torii, 2015; Towler et al., 2012).

In this project, also with the aim to provide improvements in the knowledge of the radiological situation in case of an accident and hence support decisions to authorities, a prototype of drone which uses a 3" x 3" NaI installed in an RPAS helicopter (Remotely Piloted Aircraft Systems) has been developed. The project has been possible thanks to the cooperation with the ICARUS group from the UPC

(https://www.icarus.upc.edu/en) and at the present time, is still in an initial stage although preliminary results obtained are promising. In this chapter there is described the set-up developed and first measurements of radioactivity performed with a RPAS carrying a NaI 3" x 3" monitor.

## 5.2 Instruments and methods

The vehicle used in this project is a RPAS helicopter model Benzin Acrobatic from the Vario Helicopter company (http://www.vario-helicopter.net). The RPAS dimensions are 695 x 2121 x 620 mm and it has a dry weight of 9.3 kg with a tank capacity of 0.59 l for a mixture of petrol and engine oil. The autonomy of the engine is about 20 minutes with a payload ~ 10 kg. RPAS is remotely piloted with a radio control system and a professional pilot is required.

Detector installed was a 3"x3" scintillator crystal type NaI(Tl) coupled to the Multi Channel Analyzer (MCA) Canberra uniSpec, from Canberra Industries (http://www.canberra.com/). The software required for uniSpec MCA is GENIE2000 (Canberra Industries), which works together with an application named GammaSpec (Caballero Folch, 2008); this application allows GENIE200 the continuous spectra acquisition and analysis. The monitor is powered through the same USB cable used to transfer data from the MCA to the computer. The computer used for this prototype to connect with the monitor was the mobile PC HTC Shift, which supports Windows, the required environment for GENIE2000. The boot of this mobile PC was modified to start the operative system from a pendrive, in order to solve the problems generated by helicopter vibrations on the hard disk drive. Data transmission system is described on Fig. 5.1. The on board

computer, HTC Shift, connects with the computer of the land team through an ad-hoc network created from land. Then, the ground control team can see and control HTC shift through a remote desktop. This kind of connection had a range about 50 m, which was enough to test the prototype.

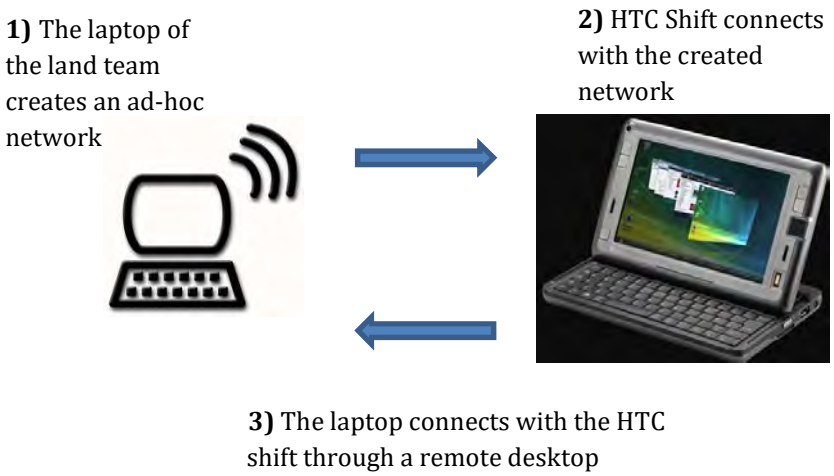


**Fig. 5.1.** Scheme of the data transmission system based on the direct link between the computer of the land team and the on board computer.

The detector and its electronics, including the HTC Shift, supposes a payload of 3.5 kg and it was installed in the bottom of the helicopter, between the landing skids, as it can be observed in Fig. 5.2, both for allow the landing of the helicopter and for balance the weight of the complete set-up. The holding system to the helicopter basis has silent blocks to isolate, partly, vibrations produced by the vehicle.

The RPAS helicopter has a telemetry system; however, the weight of the monitor did not allow its use. Instead, a smartphone was located in the front of the helicopter, as it can be observed in Fig. 5.3. The GPS of the smartphone provides position and altitude values.

**Fig. 5.2.** View of the RPAS helicopter during a flight. On the right side there is a zoom of the space between landing skids, where is allocated the detector and the computer.

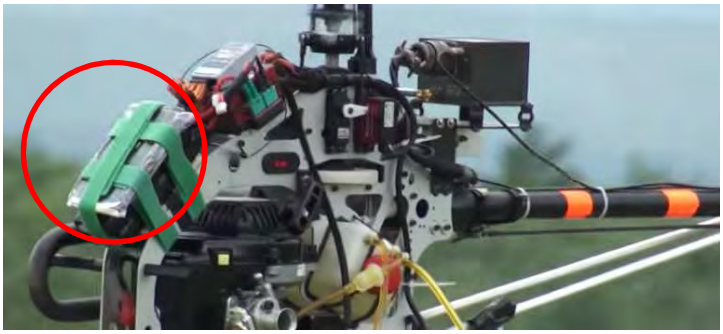

**Fig. 5.3.** Position of the smartphone in the helicopter front.

### 5.2.1 NaI Calibration

The 3" x 3" NaI(Tl) monitor was characterized using certified point sources from the Amersham Company. It was determined its FWHM and the linearity of its response.

The FWHM of this detector was calculated with $^{133}$Ba, $^{137}$Cs and $^{60}$Co point sources. Results are shown in Fig. 5.4. Dotted line shows

the fit obtained using Equation (5.1) (Gilmore, 2008). Parameters obtained are $a$ = 0.0078 and $b$ = 1.8168.

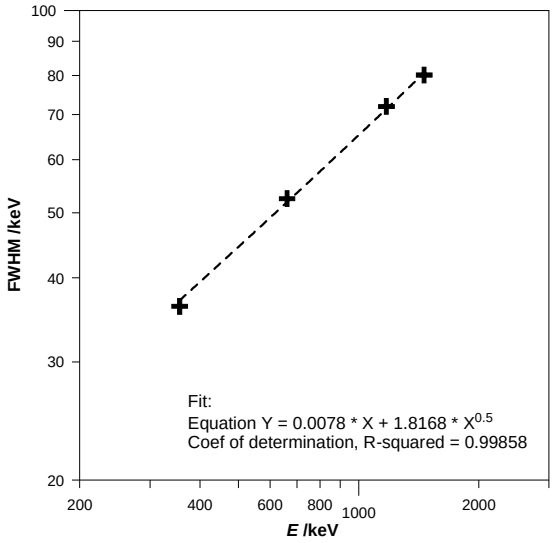


**Fig. 5.4.** Measured FWHM for the NaI(Tl) monitor using $^{133}$Ba, $^{137}$Cs and $^{60}$Co point sources. Dotted line shows the best fit achieved.

$$FWHM = aE + b\sqrt{E} \tag{5.1}$$

The linearity of the NaI(Tl) detector was studied with the same point sources; Fig. 5.5 shows the plot of full-energy peak energies against the channel number of the centroid of the peaks. The goodness of the fit is evaluated with the coefficient of determination $R^2$, and results show that a linear energy calibration is a good approximation.

The estimation of the NaI(Tl) response was performed with a $^{137}$Cs source, certified activity 39.6 kBq (01/02/1993), and with an acquisition time of 10 s, the same acquisition time to be set on flight measurements. The point source was located at different distances (20, 30, 40 cm), in order to produce different dose rates. Results are

shown on Fig. 5.6 with calculated linear fit. According to the fit, in a 10 s measurement, detector signal is 23,768.84 counts $\mu Sv^{-1}$ h for $^{137}Cs$ source.

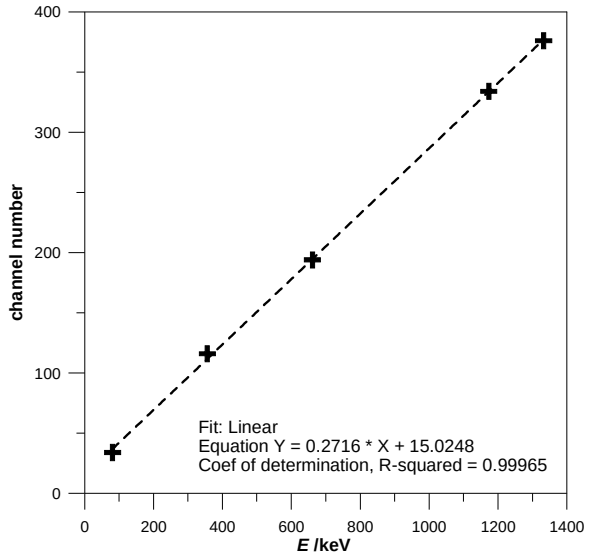


**Fig. 5.5.** Centroid channel vs. photon energy obtained for NaI(Tl) monitor using $^{133}Ba$, $^{137}Cs$ and $^{60}Co$ point sources.

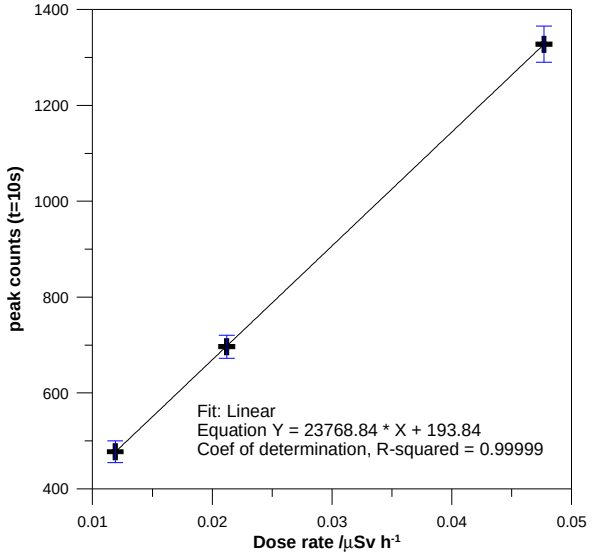


**Fig. 5.6.** Counts in the $^{137}Cs$ peak at different dose rates.

## 5.3 Results of the flight

The measurement site selected for tests flights was Barcelona Drone Center test site (http://www.barcelonadronecenter.com). BDC is a private company dedicated to Earth observation using UAV's, which has its own segregated airspace (TSA), approved by Spanish airspace authorities. It has an extension of 25 $km^2$ and a maximum ceiling of 1200 m. The facilities are located in Collsuspina, ~70 km from Barcelona (41º 48' 16.72" N, 2º 09' 27.62" E).

Two scenarios were selected, as it is shown in Fig. 5.7, one over land and another one over a pond; with the goal to observe the


**Fig. 5.7.** Location of the two measurement sites. Path travelled over the field is indicated with a red line, and over the pond, with a blue line.

sensitivity of the assembly. Over both scenarios the helicopter travelled a path with different altitudes and at certain ones, the pilot stopped the engine in order to take several spectra. The data acquisition time was 10 s and the time spent each time by the software to save and start a spectrum was about ~2 s.

### 5.3.1 Flight over the field

Results of the measurements over land are shown in the graph of Fig. 5.8. The graph shows two plots. In the waterfall plot, spectra are shown sequentially in time and, in the bottom plot, there are plotted the altitudes a.s.l. for each time. It can be observed that from second 700th, until second ~850th, when the highest altitude is reached, there is a dark region which reveals a decrease in the number of counts. The reason is that background counts are mainly due to terrestrial radiation, therefore the count rate decreases with height.

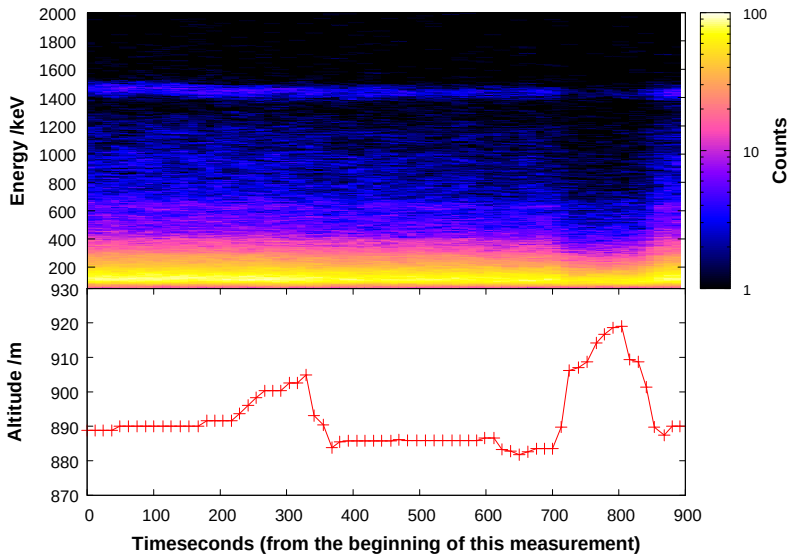


**Fig. 5.8.** Waterfall plot obtained in the flight over the field at different altitudes.

Averages of measured counts in the peak region of $^{137}Cs$ at different altitudes are listed in Table 5.1. Results show the limit detection ($L_D$, see Appendix 1) at different altitudes with an acquisition time of 10 s. According to the slope obtained in the previous section (5.2.1), 23,768.84 counts per $\mu Sv^{-1}$ h, and the calculated $L_D$, the system may be able to detect increases in the dose rate >2.55 nSv $h^{-1}$ at 0-10 m altitudes, and >2.03 nSv $h^{-1}$ at 15-25 m.

| Altitude /m | <Counts> /t=10 s | σ /t=10 s | $L_D$ /t=10 s |
|---|---|---|---|
| 0 | 133.4 | 11.6 | 69.4 |
| 5-10 | 100.0 | 10.0 | 60.6 |
| 15-25 | 61.4 | 7.8 | 48.3 |

**Table 5.1.** Background counts measured at the $^{137}Cs$ peak region as a function of the altitude with the 3" x 3" NaI(Tl) monitor. Second column represents the mean number of counts with acquisition time 10 s, third column is the standard deviation ($\boldsymbol{\sigma = \sqrt{\langle Counts \rangle}}$) and fourth column is the limit of detection calculated with *k*=2.

## 5.3.2 Flight over the pond

Second measurement over the pond is shown in the graph of Fig. 5.9, with the same types of plots previously used. In this flight, measurements were performed over the pond and the shoreline at different altitudes; Fig. 5.10 shows the position of the helicopter at different times. It can be observed from both figures that dark regions are not related with large heights but with flights over the water. Reason is that terrestrial radiation is mitigated by water and hence, count rates are lower over the pond surface. On the other hand, at higher altitudes over the pond, terrestrial radiation from the shorelines is able to reach the detector and count rates are greater than just over the water surface.

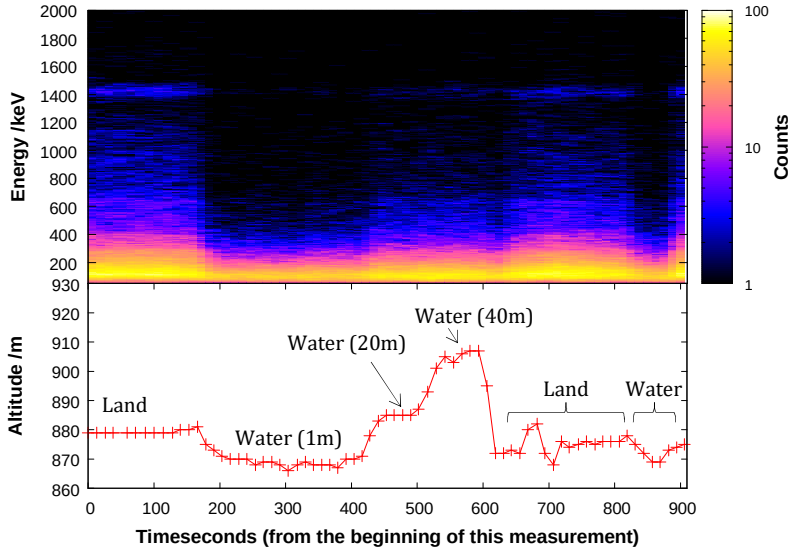


**Fig. 5.9.** Waterfall plot obtained in the flight over the pond and shoreline at different altitudes. Labels indicate helicopter position and approximate altitude.

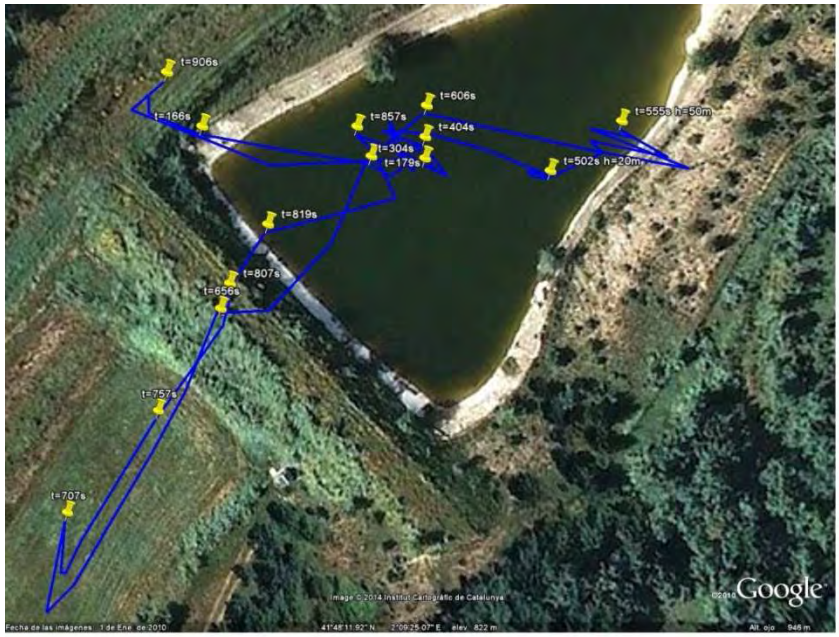


**Fig. 5.10.** Path travelled by the helicopter over the pond and the shoreline detailed for different times.

## 5.4 Conclusions

In this chapter it has been shown results obtained with a 3" x 3" NaI(Tl) detector installed in a RPAS. Although it was still a prototype, it demonstrated its sensibility to terrestrial dose rate variations and the possibility to clearly stablish a correlation between data received and path followed. In waterfall plots (Fig. 5.8 and Fig. 5.9) it can be distinguished flights at different altitudes and flights over land and over water, what its more, flights over water at certain altitude show an increase in the dose rate due to lateral contribution of shore.

Provided that results obtained with this prototype were successful, a new prototype has been developed. The HTC Shift has been replaced by the minicomputer Intel NUC DN2820FYKH with solid state hard drive, to avoid problems with helicopter vibrations, and the ad-hoc network has been replaced by a 3G connection with static IP to establish a bridge between the computer on land and the computer on board. Although this new prototype has not been tested yet, larger ranges for data transmission are expected.

# 6 Conclusions

## 6.1 Summary

In this thesis the use of novel $LaBr_3$(Ce) scintillation detectors applied to environmental monitoring has been studied. Currently, due to technical and economic reasons, surveillance networks are equipped with dose rate monitors which provide continuous information about dose rate levels while they do not provide data on gamma spectrometry. Development of new detection materials enables the possibility to use spectrometric measuring equipment, as has already been done in Finland, which has installed $LaBr_3$(Ce) detectors at some of the monitoring stations located close to nuclear power plants.

Two sizes of $LaBr_3$(Ce) were available for the study, two 1" x 1" crystals and one 1.5" x 1.5". Chapter 2 gives information on their characterization by means of several irradiations that were performed in the Calibration and Dosimetry Laboratory at our institute. The study of angular response shows an almost isotropic response of crystals, only attenuated by electronics on the back of the detector, while the energy resolution obtained was ~ 3% at 662 keV, according to the manufacturer's specifications. Energy and dose rate response show linearity, though both detector sizes start to show saturation above 1 mSv $h^{-1}$. This makes it recommendable to install both spectrometric monitors and "traditional" dose rate probes in surveillance stations which might possibly detect high dose rate values. This would be the case in stations that are located close to

nuclear power plants to prevent saturation in the case of radiological accident.

The main drawback commonly for these detectors is their inherent contamination due to $^{138}$La and $^{227}$Ac. In this thesis the internal background was experimentally measured both in lakes and at the UDO II lab, clearly showing self-counting measured spectra. In Fig. 6.1 both measurements are plotted for Monitor 1 and 2, and only differences at low energies are observed due to the cosmic radiation contribution at lakes.

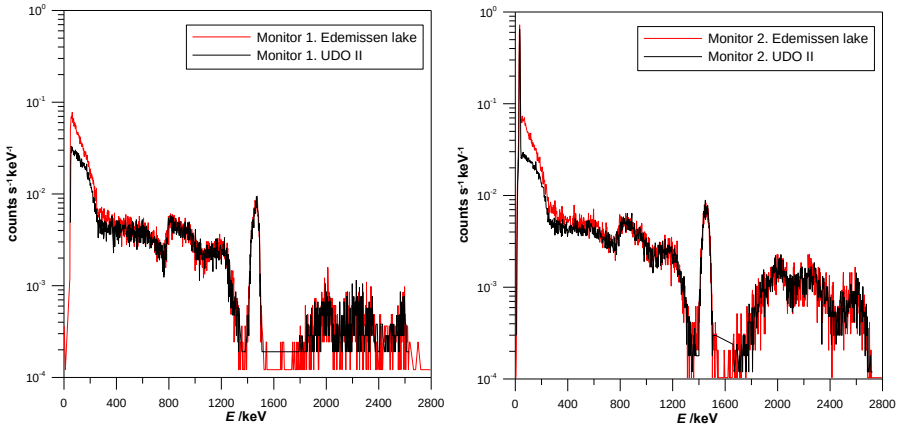


**Fig. 6.1.** Comparison of self-counting measurements performed at Edemissen lake and in the lead castle at UDO II with Monitor 1 and 2.

In spite of the goodness of results obtained in these experimental measurements, both indicate that internal background cannot be easily determined in all labs since special conditions for its determination are required. A new system has therefore been proposed to determine inherent counts produced by $^{138}$La both based on Monte Carlo simulations and experimental measurements available in a common radioactive laboratory. A modification of the PENELOPE/penEasy code was applied in order to simulate cascade effects and typical branches of $^{138}$La decay. The procedure shows

similar results to self-counting measurements obtained experimentally and offers an alternative within the reach of most laboratories.

The correct definition of this internal background is important in order not to overestimate the number of detected counts and hence, calculated $H^*(10)$. However, from the viewpoint of $H^*(10)$, it adds a constant value and therefore variations would be equally evaluated. In addition, the presence of this internal background can be considered a benefit. The constant 1435.8 keV peak, is useful to calibrate spectra and easily detect possible variations in energy bin width.

Installation of these monitors in surveillance networks led to the need to validate methodologies to obtain dose rate values from measured spectra. In this way, we will thus have information on dose rate values together with radionuclide identification. Chapter 3 provides two different methodologies, the *stripping* method and the *conversion coefficients* method. The first is based on obtaining the external flux that reaches the monitor and involves the subtraction of all partial absorptions produced by scatterings in the monitor itself. This methodology, which has been already studied and usually applied to HPGe detectors (Clouvas et al., 1998; Miller, 1984), proved that it can also offer good results in $LaBr_3(Ce)$ detectors. The second methodology is based on splitting the spectra into several energy regions (Grasty et al., 2001; Yi et al., 1997), and a coefficient to "convert" from measured counts to $\dot{H}^*(10)$ values for each region is defined.

The methodologies mentioned above were applied to several measurements. Monitor 1 was installed on the roof of our institute in

Barcelona for several months performing continuous measurements, $\dot{H}^*(10)$ was calculated from registered spectra and compared with values reported by a proportional counter from the Bitt Company belonging to the IRSN installed at the same measuring site. Results show a similar sensitivity between measured and calculated $\dot{H}^*(10)$ values and variations of a few nSv $h^{-1}$ are detected. Although values calculated with conversion coefficients are lower than those calculated with the stripping method to a constant value ~8 nSv $h^{-1}$ (for an energy range up to 3000 keV), both methods show similar patterns and are able to see the effects of meteorological variables. As shown in Fig. 6.2 and detailed in Chapter 3, rain causes radon wash-out, which produces radon progeny deposition onto the ground. The effects of such a deposition are peaks in $\dot{H}^*(10)$ of around 14 nSv $h^{-1}$ during a usual rainy event of 6-8 mm. In addition, atmospheric pressure influences cosmic radiation that reaches the earth's surface and therefore periods with high values of atmospheric pressure are related to lower values of $\dot{H}^*(10)$. In any case it may be considered that cosmic radiation only produces counts in the low energy region, as is shown in Fig. 6.1, and its contribution to total $\dot{H}^*(10)$ is less than 10 nSv h-1.

Apart from the effects of rain, the consequences of $^{222}Rn$ air concentration variations have been studied on $\dot{H}^*(10)$. Radon suffers both daily and seasonal fluctuations due to changes in the height of the atmospheric boundary layer. At the Barcelona station these oscillations of daily radon concentration are not too large and no effects were registered by the $LaBr_3(Ce)$ detectors. On the other hand, measurements carried out at the Esmeralda station (Madrid), within the framework of the European MetroERM project, show daily oscillations which easily reach more than 10 Bq $m^{-3}$, and the effects on

$\dot{H}^*(10)$ can be observed in calculated values from the $LaBr_3(Ce)$ spectra; a range between 0.2-0.4 nSv $h^{-1}$ per 10 Bq $m^{-3}$ has been estimated.

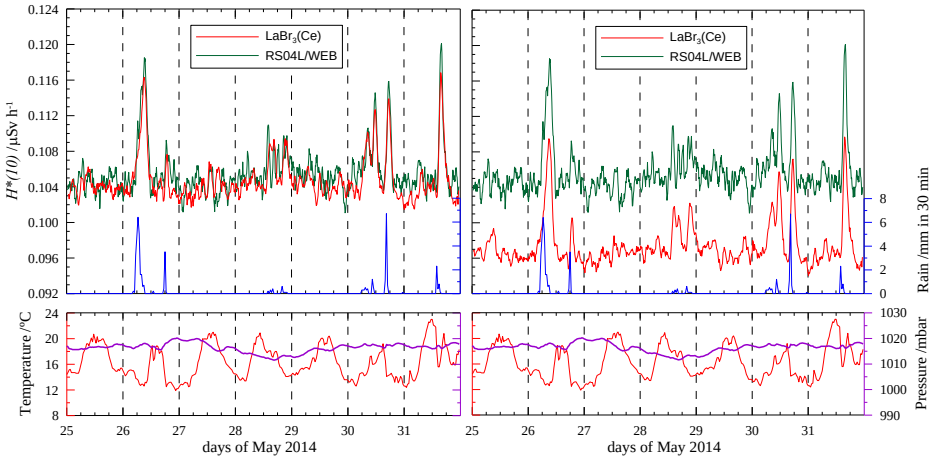


**Fig. 6.2.** Running average of the $\dot{H}^*(10)$ values obtained with the stripping method (*left side*) and conversion coefficients (*right side*) compared with ones provided by the monitor RS04L/WEB. Both plots refer to the last week of May 2014 and show meteorological values (pressure, temperature and rain).

Another series of measurements were performed at PTB also within the framework of the MetroERM project. The campaign was an intercomparison among several research groups and our group took part using Monitor 1 and 2. There were three different scenarios, a lake, the UDO II lab and an open field away from the influence of buildings or trees. Again, measurements show that values calculated with the conversion coefficients are lower than those obtained with stripping, but relative differences with reference values are ~10% in all cases. The study in the open field comprised a simulation of a radioactive plume in addition to point source exposures. Results obtained show that continuous measurements by both $LaBr_3(Ce)$

monitors were able to follow $\dot{H}^*(10)$ values which ranged from 10 to 180 nSv $h^{-1}$ with enough sensitivity to see increments of 10 nSv $h^{-1}$.

In the case of a radioactive emergency, first time data is essential in order to take decisions. If $LaBr_3(Ce)$ detectors are going to be used in surveillance networks, their response will need to be known. In addition to calculating $\dot{H}^*(10)$ from measured spectra, the study of detector response in terms of radionuclide identification was examined in Chapter 4. The analysis was performed by using Monte Carlo simulation of fresh ground deposition of artificial radionuclides. Large contaminated areas were considered so the use of variance reduction techniques was required in order to work with reasonable computing times. Results obtained show that contamination produced by 1 kBq $m^{-2}$ of $^{137}Cs$, $^{134}Cs$ and $^{131}I$ could be directly distinguished from the background in 10 min spectra with a visual search. Radionuclide identification enables atypical situations to be distinguished, which might go unnoticed if readings only in terms of $\dot{H}^*(10)$ were used. This fulfils recommendations of German legislation which requires for a spectrometric monitor the sensitivity to detect a homogeneous surface contamination of 1 kBq $m^{-2}$ of $^{137}Cs$ within 30 min.

There are some circumstances in which in-situ measurements are required because there is no possibility of connecting with surveillance networks or because more measuring points are required. As a recent example, there is the Fukushima accident (2011). In these circumstances it is very dangerous for people to carry out any measurements in the affected area. One aim of this thesis has been to study the use of new technologies to help in these emergency situations.

As detailed in Chapter 5, a drone prototype has been developed which uses a 3" x 3" NaI installed in an RPAS helicopter. The first flights took place at different altitudes and over a pond in order to study detector sensitivity. Although the prototype it is still at an initial stage and more flights are required, preliminary results obtained are promising, showing that the system is able to detect variations in terrestrial radioactivity.

## 6.2 Outlook and future steps

The possibility of installing gamma ray spectrometry detectors in radiation monitoring stations is being studied by several countries and projects. Within the framework of MetroERM, different detector types have been studied: CdZnTe, $CeBr_3$, $SrI_2$,… with the aim of determining more reliable monitors in terms of nuclide identification and low technical intervention. Results obtained in this thesis show that $LaBr_3$(Ce) are good candidates since they offer good results in terms of resolution, energy linearity and efficiency. In addition, dose rate values can be calculated from measured gamma spectra.

Therefore, as a conclusion of this work, it is advisable for the regulatory authorities to develop a plan to install gamma ray spectrometry monitors at early warning stations to gradually substitute "classical" dose rate monitors or to run in parallel with them.

However, besides the clear advantages of installing these monitors in monitoring surveillance networks, the amount of data that should be registered and analysed will increase significantly and so the development of standardized tools to automat processes will be needed. This means the development of European data bases will be

required to manage all this information. Furthermore, definition of alarms using spectrometry monitors should be harmonized.

If $\dot{H}^*(10)$ is calculated from measured gamma spectra, another issue related to harmonization that should be pointed out is that spectrometry detectors are almost transparent to cosmic radiation compared with dose rate monitors. For the general public this could be interpreted as a fall in $\dot{H}^*(10)$. Nothing could be further from the truth, so installation of these detectors must be done together with a communication plan to stablish a parallelism between $\dot{H}^*(10)$ obtained from dose rate monitors and calculated from registered gamma spectra.

To follow a nuclear or radiological event, fast and appropriate radiation protection measures based on reliable radiological data are a high priority for decision makers. In the case of widespread ground contamination, monitoring with unmanned aerial vehicles equipped with gamma ray spectrometry detectors is a solution to protect operators against contamination or irradiation. This means careful calibration since the detector will be in motion and surrounded by electronics. Advanced methods based on reference materials and standard radionuclide sources will be required, and the use of Monte Carlo simulations will be helpful. The European project "Metrology for mobile detection of ionising radiation following a nuclear or radiological incident" (Preparedness) will start. One of the main aims is to develop unmanned aerial detection systems installed on aerial vehicles for the remote measurement of dose rates and radioactivity concentrations.

# Appendix 1. Statistics.

*Definitions and figures used in this appendix are based on (Gilmore, 2008).*

All events related with radioactive decays have an statistical nature. The reason is that the law of radioactive decay (see Equation (A1.1)) describes the behaviour of a source formed by several atoms ($N_0$) according to its decay constant ($\lambda$), but does not predict the decay of an individual atom. Therefore, we are only able to say that after a certain time $\Delta t$, the number of not decayed nuclei will be $N$.

$$N = N_0 e^{-\lambda \Delta t} \tag{A1.1}$$

As a consequence, we can say that a single particle will decay with a certain probability $p$:

$$p = (1 - e^{-\lambda \Delta t}) \tag{A1.2}$$

The decay of each atom is statistically described by a binomial distribution, maybe the particle decay or maybe not. The probability of getting $n$ decays in a sample with $N$ atoms is described by the probability mass function:

$$P(n) = \frac{N!}{(N-n)!\,n!} p^n (1-p)^{N-n} \tag{A1.3}$$

The expected value and the variance in a binomial distribution are given by Equation (A1.4) and (A1.5), respectively.

$$E(n) = pN \tag{A1.4}$$

$$var(n) = (1-p)pN \tag{A1.5}$$

Most practical situations can be described by $N \to \infty$ and $p \to 0$, since the number of atoms in a source could be huge and probability of detection used to be low. Then, the binomial distribution can be approximated to a Poisson distribution.

$$P(n) = \frac{[E(n)]^n}{n!} e^{-E(n)} \tag{A1.6}$$

Moreover, applying $p \to 0$ to Equation (A1.5), we can say *E(n) = var(n).*

When the expected value ($pN$) is high, due to central limit theorem, the Poisson distribution can be approximated to a Normal distribution. In case of low number of expected counts this approximation will not be possible and the Poisson distribution must be used.

$$P(n) = \frac{1}{\sqrt{2\pi E(n)}} exp\left\{\frac{-(n-E(n))^2}{2E(n)}\right\} \tag{A1.7}$$

Detectors used in all these measurements have a certain efficiency of detection $\varepsilon$, that is, not all decays will be registered. The expected value previously defined is $E(C) = p\varepsilon N$, where $C$ are the measured counts. When several measurements are performed, the expected value corresponds to an average value of all measurements. But commonly, there is only a single measurement. In this situation, the measurement can be considered a sample of a population whose distribution function is a Poisson or Gaussian. In these circumstances,

the expected value, and also the variance, can be identified with measured counts:

$$E(C) = var(C) = C \tag{A1.8}$$

In a measurement always there is certain number of counts due to background, commonly produced by interaction of other gamma-rays with the detector. This background ($B$) should be subtracted in order to know the net counts ($N$) actually detected $N = C - B$. Since there is no correlation between measurements the uncertainty is:

$$var(N) = var(C) + var(B) = N + B + var(B) \tag{A1.9}$$

And for $N = 0$:

$$var(N = 0) = B + var(B) = 2B \tag{A1.10}$$

Because of the uncertainty associated to measurements, sometimes the decision whether a count is a true measurement or is due to background is not clear. Some concepts are defined to help in these counting decisions.

- Critical limit ($L_C$). The limit above which we can be confident to say, in a certain degree $\alpha$, that a net count is statistically significant and does not belong to background. Considering a mean value $N = 0$ with standard deviation of $\sigma_0$, the critical limit is stablished at $k_\alpha \sigma_0$, where $k_\alpha$ is the coverage factor (Fig. A1. 1). It is defined by Equation (A1.11).

  $$L_C = k_\alpha \sigma_0 \tag{A1.11}$$

  Equation (A1.11) can be redefined applying Equation (A1.10):

$$L_C = k_\alpha \sigma_0 = k_\alpha \sqrt{(B + var(B))} = k_\alpha \sqrt{2B} \quad \text{(A1.12)}$$

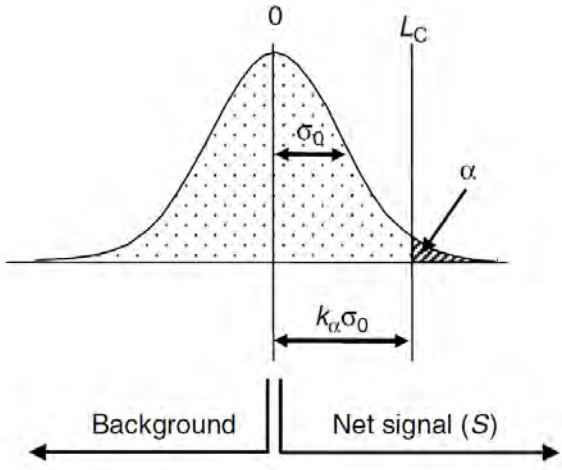


**Fig. A1. 1.** Definition of critical limit (vertical axis represents the frequency of observing a particular count).

Table A1. 1 shows the value of $k_\alpha$ related with each degree of confidence. One-tailed columns are considered because we are interested in values exceeding the higher side of the distribution. Only with probability $\alpha$ a count would be considered true when it was not.

- Upper limit ($L_U$). It is the maximum statistically reasonable that could be stablished for a measured number of net counts ($N$). For any distribution of counts, we can say with a certain confidence level (associated $k_\alpha$ factor), that t rue activity is lower or equal to $L_U$. If $N = 0$, then $L_U = L_C$.

$$L_U = N + k_\alpha \sigma_N = N + k_\alpha \sqrt{N + 2B} \quad \text{(A1.13)}$$

| *Probability interval, a* | *1-tailed confidence* | *2-tailed confidence* | *ka factor* |
|---|---|---|---|
| 0.1587 | 84.13 | 68.27 | 1.0 |
| 0.1 | 90.00 | 80.00 | 1.282 |
| 0.05 | 95.00 | 90.00 | 1.645 |
| 0.025 | 97.50 | 95.00 | 1.96 |
| 0.02275 | 97.73 | 95.45 | 2.00 |
| 0.01 | 99.00 | 98.00 | 2.326 |
| 0.00621 | 99.38 | 98.75 | 2.5 |
| 0.005 | 99.50 | 99.00 | 2.576 |
| 0.00135 | 99.87 | 99.73 | 3.0 |

**Table A1. 1.** $k_\alpha$ factors for particular probability intervals and the associated degrees of confidence.

- Detection limit ($L_D$). It is the number of counts which we can be confident to detect. Unlike the $L_C$ we do not want to avoid false positives, we want to avoid false negatives.

  Because of Gaussian distribution of measured counts, detected counts above $L_C$, statistically will be below this value in certain occasions. For example, if detected counts are exactly $N = L_C$, in 50% counts they will fall below $L_C$. With detection limit we wish to be certain with a certain degree (associated to $k_\beta$ factor) that the chance of not detecting when it is really there is $\beta$. This is expressed by Equation (A1.14) where $\sigma_D$ is the standard deviation of detected counts.

$$L_D = L_C + k_\beta \sigma_D = k_\alpha \sigma_0 + k_\beta \sigma_D \qquad \text{(A1.14)}$$

When $N = L_D$, then we can say at the detection limit:

$$N = C - B \rightarrow \sigma_D^2 = C + B$$

$$C = L_D + B \qquad \text{(A1.15)}$$

$$\sigma_D^2 = L_D + \sigma_0^2$$

And Equation (A1.14) can be redefined as:

$$L_D = {k_\alpha}^2 + 2k_\alpha\sigma_0 \qquad \text{(A1.16)}$$

In case of low number of counts (<25), when the Normal approximation is not possible

$$P(n) = \frac{(B)^n}{n!}e^{-B} \qquad \text{(A1.17)}$$

# Appendix 2. Box – Müller transformation.

The Box-Müller transformation is a method to generate normal distributed random numbers from uniformly distributed random numbers.

Equation (A2. 1) defines the normal distribution:

$$f(x) = \frac{1}{\sqrt{2\pi}} e^{-x^2/2} \tag{A2. 1}$$

If $x_1$ and $x_2$ are two independent random variables, the probability density function is defined as:

$$f(x_1, x_2) = \frac{1}{\sqrt{2\pi}} e^{-{x_1}^2/2} \cdot \frac{1}{\sqrt{2\pi}} e^{-{x_2}^2/2} = \frac{1}{2\pi} e^{-({x_1}^2+{x_2}^2)/2} \tag{A2. 2}$$

Since this function is radially symmetric, it can be expressed in polar coordinates $x_1 = rcos\phi$ and $x_2 = rsin\phi$:

$$f(x_1, x_2)\, dx_1\, dx_2 = f(r, \phi)\, r\, dr\, d\phi = \frac{1}{2\pi} e^{-r^2/2}\ r\, dr\, d\phi \tag{A2. 3}$$

Both variables $r$ and $\phi$ are independent and their cumulative distribution functions are:

$$F(r) = F(R \le r) = \int_0^r e^{-r^2/2}\ r\, dr = 1 - e^{-r^2/2} \tag{A2. 4}$$

$$G(\phi) = G(\Phi \le \phi) = \int_0^{2\pi} \frac{1}{2\pi} d\phi = 1 \tag{A2. 5}$$

Variable $\Phi$ is uniformly distributed in the interval [0,2π] so $\Phi = 2\pi \cdot \xi_1$. And variable $R$, according to its cumulative distribution function:

$$F(R) = 1 - e^{-\frac{R^2}{2}} = 1 - \xi_1 \Rightarrow R = \sqrt{-2\, ln\xi_1} \tag{A2. 6}$$

$$G(\Phi) = 1 = \xi_2 \Rightarrow \Phi = 2\pi\xi_2 \tag{A2. 7}$$

So the starting variables $x_1$ and $x_2$ can be expressed as:

$$\begin{aligned} x_1 &= \sqrt{-2\, ln\xi_1}\cos(2\pi\xi_2) \\ x_2 &= \sqrt{-2\, ln\xi_1}\sin(2\pi\xi_2) \end{aligned} \tag{A2. 8}$$

where $\xi_1$ and $\xi_2$ are two random independent random numbers, which can take values from 0 to 1.

Since a normal variable is described by a mean value ($\mu$) and a standard deviation ($\sigma$). To define a new random variable ($X$) the linear transformation described by Equation (A2. 9) can be applied, where $x$ is a random number generated with Box-Müller method; that is, which follows a Gaussian distribution.

$$X = m + \sigma x \tag{A2. 9}$$

As an example several random numbers were generated with Box-Müller method and applied, according to Equation (A2. 9), to a particular value $N$ = 10, which means to be a number of counts. The average value obtained from calculated random numbers was 10.002 and the standard deviation was 3.172.

Results are shown in Fig. A2. 1, where data obtained have been grouped in bins in order to plot their frequency (black points). A

Gaussian fit was added to the plot (red line) and the obtained values for the mean and the standard deviation are the ones expected.

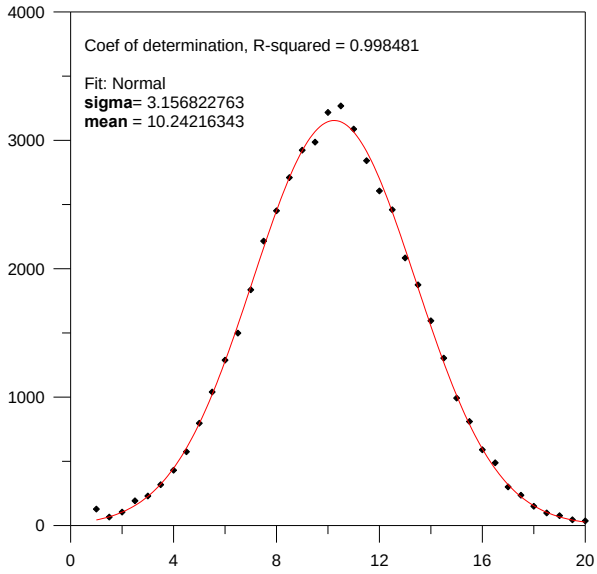


**Fig. A2. 1.** Data obtained from random points applying the Box-Müller transformation.

# Appendix 3. $H^*(10)$ and $^{222}Rn$

## A3.1 Long-time measurements of ambient dose equivalent rate values

Down below are calculated values of $\dot{H}^*(10)$ (red line) from gamma spectra measured with the 1" x 1" $LaBr_3(Ce)$ installed on the roof at INTE-UPC. The applied is the stripping method and an energy range 40 – 3000 keV have been considered. In all plots calculated values are compared with measured $\dot{H}^*(10)$ values (green line) with a RS04/WEB_R probe. Meteorological parameters (rain, temperature and atmospheric pressure) are also shown.

Plots are monthly and cover 1-year of measurements.

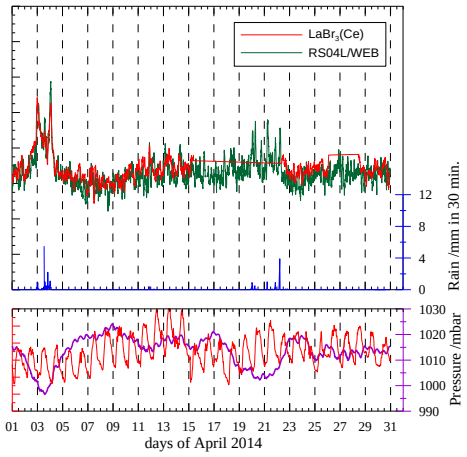

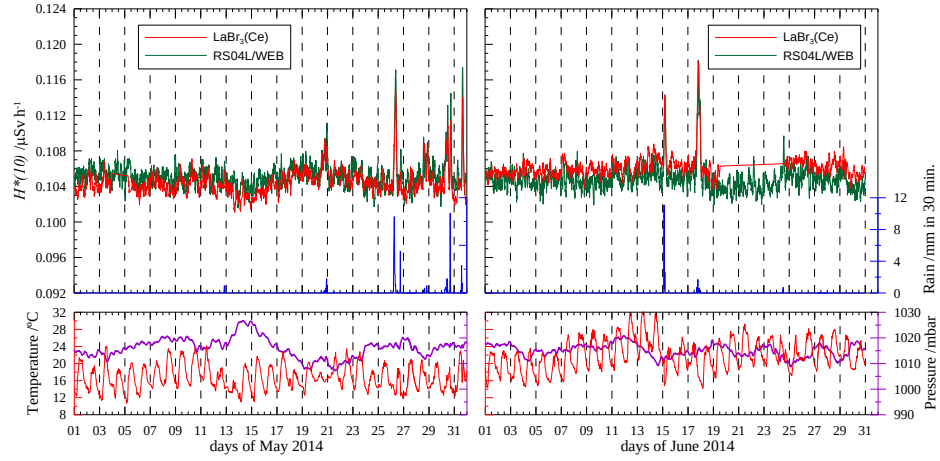
LaBr3(Ce)
RS04L/WEB
H*(10) /µSv h-1
Rain /mm in 30 min.
Temperature /°C
Pressure /mbar
days of May 2014
days of June 2014

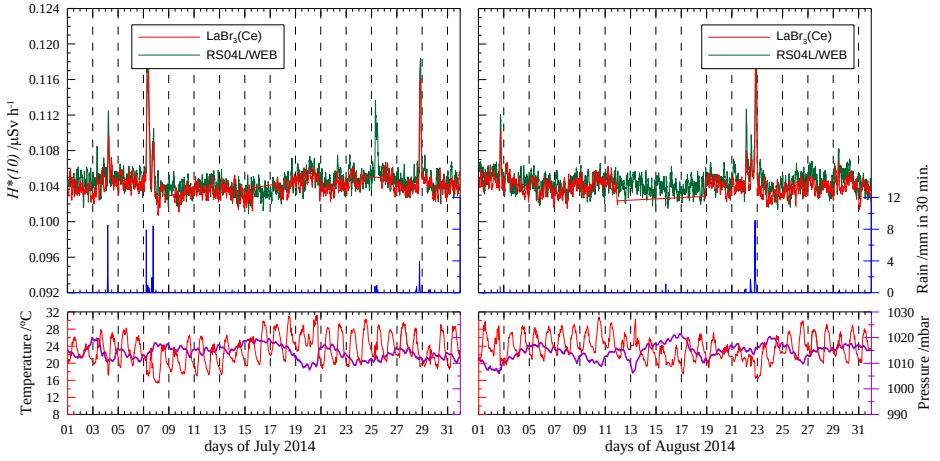
LaBr3(Ce)
RS04L/WEB
H*(10) /µSv h-1
Rain /mm in 30 min.
Temperature /°C
Pressure /mbar
days of July 2014
days of August 2014

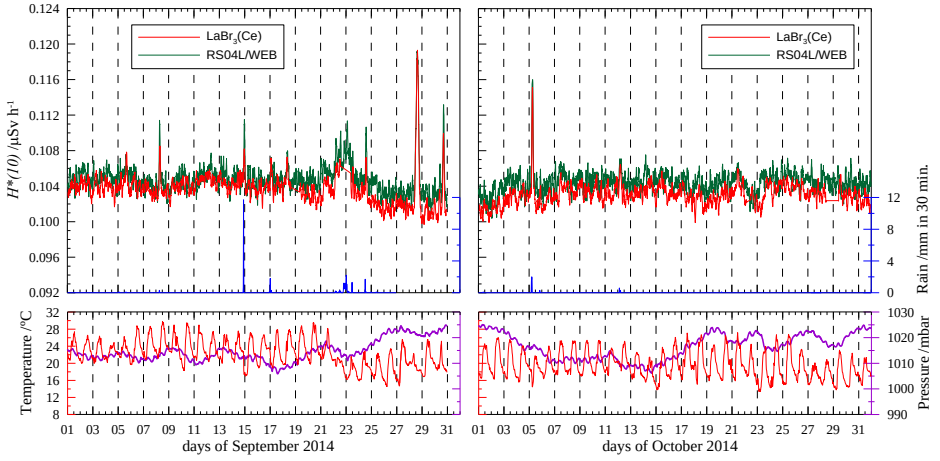
LaBr3(Ce)
RS04L/WEB
H*(10) /µSv h-1
Rain /mm in 30 min.
Temperature /°C
Pressure /mbar
days of September 2014
days of October 2014

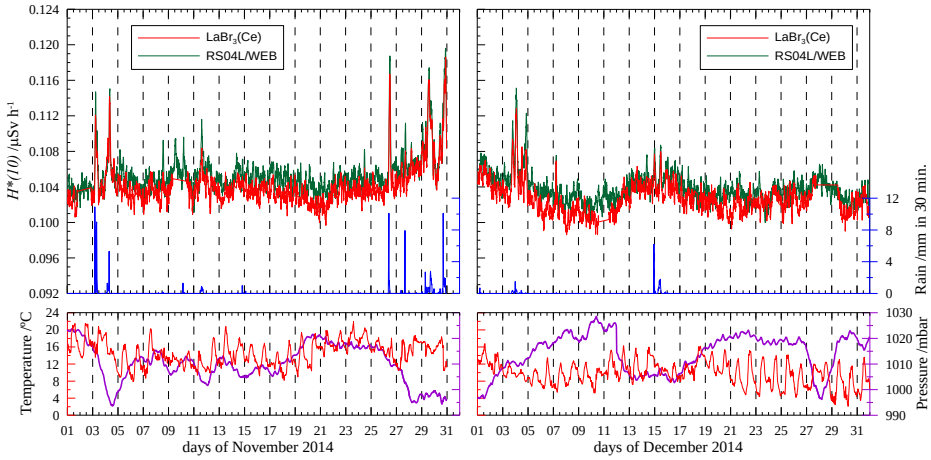
LaBr3(Ce)
RS04L/WEB
H*(10) /µSv h-1
Rain /mm in 30 min.
Temperature /°C
Pressure /mbar
days of November 2014
days of December 2014

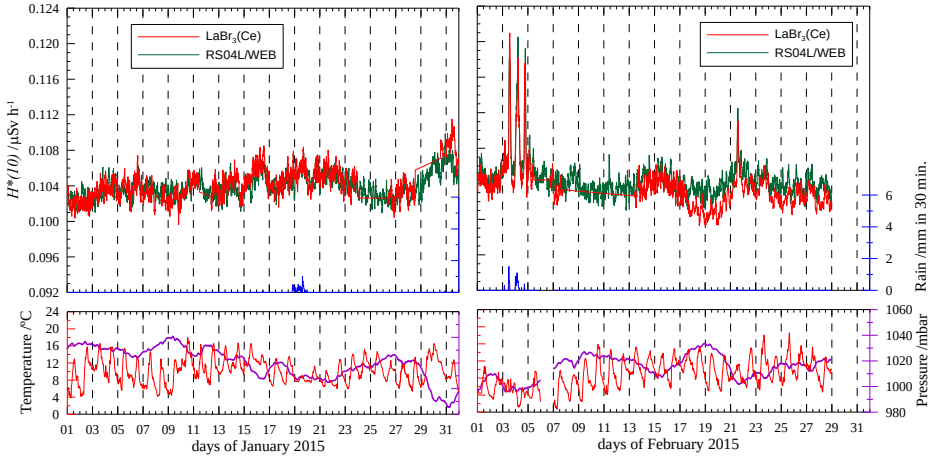
LaBr3(Ce)
RS04L/WEB
H*(10) /µSv h-1
Rain /mm in 30 min.
Temperature /°C
Pressure /mbar
days of January 2015
days of February 2015

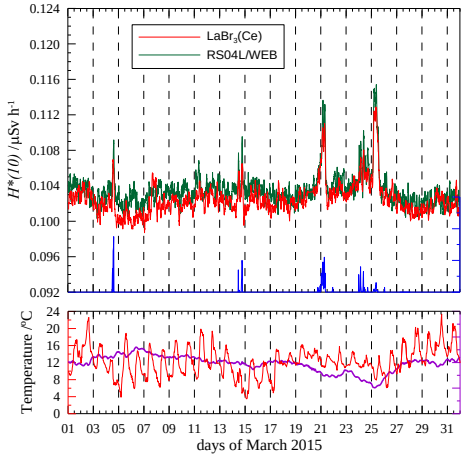
LaBr3(Ce)
RS04L/WEB
H*(10) /µSv h-1
Temperature /°C
days of March 2015

## A3.2 Measurements of $^{222}Rn$ and progeny at ESMERALDA-CIEMAT

Down below are plots corresponding to calculated $\dot{H}^*(10)$ using stripping and conversion factors, together with the $\dot{H}^*(10)$ obtained from RS monitor for all 2016. Calculated values of $\dot{H}^*(10)$ have been obtained from gamma spectra measured with 1.5" x 1.5" $LaBr_3(Ce)$, a commercial model named SpectroTRACER. Measuring site is the ESMERALDA station of CIEMAT, in Madrid.

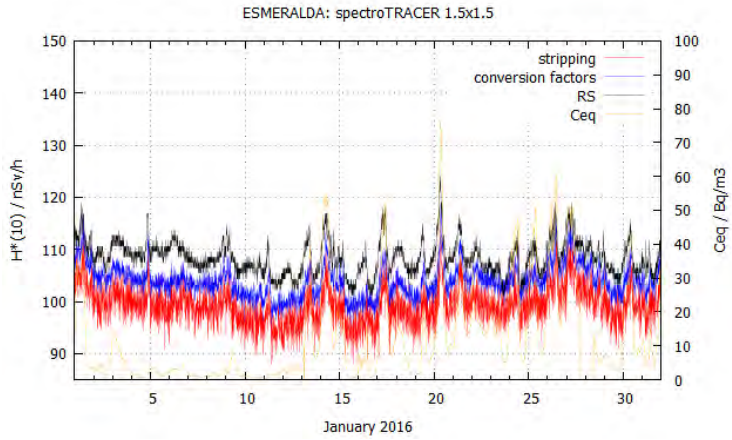


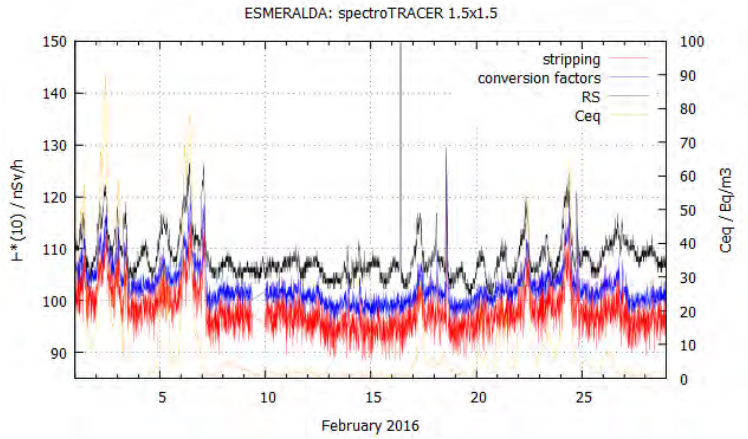

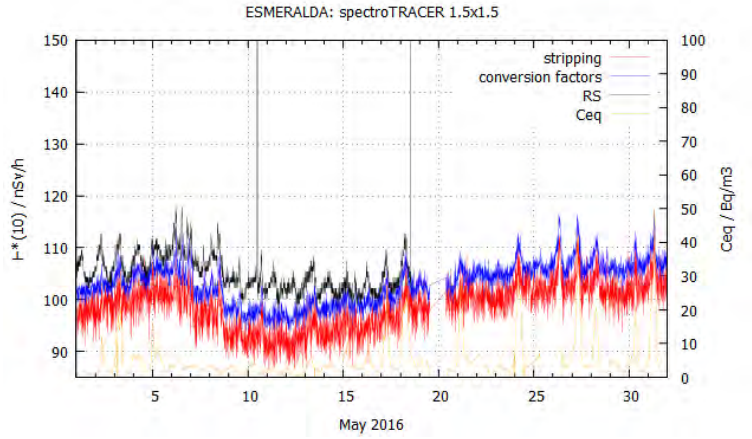
ESMERALDA: spectroTRACER 1.5x1.5
stripping
conversion factors
RS
Ceq
H*(10) / nSv/h
Ceq / Bq/m3
May 2016

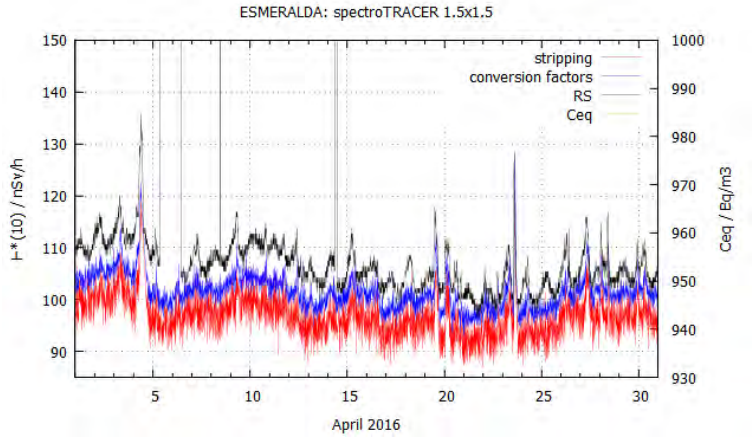
ESMERALDA: spectroTRACER 1.5x1.5
stripping
conversion factors
RS
Ceq
H*(10) / nSv/h
Ceq / Bq/m3
April 2016

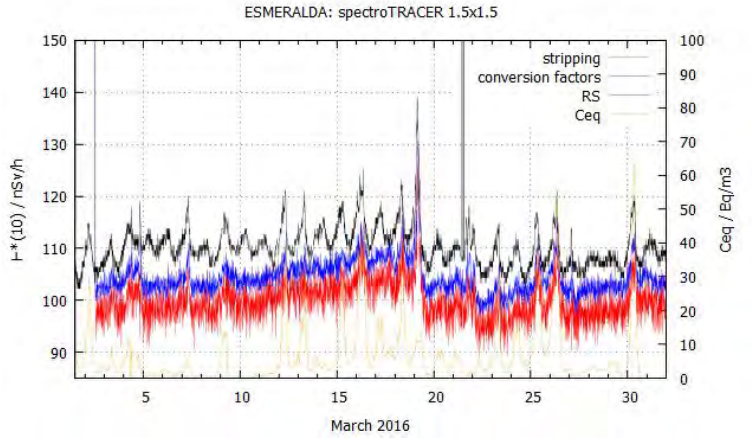
ESMERALDA: spectroTRACER 1.5x1.5
stripping
conversion factors
RS
Ceq
H*(10) / nSv/h
Ceq / Bq/m3
March 2016

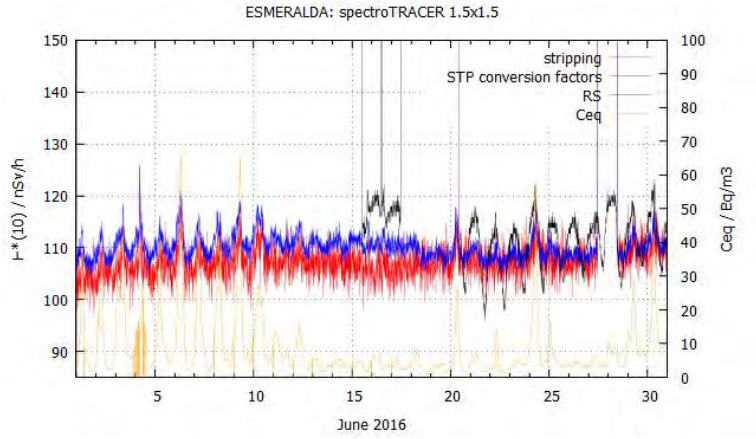
ESMERALDA: spectroTRACER 1.5x1.5
stripping
STP conversion factors
RS
Ceq
H*(10) / nSv/h
Ceq / Bq/m3
June 2016

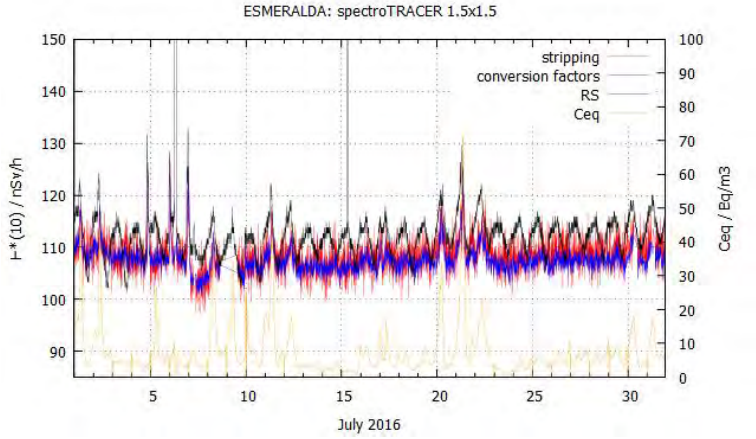
ESMERALDA: spectroTRACER 1.5x1.5
stripping
conversion factors
RS
Ceq
H*(10) / nSv/h
Ceq / Bq/m3
July 2016

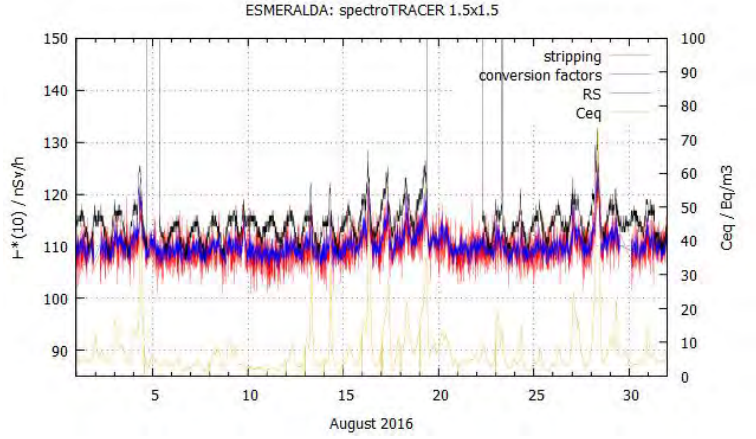
ESMERALDA: spectroTRACER 1.5x1.5
stripping
conversion factors
RS
Ceq
H*(10) / nSv/h
Ceq / Bq/m3
August 2016

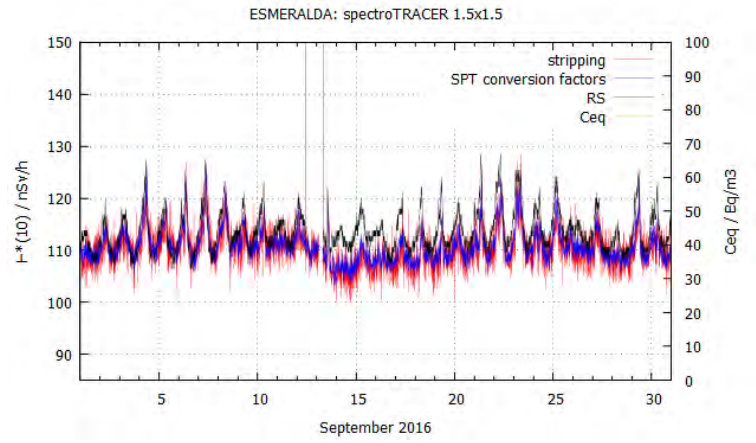
ESMERALDA: spectroTRACER 1.5x1.5
stripping
SPT conversion factors
RS
Ceq
H*(10) / nSv/h
Ceq / Bq/m3
September 2016

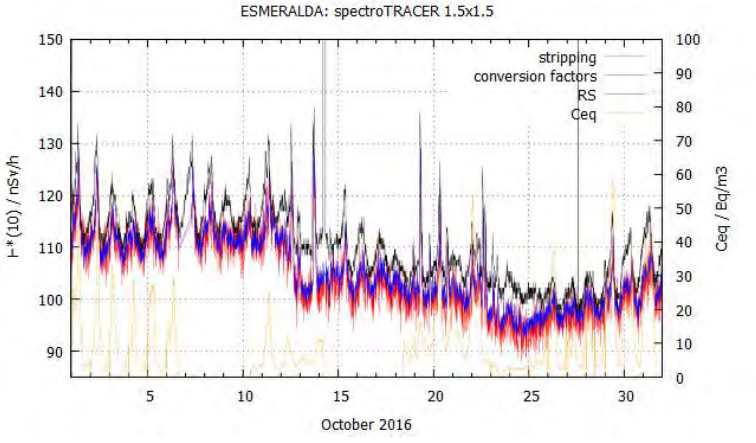
ESMERALDA: spectroTRACER 1.5x1.5
stripping
conversion factors
RS
Ceq
H*(10) / nSv/h
Ceq / Bq/m3
October 2016

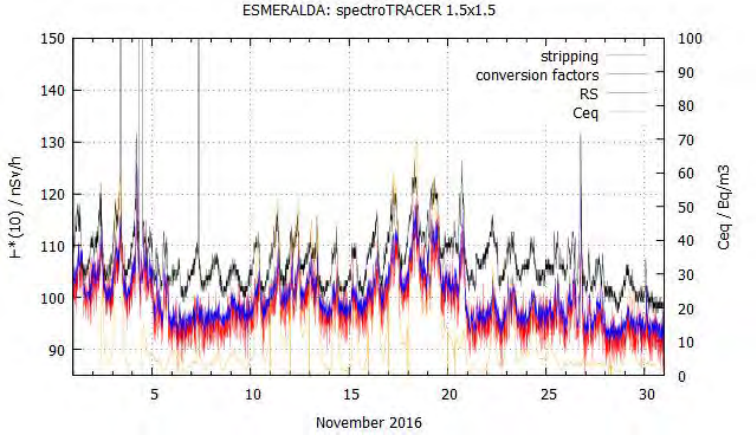
ESMERALDA: spectroTRACER 1.5x1.5
stripping
conversion factors
RS
Ceq
H*(10) / nSv/h
Ceq / Bq/m3
November 2016

o

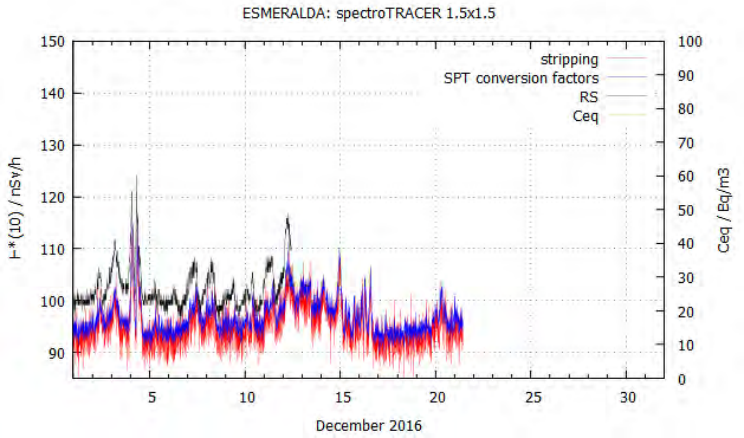
ESMERALDA: spectroTRACER 1.5x1.5
stripping
SPT conversion factors
RS
Ceq
H*(10) / nSv/h
Ceq / Bq/m3
December 2016
150
140
130
120
110
100
90
100
90
80
70
60
50
40
30
20
10
0
5
10
15
20
25
30

# Bibliography


Bé, M.-M., 2013. Table de Radionucléides. Available at ⟨http://www.nucleide.org/DDEP_WG/Nuclides/La-138_tables.pdf⟩

Barros, N., Borrego, C., Toll, I., Soriano, C., al, et, 2003. Urban photochemical pollution in the Iberian Peninsula: Lisbon and Barcelona airsheds. J. Air Waste Manage. Assoc. 53, 347–359.

Blaauboer, R.O., Smetsers, R.C.G.M., 1996. Variations in outdoors radiation levels in the Netherlands. Rijksuniversiteit Groningen.

Caballero Folch, R., 2008. Millora del monitor d'aerosols radioactius de l'estació radiometeorològica del Campus Nord. Universitat Politècnica de Catalunya.

Camp, A., Vargas, A., 2014. Ambient dose estimation H*(10) from LaBr3(Ce) spectra. Radiat. Prot. Dosimetry 160, 264–8. doi:10.1093/rpd/nct342

Camp, A., Vargas, A., Fernández-Varea, J.M., 2016. Determination of LaBr3(Ce) internal background using a HPGe detector and Monte Carlo simulations. Appl. Radiat. Isot. 109, 512–517. doi:10.1016/j.apradiso.2015.11.093

Casanovas, R., Morant, J.J., Salvadó, M., 2012. Temperature peak-shift correction methods for NaI(Tl) and LaBr3(Ce) gamma-ray spectrum stabilisation. Radiat. Meas. 47, 588–595. doi:10.1016/j.radmeas.2012.06.001

Clouvas, A., Xanthos, S., Antonopoulos-Domis, M., Silva, J., 1998. Monte Carlo based method for conversion of in-situ gamma ray spectra obtained with a portable Ge detector to an incident photon flux energy distribution. Health Phys. 74, 216–230. doi:10.1097/00004032-199802000-00007

Cortès, G., 2001. Aportaciones al estudio de los campos de radiación ionizantes ambientales. Universitat Politècnica de Catalunya.

Cortes, G., Sempau, J., Ortega, X., 2001. Automated measurement of radon daughters Bi-214 and Pb-214 in rain water. Nukleonika 46, 161–164

Dambacher, M., 2011. GMCA. Gamma Ray Analysis Digital Signal Processing Multi Channel Analyzer. User manual v0.9. Freiburg.

Dambacher, M., Zwerger, A., Fauler, A., Disch, C., Stöhlker, U., Fiederle, M., 2011. Development of the gamma-ray analysis digital filter multi-channel analyzer (GMCA). Nucl. Instruments Methods Phys. Res. Sect. A Accel. Spectrometers, Detect. Assoc. Equip. 652, 445–449. doi:10.1016/j.nima.2011.02.020

Decay chain, n.d. In *Wikipedia.* Retrieved January 10, 2017, from https://en.wikipedia.org/wiki/Decay_chain

Deslattes, R.D., Kassler, E.G., Indelicato, P., De Billy, L., Lindroth, E., Anton, J., 2003. X-ray transition energies: New approach to a comprehensive evaluation. Rev. Mod. Phys. 75, 35–99. doi:10.1103/RevModPhys.75.35

Dombrowski, H., 2014. Area dose rate values derived from NaI or LaBr3 spectra. Radiat. Prot. Dosimetry 160, 269–76. doi:10.1093/rpd/nct349

Dorenbos, P., de Haas, J.T.M., van Eijk, C.W.E., 2004. Gamma ray spectroscopy with a Ø19x19 mm3 LaBr3 : 0.5% Ce3+ scintillator. IEEE Trans. Nucl. Sci. 51, 1289–1296. doi:10.1109/TNS.2004.829375

Elanique, A., Marzocchi, O., Leone, D., Hegenbart, L., Breustedt, B., Oufni, L., 2012. Dead layer thickness characterization of an HPGe detector by measurements and Monte Carlo simulations. Appl. Radiat. Isot. 70, 538–542. doi:10.1016/j.apradiso.2011.11.014

Firestone, R.B., Ekström, L., 2004. WWW Table of Radioactive Isotopes, Version 2.1. URL http://ie.lbl.gov/toi/

Galmarini, S., 2006. One year of 222Rn concentration in the atmospheric surface layer. Atmos. Chem. Phys. 6, 2865–2886. doi:10.5194/acp-6-2865-2006

Garcia-Toraño, E., Malonda, A.G., 1985. EFFY, a new program to compute the couting efficiency of beta particles in liquid scintillators. Comput. Phys. Commun. 36, 307–312. doi:10.1016/0010-4655(85)90057-8

Gilmore, G.R., 2008. Practical Gamma-ray Spectrometry, 2nd ed. John Wiley & Sons Ltd, Chichester, West Sussex, England.

Grasty, R.L., Walters, B.R.B., Hovgaard, J., LaMarre, J.R., 2001. Calibration of a 7.6 cm x 7.6 cm (3 inch x 3 inch) Sodium Iodide Gamma Ray Spectrometer for Air Kerma Rate. Radiat. Prot. Dosim. 94 , 309–316.

Grossi, C., Arnold, D., Adame, J.A., López-Coto, I., Bolívar, J.P., de la Morena, B.A., Vargas, A., 2012. Atmospheric 222Rn concentration and source term at El Arenosillo 100 m meteorological tower in southwest Spain. Radiat. Meas. 47, 149–162. doi:10.1016/j.radmeas.2011.11.006

Hirayama, H., Namito, Y., Bielajew, A.F., Wilderman, S.J., Nelson, W.R., 2005. The EGS5 Code System, KEK Report 2005-8, SLAC-R-730.

Hubbell, J., Seltzer, S.M., 1995. Tables of X-Ray Mass Attenuation Coefficients and Mass Energy-Absorption Coefficients 1 keV to 20 MeV for Elements Z = 1 to 92 and 48 Additional Substances of Dosimetric Interest.

Huy, N.Q., 2011. Dead-layer thickness effect for gamma spectra measured in an HPGe p-type detector. Nucl. Instruments Methods Phys. Res. Sect. A Accel. Spectrometers, Detect. Assoc. Equip. 641, 101–104. doi:10.1016/j.nima.2011.02.097

IAEA, 2007. IAEA safety glossary : terminology used in nuclear safety and radiation protection : 2007 edition.

ISO 4037-3, 1999. International Organization for Standardization. X and gamma reference radiation for calibrating dosemeters and doserate meters and for determining their response as function of photon energy—Part 3: Calibration of area and personal dosemeters and the meas.

JCGM/WG1, 2008. JCGM 100:2008. Evaluation of measurement data - Guide to the expression of uncertainty in measurement.

Kendall, G.M., Smith, T.J., 2002. Doses to organs and tissues from radon and its decay products. J. Radiol. Prot. 22, 389–406. doi:10.1088/0952-4746/22/4/304

Knoll, G.F., 2010. Radiation Detection and Measurement, 4th ed. John Wiley&Sons, New York.

Kurvinen, K., Smolander, P., Pöllänen, R., Kuukankorpi, S., Kettunen, M., Lyytinen, J., 2005. Design of a radiation surveillance unit for an unmanned aerial vehicle. J. Environ. Radioact. 81, 1–10. doi:10.1016/j.jenvrad.2004.10.009

MacFarlane, J.W., Payton, O.D., Keatley, A.C., Scott, G.P.T., Pullin, H., Crane, R.A., Smilion, M., Popescu, I., Curlea, V., Scott, T.B., 2014. Lightweight aerial vehicles for monitoring, assessment and mapping of radiation anomalies. J. Environ. Radioact. 136, 127–30. doi:10.1016/j.jenvrad.2014.05.008

McGinnis, R., 2009. Rad Pro Calculator. Version 3.26.

Menge, P.R., Gautier, G., Iltis, A., Rozsa, C., Solovyev, V., 2007. Performance of large lanthanum bromide scintillators. Nucl. Instruments Methods Phys. Res. Sect. A Accel. Spectrometers, Detect. Assoc. Equip. 579, 6–10. doi:10.1016/j.nima.2007.04.002

Milbrath, B.D., Runkle, R.C., Hossbach, T.W., Kaye, W.R., Lepel, E.A., McDonald, B.S., Smith, L.E., 2005. Characterization of alpha contamination in lanthanum trichloride scintillators using coincidence measurements. Nucl. Instruments Methods Phys. Res. Sect. A Accel. Spectrometers, Detect. Assoc. Equip. 547, 504–510. doi:10.1016/j.nima.2004.11.054

Miller, K.M., 1984. A Spectral Stripping Method for a Ge Spectometer used for Indoor Gamma Exposure Rate Measurements. New York.

Minato, S., 1980. Some observations of the variations in natural gamma radiation due to rainfall. United States.

Moszyński, M., Nassalski, A., Syntfeld-Każuch, A., Szczęśniak, T., Czarnacki, W., Wolski, D., Pausch, G., Stein, J., 2006. Temperature dependences of LaBr3(Ce), LaCl3(Ce) and NaI(Tl) scintillators. Nucl. Instruments Methods Phys. Res. Sect. A Accel. Spectrometers, Detect. Assoc. Equip. 568, 739–751. doi:10.1016/j.nima.2006.06.039

Mougeot, X., 2015. Reliability of usual assumptions in the calculation of β and ν spectra. Phys. Rev. C 91, 055504. doi:10.1103/PhysRevC.91.055504

Namito, Y., Nakamura, H., Toyoda, A., Iijima, K., Iwase, H., Ban, S., Hirayama, H., 2012. Transformation of a system consisting of plane isotropic source and unit sphere detector into a system consisting of point isotropic source and plane detector in Monte Carlo radiation transport calculation. J. Nucl. Sci. Technol. 49, 167–172. doi:10.1080/00223131.2011.649079

Neumaier, S., Dombrowski, H., 2014. Eurados intercomparisons and the harmonisation of environmental radiation monitoring. Radiat. Prot. Dosimetry 160, 297–305. doi:10.1093/rpd/ncu002

Photonis, 2007. Photomultiplier XP2060.

Pöllänen, R., Toivonen, H., Peräjärvi, K., Karhunen, T., Ilander, T., Lehtinen, J., Rintala, K., Katajainen, T., Niemelä, J., Juusela, M., 2009. Radiation surveillance using an unmanned aerial vehicle. Appl. Radiat. Isot. 67, 340–344. doi:10.1016/j.apradiso.2008.10.008

Porstendörfer, J., 1994. Properties and behaviour of radon and thoron and their decay products in the air. J. Aerosol Sci. 25, 219–263. doi:10.1016/0021-8502(94)90077-9

Quarati, F., Bos, A.J.J., Brandenburg, S., Dathy, C., Dorenbos, P., Kraft, S., Ostendorf, R.W., Ouspenski, V., Owens, A., 2007. X-ray and gamma-ray response of a 2″×2″ LaBr3:Ce scintillation detector. Nucl. Instruments Methods Phys. Res. Sect. A Accel. Spectrometers, Detect. Assoc. Equip. 574, 115–120. doi:10.1016/j.nima.2007.01.161

Quarati, F.G.A., Dorenbos, P., van der Biezen, J., Owens, A., Selle, M., Parthier, L., Schotanus, P., 2013. Scintillation and detection characteristics of high-sensitivity CeBr3 gamma-ray spectrometers. Nucl. Instruments Methods Phys. Res. Sect. A Accel. Spectrometers, Detect. Assoc. Equip. 729, 596–604. doi:10.1016/j.nima.2013.08.005

Quarati, F.G.A., Khodyuk, I. V., Van Eijk, C.W.E., Quarati, P., Dorenbos, P., 2012. Study of 138La radioactive decays using LaBr 3 scintillators. Nucl. Instruments Methods Phys. Res. Sect. A Accel. Spectrometers, Detect. Assoc. Equip. 683, 46–52. doi:10.1016/j.nima.2012.04.066

Salvat, F., Fernández-Varea, J.M., Sempau, J., 2011. PENELOPE-2011 : A Code System for Monte Carlo Simulation of Electron and Photon Transport (No. NEA/NSC/DOC(2011)5), Nuclear Energy Agency. Workshop Proceedings. Barcelona.

Sáez-Vergara, J.C., Romero, A.M., Correa, E., 1996. Establecimiento en el CIEMAT de una estación de referencia secundaria para la medida de dosis ambientales externas, in: Proceedings VI Congreso de La Sociedad Española de Protección Radiológica, Radioprotección (special Issue). pp. 153–154.

Sáez-Vergara, J.C., Thompson, I.M.G., Gurriarán, R., Dombrowski, H., Funck, E., Neumaier, S., 2007. The second eurados intercomparison of national network systems used to provide early warning of a nuclear accident. Radiat. Prot. Dosimetry 123, 190–208. doi:10.1093/rpd/ncl112

Sáez-Vergara, J.C., Vila Pena, M., Sancho Llerandi, C., 2004. CIEMAT/CSN Co-operation on the quality assurance of the Spanish automatic early-warning network "REA," in: 11th International Congress of the International Radiation Protection Association.

Saint Gobain, 2009. BrilLance Scintillators. Scintillation Products Technical Note.

Saint Gobain Crystals, 2004. Efficiency Calculations for Selected Scintillators.

Saint-Gobain Crystals, 2009. BrilLance Scintillators. Performance Summary.

Salvat, F., Fernández-Varea, J.M., Sempau, J., 2011. PENELOPE-2011 : A Code System for Monte Carlo Simulation of Electron and Photon Transport (No. NEA/NSC/DOC(2011)5), Nuclear Energy Agency. Workshop Proceedings. Barcelona.

Sanada, Y., Torii, T., 2015. Aerial radiation monitoring around the Fukushima Dai-ichi Nuclear Power Plant using an unmanned helicopter. J. Environ. Radioact. 139, 294–9. doi:10.1016/j.jenvrad.2014.06.027

Scintillation counter, n.d. In *Wikipedia.* Retrieved November 25, 2016, from https://en.wikipedia.org/wiki/Scintillation_counter#/media/File:PhotoMultiplierTubeAndScintillator.jpg

Sempau, J., Badal, A., Brualla, L., 2011. A PENELOPE-based system for the automated Monte Carlo simulation of clinacs and voxelized geometries--application to far-from-axis fields. Med. Phys. 38, 5887–5895.

Sonzogni, A.A., 2003. Nuclear Data Sheets for A = 138. Nucl. Data Sheets 98, 515–664. doi:10.1006/ndsh.2003.0004

Toivonen, H., Vesterbacka, K., Pelikan, A., Mattila, A., Karhunen, T., 2008. LaBr3 Spectrometry for Environmental Monitoring, in: The 12th International Congress of the International Radiation Protection Association. Buenos Aires, Argentina, p. 15.

Towler, J., Krawiec, B., Kochersberger, K., 2012. Terrain and Radiation Mapping in Post-Disaster Environments Using an Autonomous Helicopter. Remote Sens. 4, 1995–2015. doi:10.3390/rs4071995

UNSCEAR, 2008. Sources and Effects of Ionizing Radiation.

Vargas, A., Arnold, D., Adame, J.A., Grossi, C., Hernández-Ceballos, M.A., Bolivar, J.P., 2015. Analysis of the vertical radon structure at the Spanish "El Arenosillo" tower station. J. Environ. Radioact. 139, 1–17. doi:10.1016/j.jenvrad.2014.09.018

Vargas, A., Camp, A., Serrano, I., Duch, M.A., 2014. Coincidence summing corrections for volume samples using the PENELOPE/penEasy Monte Carlo code. Appl. Radiat. Isot. 87, 376–9. doi:10.1016/j.apradiso.2013.11.057

Vargas, A., Cornejo, N., Camp, A., 2017. Comparison of methods for H*(10) calculation from LaBr3(Ce) measured spectra. Appl. Radiat. Isot. Submitted.

Vargas, A., Ortega, X., Cortes, G., Bonet, J., 2004. Response of a radioactive aerosol monitor to radon progeny concentration, in: 11th International Congress of the International Radiation Protection Association, 11th International Congress of the International Radiation Protection Association. p. 246.

Williams, T., Kelley, C., n.d. Gnuplot: an interactive plotting program.

XIA LLC, 2009. microDXP Digital X-Ray Processor. Technical Reference Manual v1.1.2. Hayward.

Yi, C.Y., Jun, J.S., Chai, H.S., Oh, J.J., Yun, J.Y., 1997. Measurement of Ambient Dose Equivalent Using a NaI(Tl) Scintillation Detector. Radiat. Prot. Dosim. 74 , 273–278.

Zähringer, M., Sempau, J., 1997. Calibration factors for dose rate probes in environmental monitoring networks obtained from monte carlo simulations. BfS-IAR.